Theory of quantum transport in molecular-scale structures

Turki Bashar A Alotaibi

B.Sc., M.Sc.

PhD Thesis in Physics

Department of physics, Lancaster University, UK

This Thesis is submitted in partial fulfilment of the requirements for degree of Doctor of Philosophy

2022

Declaration

I hereby declare that the thesis is my own work and effort and has not been submitted in substantially the same form for the award of a higher degree elsewhere. Other sources of information have been used, they have been acknowledged. This thesis documents work carried out between July 2019 and February 2022 at Lancaster University UK, under the supervision of Prof. Colin J. Lambert and funded by Jouf University, KSA.

Turki Alotaibi

Feb. 2022

Acknowledgment

I would like to express deepest gratitude to Prof. Colin John Lambert for the excellent supervision and guidance I received. This thesis would never completed without his enormous support and excellent guidance. I would also like to express my grateful admiration to Dr Ali Ismael, none of this work would have been accomplished without his insightful comments and suggestions, dedicated time, and guidance. Also, many thanks to Theory of molecular-Scale groups especially Dr Michel Jay and Dr Majed Alshammari.

I would like also to thank my sponsor Jouf University KSA, for given me this great opportunity to study a Ph.D. in the United Kingdom.

I would like to thank the collaborating experimental groups. I would like to thank all my friends and colleagues in Colin's group.

Last but not the least, I would like to thank dear family for showing their constant care, love and support. I also express my deepest gratitude to my supportive wife and my daughters for giving me courage and hope throughout my study.

Above all, my great thanks to ALLAH for his mercy and blessing.

Abstract

Molecular electronics is a flexible approach to studying nanoscale thermoelectricity and helping the discovery of new low-cost and environmentally friendly organic thermoelectric materials. This thesis introduces the theoretical tools used to support this process, starting in chapters 2 and 3, respectively. I have addressed the fundamental equations and techniques that support my work, such as the Schrodinger equation, density functional theory (DFT), and the SIESTA programme, which implements DFT and solves the underlying equations. I also explain single particle transport theory, which is based on the Hamiltonian and Green's functions, and provide some illustrations of how it may be employed.

Chapter 4 is the first results chapter in this thesis, in which the three endohedral metallofullerenes (EMFs) $Sc_3N@C_{80}$, $Sc_3C_2@C_{80}$ and $Er_3N@C_{80}$ are studied and compared with C_{60}. I commenced my investigation by displaying the wave function plots of the molecules under investigation. I examined the charge transfer between metallic moieties and the cage employing three different methods: Mulliken population, Hirshfeld, and Voronoi. The charge transfer analyses were performed on a gold substrate and in the gas phase. The counterpoise approach was utilised to determine the most energy-favourable orientation for metallic moieties like $Sc_3N@C_{80}$, $Sc_3C_2@C_{80}$ and $Er_3N@C_{80}$ to settle within the I_h-cage.

I have shown how rotation angles θ, Φ, α and β about different axes play an important role in the conductance and Seebeck coefficient fluctuations. I investigated how the total energy varies with the angle of rotation, both in presence and absence of the gold substrate. There are an infinite number of inequivalent orientations of the metallic moieties comparative to their fullerene cage. Therefore, for each of the four axes, I considerd one mode of rotation in the gas phase and three modes of rotation on a substrate. I used DFT to determine the optimum distances between EMFs and the metallic electrodes.

In chapter 5, I address the parameters that I investigated in Chapter 4 to enhance my simulations. Then I demonstrated how standard deviations in the Seebeck coefficient σ_S of EMF-based junctions are associated to the geometric standard deviation σ and charge inhomogeneity σ_q, exhibiting a fascinating structure-function relation. I compared EMF molecules to C_{60} and identified that σ_q, σ_S are the highest

for $Sc_3C_2@C_{80}$, and the lowest for C_{60}, whereas the other EMFs follow the order $Sc_3C_2@C_{80}$ >$Sc_3N@C_{80}$ > $Er_3N@C_{80}$ > C_{60}.

A significant value of σ_S indicates that a molecule could exhibit a wide range of Seebeck coefficients, and if the orientations corresponding to the large range can be isolated and controlled, the molecule has the potential to exhibit high-performance thermoelectricity. Large values of σ_S are associated with a broad Seebeck coefficient distribution, with both positive and negative signs. Ffor the EMFs explored here, this shows that they are bi-thermoelectric materials. Furthermore, molecules with high charge inhomogeneity reveal rare examples of high thermopower, suggesting that such molecules have the potential to produce high-performance thermoelectricity if these rare junction configurations can be isolated and controlled.

List of Figures

rotation about θ (obtained from the difference between the maxima and minima of $\Delta(\theta)$) are 400, 300 and 130 meV respectively, and the moieties Sc_3C_2 moieties Sc_3C_2 has preferred orientations of $\theta \approx 0°$, 190° and 360°, corresponding to the minima of $\Delta(\theta)$. The energy barriers $\Delta E(\Phi)$ to rotation about Φ are 350, 250 and 100 meV respectively, and therefore the moiety Sc_3C_2has preferred orientations of $\Phi \approx$ (0°, 110°, 180°, 210°, 270° and 360°). The energy barriers to rotation about α are 300, 150 and 60 meV respectively, and therefore the moieties Sc_3C_2 has preferred orientations of $\alpha \approx$ (0°, 75°, 160°, 240° and 320°). 70

Figure 4.14. Top panel: The energy difference $\Delta(\theta)$ as a function of rotation angle θ of Sc_3N within the fixed I_h-C_{80} cage. Bottom panel: The energy differecne $\Delta(\Phi, \alpha)$ as a function of rotation angles Φ and α (yellow and green respectively), of Sc_3N within the fixed I_h-C_{80} cage. The energy barriers $\Delta E(\theta)$ to rotation about θ (obtained from the difference between the maxima and minima of $\Delta(\theta)$) are 400, 300 and 130 meV respectively, and the moieties Sc_3N moieties Sc_3N has preferred orientations of $\theta \approx 0°$, 190° and 360°, corresponding to the minima of $\Delta(\theta)$. The energy barriers $\Delta E(\Phi)$ to rotation about Φ are 350, 250 and 100 meV respectively, and therefore the moiety Sc_3Nhas preferred orientations of $\Phi \approx$ (10°, 95°, 200°, 280° and 340°). The energy barriers to rotation about α are 300, 150 and 60 meV respectively, and therefore the moieties Sc_3N has preferred orientations of $\alpha \approx$ (0°, 75°, 100°, 150°, 200° 250°, 300° and 350°). 71

Figure 4.15. Top panels: The energy difference $\Delta(\theta)$ as a function of rotation angle θ of Er_3N within the fixed I_h-C_{80} cage. Bottom panels: The energy differecne $\Delta(\Phi, \alpha)$ as a function of rotation angles Φ and α (yellow and green respectively), of Er_3N within the fixed I_h-C_{80} cage. The energy barriers $\Delta E(\theta)$ to rotation about θ (obtained from the difference between the maxima and minima of $\Delta(\theta)$) are 400, 300 and 130 meV respectively, and the moieties Er_3N moieties Er_3N has preferred orientations of $\theta \approx 0°$, 190° and 360°, corresponding to the minima of $\Delta(\theta)$. The energy barriers $\Delta E(\Phi)$ to rotation about Φ are 350, 250 and 100 meV respectively, and therefore the moiety Er_3N has preferred orientations of $\Phi \approx$ (0°, 120°, 250° and 350°). The energy barriers to rotation about α are

List of Tables

List of abbreviations

SIESTA	Spanish Initiative for Electronic Simulations with Thousands of Atoms
DFT	Density Functional Theory
DOS	Density of States
LDA	Local Density Approximation
GGA	Generalized Gradient Approximation
vdW	Van der Waals
CP	Counterpoise Correction
BSSE	Basis Set Superposition Error Correction
DZ	Double-ξ basis set
DZP	Double- ξ polarized basis set
LCAO	Linear Combination of Atomic Orbital
LCAOB	Linear Combination of Atomic Orbital Basis
STM- B	Scanning Tunnelling Microscopy Break Junctions
MCBJ	Mechanically Controllable Break Junctions
HOMO	Highest Occupied Molecular Orbital
LUMO	Lowest Unoccupied Molecular Orbital
EMFs	Endohedral metallofullerenes
T(E)	Transmission coefficient
S	Seebeck coefficient
G	electrical conductivity
P	Power factor
G_0	quantum of conductance
σ	standard deviation

List of Publications

1. Laura Rincón-García, Charalambos Evangeli, Panagiotis Dallas, **Turki Alotaibi**, Alaa A. Al-Jobory, Gabino Rubio-Bollinger, Kyriakos Porfyrakis, Nicolás Agraït and Colin J. Lamber. Exploiting fluctuations in the search for high-thermoelectric-performance molecular junctions. *Submitted.*

2. Wenqiang Cao, Alaa Al-Jobory, Qian-Chong Zhang, Jingyao Ye, Abdullah Alshehab, Kai Qu, **Turki Alotaibi**, Hang Chen, Junyang Liu, Zhong-Ning Chen, Colin J. Lambert and Wenjing Hong. Highly Insulative Alkane Rings with Destructive σ-Interference. *Submitted.*

Table of Contents

Chapter 1

Molecular electronics and thermopower

Molecular electronics is the study of molecules in order to build up electronic components or electronic devices [1]. Electrical components such as single-molecule [2] junctions, have the potential to deliver: memories [3], sensors [4], logic gates [5], and thermoelectric energy with ultralow energy needs and device areas less than 10 nm. These are also of interest due to their ability to probe room-temperature quantum properties at a molecular scale, including thermoelectricity and quantum interference [6].

In 1974, the first molecular rectifier was proposed by Aviram and Ratner [7]. Since then, the field of single molecule electronics has stimulated the interest of many scientists. A vast number of molecules have been investigated by modifying their chemical structure, some of which act as fundamental electronic elementary devices, including conducting wires [8] rectifiers [9] and negative differential resistance devices, [10]. The use of specialised intermolecular interactions to create molecular devices is a significant challenge in molecular electronics. As a consequence, a thorough understanding of electron transport between nearby molecules is required.

In this thesis, electrode molecule-electrode systems are examined primarily using theoretical methodologies. Experimental measurements of these systems have been made by experimental groups using two kinds of equipment: Scanning Tunneling Microscopy Break Junctions (STM-BJ) [11] and Mechanically Controllable Break Junctions (MCBJ) [12]. Lately, more scalable methods for connecting single molecules, such like graphene-based junctions and silicone-based junctions have been developed. However, structural issues in 2D hexagonal materials have been discussed for some years [13]and consequently their recruitment as electrodes is still in its initial stages. Therefore, for the time being, gold break junctions are the recommended contacting approach. Several strategies for regulating electron transport have been devised within such limits, including electrochemical gating [14] and mechanical gating [15].

Recently, there has been significant progress in understanding the thermoelectrical characteristics of single-molecule junctions [16], stimulated in part by observations of high Seebeck coefficient of order 161 μVK for PEDOT: PSS organic films [17]. It was recently found that the sign of endohedral metallofullerenes EMF and nanotubes may be altered by applying pressure, strain, and intermolecular interactions [18]. In endohedral fullerenes, the presence of transport resonances closer to the Fermi level, according to theoretical predictions, is a major factor to determine the thermoelectric performance of a molecular junction. The effect of transmission resonances was explored theoretically by Finch *et al* [19]. Fano resonance mostly around the Fermi level enhances thermopower and thermoelectric efficiency. Enhanced thermoelectric properties have also been predicted in the vicinity of interference-induced transmission nodes [20]. $Sc_3N@C_{80}$ EMF, is known to have a relatively small energy gap [21] and to be particularly stable at room temperature and even at elevated temperatures [22]. The presence of a metallic moiety within the fullerene cage not only will provide new resonances, but also allowed tuning of the position of the resonance and hence the sign of the thermopower by mechanically compressing the junction according on the orientation of the molecule.

Kroto, Curl, and Smalley [23] discovered fullerenes in 1985 and were awarded the 1996 Nobel Prize of Chemistry for their work. Fullerenes are closed-cage molecules composed entirely of carbon atoms. C_{60} was the first example synthesised and is the most stable and common fullerene. The discovery of smaller and higher fullerenes, (see e.g. Figure 1.1a, C_{78}) made up of 28 to hundreds of carbon atoms, extends the family of fullerenes. Other significant breakthroughs in carbon nanoscience have followed their discovery, including the discovery of carbon nanotubes and graphene. Fullerenes are made up of combined pentagons and hexagons., with C_{60} possessing 12 pentagons and 20 hexagons. However, regardless of the fact that it contains all-conjugated carbon atoms, C_{60} is not a particularly aromatic compound.

The closed-cage form of fullerene molecules is suitable for encapsulating a diverse range of atoms, molecules, and clusters. These compounds are known as endohedral fullerenes, an example of which is shown in Figure 1.1b. In 1991, $La@C_{82}$ was identified as the first endohedral fullerene [24]. From then on, a diverse variety of endohedral fullerenes have been synthesised, whose striking features, result

from the interaction between the encapsulated species and the cage [25,26]. Endohedral metallofullerenes (EMFs) are formed by encapsulating metal species, which interact with the surrounding cage and affect the electrical structure, leading to various of applications in materials science, photovoltaics, and medicine.

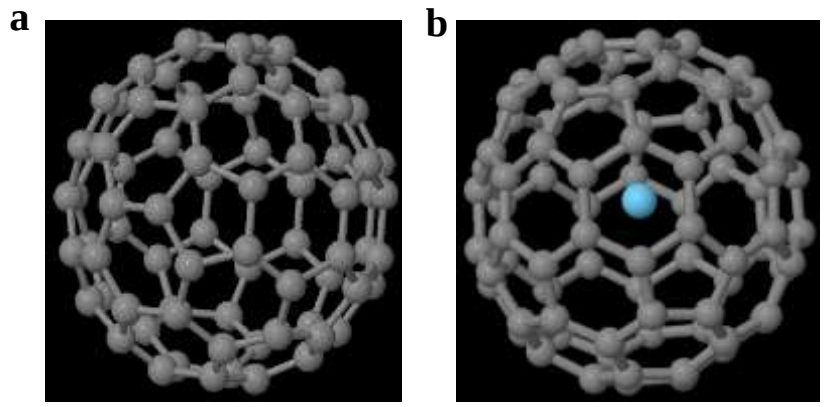

Figure 1.1. a: C_{78} an example for fullerene and **b:** La@C_{82} an example for endohedral fullerenes.

1.2 Thesis outline

As an introduction to the theoretical methods used to describe electron transport in molecular-scale junctions, chapter 2, provides an outline of density functional theory (DFT). The Hohenberg-Kohn theorems and the Kohn-Sham theorems are described and the Exchange Correlation Functionals and correlation energies in the local density approximation and the generalized gradient approximation are explained. Finally, the SIESTA code is introduced, along with some fine details of the calculations, such as the use of pseudopotentials and finite basis sets.

Chapter 3, discusses electron transport and the Landauer formula. It also, provides examples of the Green's functions for a Scattering Theory in simple one-dimensional discretized lattice and then moves on to calculating the scattering matrix of a ssytems connected to one-dimensional leads. In addition, it presents a generalized approach to transport calculations.

In Chapter 4, the electronic structure of three endohedral metallofullerenes (EMFs), including $Sc_3N@C_{80}$, $Sc_3C_2@C_{80}$, and $Er_3N@C_{80}$, in addition to an empty cage such as C_{60} were intensively

explored. I start by examining the wave functions of the studied molecules. Three different methods including Mulliken pobulation, Hirshfeld and Voronoi analyses, were employed to track down the charge transfer between metallic moieties and the cage. The charge transfer analyses were applied in the gas phase and on a gold substrate. The counterpoise method was used to determine the most probable orientation for metallic moieties inside the cage. The orientations of metallic moieties were also explored relative to 3 different rotation axes θ, Φ and β in gas phases. A similar approach, was used on Au-substrate, where in 4 different rotation angles θ, Φ, α and β are defined I also demonstrate how θ, Φ, α and β axes pass through the metallic moieties and investigateing how the total energy varies with the angle of rotation, both in presence and absence of a gold substrate. For each of the 4 axes, I consider one mode of rotation in the gas phase and three modes of rotation on a substrate.

In chapter 5, the electrical conductance and Seebeck coefficient of three endohedral metallofullerenes (EMFs) $Sc_3N@C_{80}$, $Sc_3C_2@C_{80}$, and $Er_3N@C_{80}$, are thoroughly investigated and it is found that their standard deviations are correlated with the degree of structural variations and the degree of charge inhomogeneity on the fullerene cages.

All EMFs studied are bi-thermoelectric systems, exhibiting both positive and negative Seebeck coefficients, in contrast to the empty C_{60}. The distance d between the top-most plane of the Au substrate and the closest metallic atom fluctuates due to rotations on the surface and the degree of variation is characterised by the associated standard deviation σ, which is a purely geometric quantity. Similarly, the degree of charge inhomogeneity on the fullerene cage can be characterised by a standard deviation σ_q.

In chapter 5, I also prove that standard deviations in the Seebeck coefficients σ_S of EMF-based junctions are correlated with the geometric quantity σ and the charge inhomogeneity σ_q. I benchmark these molecules against C_{60} and find that all of σ_q, σ_S are the largest for $Sc_3C_2@C_{80,}$ all are the smallest for C_{60} and for the other EMFs. This means that external measurements of fluctuations in the Seebeck coefficient provide insight into the internal structure and charge distribution of endohedral metallofullerene.

Bibliography

1. Scheer, E. (2013). Visions for a molecular future. *Nature Nanotechnology, 8(6), 386.*
2. Aradhya, S. V., and Venkataraman, L. (2013). Single-molecule junctions beyond electronic transport. *Nature nanotechnology*, 8(6), 399.
3. T. Prodromakis, C. Toumazou, and L. Chua, (2012). Two centuries of memristors, *Nature Materials*, vol. 11, no. 6, pp. 478–481.
4. Ismael, A. K., & Lambert, C. J. (2019). Single-molecule conductance oscillations in alkane rings. *Journal of Materials Chemistry C, 7*(22), 6578-6581.
5. Naghibi, S., Ismael, A. K., Vezzoli, A., Al-Khaykanee, M. K., Zheng, X., Grace, I. M., Bethell, D., Higgins, S. J., Lambert, C. J. and Nichols, R. J. (2019). Synthetic control of quantum interference by regulating charge on a single atom in heteroaromatic molecular junctions. *The journal of physical chemistry letters*, *10*(20), 6419-6424.
6. Lambert, C. J. (2015). Basic concepts of quantum interference and electron transport in single-molecule electronics. *Chemical Society Reviews*, 44(4), 875-888.
7. Aviram, A., and Ratner, M. A. (1974). Molecular rectifiers. *Chemical physics letters*, 29(2), 277-283.
8. Lafferentz, L., Ample, F., Yu, H., Hecht, S., Joachim, C., and Grill, L. (2009). Conductance of a single conjugated polymer as a continuous function of its length. *Science*, 323(5918), 1193-1197.
9. Batra, A., Darancet, P., Chen, Q., Meisner, J. S., Widawsky, J. R., Neaton, J. B., and Venkataraman, L. (2013). Tuning rectification in single-molecular diodes. *Nano letters*, 13(12), 6233-6237.
10. Chen, J., Wang, W., Reed, M. A., Rawlett, A. M., Price, D. W., and Tour, J. M. (2000). Room-temperature negative differential resistance in nanoscale molecular junctions. *Applied physics letters*, 77(8), 1224-1226.

11. Li, C., Pobelov, I., Wandlowski, T., Bagrets, A., Arnold, A., and Evers, F. (2008). Charge transport in single Au vertical bar alkanedithiol vertical bar Au junctions: Coordination geometries and conformational degrees of freedom. *Journal of the American Chemical Society*, 130(1), 318-326.

12. Hong, W., Manrique, D. Z., Moreno-García, P., Gulcur, M., Mishchenko, A., Lambert, C. J., and Wandlowski, T. (2012). Single molecular conductance of tolanes: experimental and theoretical study on the junction evolution dependent on the anchoring group. *Journal of the American Chemical Society*, 134(4), 2292-2304.

13. Warner, J. H. (2015). Detailed Atomic Structure of Defects in 2D Materials: From Graphene to Transition Metal Dichalcogenides. *Microscopy and Microanalysis*, 21(S3), 573-574.

14. Li, Y., Baghernejad, M., Qusiy, A. G., Zsolt Manrique, D., Zhang, G., Hamill, J., and Lambert, C. (2015). Three-state single-molecule naphthalenediimide switch: integration of a pendant redox unit for conductance tuning. *Angewandte Chemie*, 127(46), 13790-13793.

15. Rincón-García, L., Ismael, A. K., Evangeli, C., Grace, I., Rubio-Bollinger, G., Porfyrakis, K., and Lambert, C. J. (2016). Molecular design and control of fullerenebased bi-thermoelectric materials. *Nature materials*, 15(3), 289-293.

16. Yzambart, G., Rincón-García, L., Al-Jobory, A. A., Ismael, A. K., Rubio-Bollinger, G., Lambert, C. J., and Bryce, M. R. (2018). Thermoelectric Properties of 2, 7-Dipyridylfluorene Derivatives in Single-Molecule Junctions. *The Journal of Physical Chemistry* C, 122(48), 27198-27204.

17. Massonnet, N., Carella, A., Jaudouin, O., Rannou, P., Laval, G., Celle, C., and Simonato, J. P. (2014). Improvement of the Seebeck coefficient of PEDOT: PSS by

chemical reduction combined with a novel method for its transfer using free-standing thin films. *Journal of Materials Chemistry* C, 2(7), 1278-1283.

18. González, M. T., Ismael, A. K., Garcia-Iglesias, M., Leary, E., Rubio-Bollinger, G., Grace, I., Rodriguez, D., Torres, T., Lambert, C. J., and Agrait, N. (2021). Interference Controls Conductance in Phthalocyanine Molecular Junctions. *The Journal of Physical Chemistry C*, *125*(27), 15035-15043.
19. Finch, C. M., Garcia-Suarez, V. M., and Lambert, C. J. (2009). Giant thermopower and figure of merit in single-molecule devices. *Physical review* b, *79*(3), 033405.
20. Bergfield, J. P., Solis, M. A., and Stafford, C. A. (2010). Giant thermoelectric effect from transmission supernodes. *ACS nano*, *4*(9), 5314-5320.
21. Stevenson, S., Rice, G., Glass, T., Harich, K., Cromer, F., Jordan, M. R., Craft, J., Hadju, E., Bible, R., Olmstead, M. M. and Dorn, A. H. (1999). Small-bandgap endohedral metallofullerenes in high yield and purity. *Nature*, *401*(6748), 55-57.
22. Nörenberg, C., Leigh, D. F., Cattaneo, D., Porfyrakis, K., Bassi, A. L., Casari, C. S., Passoni, M., Owen, J. H., and Briggs, G. A. D. (2008, March). Self-assembly and electronic effects of Er3N@ C80 and Sc3N@ C80 on Au (111) and Ag/Si (111) surfaces. *In Journal of Physics: Conference Series* (Vol. 100, No. 5, p. 052080). IOP Publishing.
23. Kroto, H. W., Heath, J. R., O'Brien, S. C., Curl, R. F., and Smalley, R. E. (1985). C_{60}: buckminsterfullerene. *nature*, *318*(6042), 162-163.
24. Chai, Y., Guo, T., Jin, C., Haufler, R. E., Chibante, L. F., Fure, J., Lihong, W, Michael, A, and Smalley, R. E. (1991). Fullerenes with metals inside. *The Journal of Physical Chemistry*, *95*(20), 7564-7568.
25. Shinohara, H. (2000). Endohedral metallofullerenes. *Reports on Progress in Physics*, *63*(6), 843.

26. Guha, S., and Nakamoto, K. (2005). Electronic structures and spectral properties of endohedral fullerenes. *Coordination Chemistry Reviews*, *249*(9-10), 1111-1132.
27. Ismael, A. K., Rincón-García, L., Evangeli, C., Dallas, P., Alotaibi, T., Al-Jobory, A. A., Bollinger, G., Profyrakis, K., Agrait, N., and Lambert, C. J. (2022). Exploring seebeck-coefficient fluctuations in endohedral-fullerene, single-molecule junctions. *Nanoscale Horizons*.

Chapter 2

Density Functional Theory

This chapter introduces the density functional theory (DFT) formalism as well as the SIESTA DFT code, which is employed in all of the electronic structure computations in this thesis. The initial step in determining the molecule's electron transport characteristics is to use DFT to obtain a mean-field Hamiltonian. However, since the Hamiltonian only pertains to the isolated molecule, it must still be linked to semi-infinite leads, as described in the next chapter.

2.1 Introduction

It is necessary to have a reliable source of structural and electronic information in order to describe the behaviour of molecular electronic devices. In this chapter, I will give a brief summary of density functional theory (DFT) and the SIESTA (Spanish Initiative for Electronic Simulations with Thousands of Atoms) code [1], which I utilised extensively during my PhD studies as a theoretical tool for investigating both qualitatively and quantitatively the architectures of molecules, charge densities, and band structures. SIESTA is a collection of algorithms and a fully integrated software programme for performing DFT calculations on a large number of atoms (1000) in a matter of hours, days, or weeks. The fundamental principle of DFT is that every physical attribute of a complex system composed of several interacting particles can be represented as a function of the system's ground state density. The proof of the existence of such a functional was first presented by Hohenberg and Kohn [2] in 1964. However, the proof does not provide us any information on the shape of the functional. However, an ansatz proposed by Kohn and Sham [3] opened the door to applications for realistic physical systems. Since then, DFT has been a common tool in theoretical physics and molecular chemistry. This chapter will give an overview of the principles of DFT and all of its numerical applications. The literature is quite broad and deals with the subject with considerably more detail [4-7]. I will begin by outlining the several alternative approaches to the many body issue, and then I will demonstrate the Hartree-Fock

technique and the Hohenberg-Kohn theorems, followed by a demonstration of the Kohn-Sham ansatz. Next, I distil the most often used functional forms, which are critical in applied numerical analysis. I also focus on localised base sets, pseudo-atomic orbits defining the number space of the Hilbert computations in this thesis, and Basis Set Superposition Error Correction (BSSE) and Counterpoise Correction (CP).

2.2 The Schrödinger Equation and Variational Principle

The Schrödinger equation, which is time independent and non-relativistic, may be used to describe any non-relativistic multi particle system:

$$\mathrm{H}\psi_i(\vec{r}_1,\vec{r}_2,\dots,\vec{r}_N,\vec{R}_1,\vec{R}_2,\dots,\vec{R}_M = E_i\psi_i(\vec{r}_1,\vec{r}_2,\dots,\vec{r}_N,\vec{R}_1,\vec{R}_2,\dots,\vec{R}_M) \tag{2.1}$$

Where ψ_i is the wavefunction of the i^{th} state of the system and E_i is the numerical value of the energy of the state represented by ψ_i represents the Hamiltonian operator of a system consisting of N-electrons and M-nuclei that explains the interaction of particles with each other. The Hamiltonian operator of such a system can be written as a sum of five terms given by [2, 3, 8-12]:

$$\begin{aligned} &= \overbrace{-\frac{\hbar^2}{2m_e}\sum_{i=1}^{N}\nabla_i^2}^{T_e} - \overbrace{\frac{\hbar^2}{2m_n}\sum_{n=1}^{M}\nabla_n^2}^{T_n} - \overbrace{\frac{1}{4\pi\varepsilon_o}\sum_{i=1}^{N}\sum_{n=1}^{M}\frac{1}{|\vec{r}_i-\vec{R}_n|}Z_n e^2}^{U_{en}} \\ &\quad + \overbrace{\frac{1}{8\pi\varepsilon_o}\sum_{i=1}^{N}\sum_{i\neq j}^{N}\frac{e^2}{|\vec{r}_i-\vec{r}_j|}}^{U_{ee}} + \overbrace{\frac{1}{8\pi\varepsilon_o}\sum_{n=1}^{M}\sum_{n\neq n'}^{M}\frac{Z_n Z_{n'} e^2}{|\vec{R}_n-\vec{R}_{n'}|}}^{U_{nn}} \end{aligned} \tag{2.2}$$

Where i and j denote the N-electrons while n and $\acute{n}$ run over the M-nuclei in the system, m_e and m_n are the mass of electron and nucleus respectively, e and Z_e are the electron and nuclear charge respectively. The position of the electrons and nuclei are denoted as $\vec{r}_i$ and $\vec{R}_n$ respectively, and ∇^2 is the Laplacian operator, in Cartesian coordinates is defined as

$$\nabla_i^2 = \frac{\partial^2}{\partial x_i^2} + \frac{\partial^2}{\partial y_i^2} + \frac{\partial^2}{\partial z_i^2}$$

According to the illustration given by the equation (2.2), the terms, T_e is the kinetic energy of electrons, while T_n is denoted as kinetic energy of nuclei in the system. Additionally, the last three terms describe the potential part of the Hamiltonian; the term U_{en} represents the attractive electrostatic interaction between nuclei and electrons in the system. The electron-electron(U_{ee}) and nuclear-nuclear (U_{nn}) are the repulsive part of the potential respectively [1, 3, 4, 9, 11]

The Born-Oppenheimer approximation, also known as the clamped nuclei approximation, may be used in the analysis because about 99.9% of the mass of an atom is contained in the nucleus; also, the nuclei in the system can be regarded fixed in comparison to the electrons. This implies, for example, that the hydrogen atom's mass concentration is shown by the fact that the nucleus weighs about 1800 times more than the electron. If the nuclei of the treated atoms are maintained stable, the resultant kinetic energy accumulates to zero, implying that they no longer contribute to the complete wave-function.
As a consequence of the preceding assumption, the electron system's Hamiltonian expression decreases the Hamiltonian to a different figure; similarly, the electronic Hamiltonian H_{ele}, which in a fixed nuclear representation may well be given by [3, 4, 9, 11]:

Where; the U_{nn} is an obtained constant for the system. The Schrödinger equation for 'clamped-nuclei'

$$\mathrm{H}_{ele} = \overbrace{-\frac{\hbar^2}{2m_e}\sum_{i=1}^{N}\nabla_i^2}^{T_e} \overbrace{-\frac{1}{4\pi\varepsilon_o}\sum_{i=1}^{N}\sum_{n=1}^{M}\frac{1}{|\vec{r}_i-\vec{R}_n|}Z_n e^2}^{U_{en}} + \overbrace{\frac{1}{4\pi\varepsilon_o}\frac{1}{2}\sum_{i=1}^{N}\sum_{i\neq j}^{N}\frac{e^2}{|\vec{r}_i-\vec{r}_j|}}^{U_{ee}} + \overbrace{\frac{1}{4\pi\varepsilon_o}\frac{1}{2}\sum_{i=1}^{M}\sum_{n\neq n'}^{M}\frac{Z_n Z_{n'} e^2}{|\vec{R}_n-\vec{R}_{n'}|}}^{U_{nn}} \quad (2.3)$$

is represented as:

$$\mathrm{H}_{ele}\psi_{ele} = E_{ele}\psi_{ele} \quad (2.4)$$

Where; ψ_{ele} is dependent on the electron coordinates for the system, while the nuclear part enters only dimensionally and does not clearly appear in ψ_{ele}.

Total energy E_{total} is given as the sum of E_{ele} and the constant nuclear repulsion term for the system which is given as:

$$E_{total} = E_{ele} + U_{nn} \quad (2.5)$$

Wave-function for a system is not an observable quantity, its modulus squared can be written in the form as:

$$|\psi(\vec{r}_1, \vec{r}_2, \dots, \vec{r}_N)|^2 d\vec{r}_1\, d\vec{r}_2 \dots d\vec{r}_N \quad (2.6)$$

The above expression represents the fact that the probability that electrons 1, 2…, *N* are found in the volume elements$d\vec{r}_1\, d\vec{r}_2 \dots\dots d\vec{r}_N$, this is because the electrons are indistinguishable, and this probability is unchangeable if the coordinates of any two of electrons (*i* and *j*) are swapped [15]:

$$\left|\psi(\vec{r}_1, \vec{r}_2, \dots \vec{r}_i, \vec{r}_j, \dots, \vec{r}_N)\right|^2 = \left|\psi(\vec{r}_1, \vec{r}_2, \dots \vec{r}_j, \vec{r}_i, \dots, \vec{r}_N)\right|^2 \quad (2.7)$$

Because of the reason that electrons are fermions with spins of a half then the value of ψ must therefore be anti-symmetric with respect to the interchange of the spatial and the spin coordinates as well in any pair of electrons:

$$\psi(\vec{r}_1, \vec{r}_2, \dots \vec{r}_i, \vec{r}_j, \dots, \vec{r}_N) = -\psi(\vec{r}_1, \vec{r}_2, \dots \vec{r}_i, \vec{r}_j, \dots, \vec{r}_N) \tag{2.8}$$

A logical result of probability interpretation format of the wave-function is that the integral of equation 2.6 over the full range of all variables gives an output of one**.** This mean, the probability of finding the *N*-electron at any position in a space must be exactly unity,

$$\int \dots \int |\psi(\vec{r}_1, \vec{r}_2, \dots, \vec{r}_N)|^2 \, d\vec{r}_1 \, d\vec{r}_2 \dots d\vec{r}_N = 1 \tag{2.9}$$

A wave-function that meets the requirements for equation (2.9) is a normalized one.

Since the Schrödinger wave-equation does not have an exact solution, several theories have been developed to fulfil this objective; this effort start with Hartree, Hartree-Fock and many others. A large number of these theories were based on a significant theoretical principle referred to as variational principle of the wave-function where this principle leads an analysts on how to look for solutions by using suitable trial wave-functions ψ_{Tri} [11]. The above principle is meaningful in the study of the ground state, but is not very fruitful in the study of excited states. When a system is in the state ψ_{Tri}, the expectation value of the energy is given by the expression:

$$\langle E_{Tri} \rangle = \frac{\int \psi_{Tri} \mathrm{H} \, \psi^*_{Tri} \, d\vec{r}}{\int \psi_{Tri} \, \psi^*_{Tri} \, d\vec{r}} \tag{2.10}$$

$$\langle E_{Tri} \rangle = \frac{\int \psi_{Tri} \mathrm{H} \, \psi^*_{Tri} \, d\vec{r}}{\int \psi_{Tri} \, \psi^*_{Tri} \, d\vec{r}} \tag{2.11}$$

Variational principle that is given in the equation 2.10 implies that the energy computes as the expectation value of the Hamiltonian operator from any ψ_{Tri} that is an upper bound of the true ground-state energy ψ_{GS}. Suppose ψ_{Tri} is normalized as per the equation 2.9 while ψ_{Tri} then it equals to the ground state ($\psi_{Tri} = \psi_{GS}$). This indicates that entity E_{Tri} is equal to the exact ground state energy E_{GS}, additionally, we can reconfigure the equation 2.10 for the ground state as:

$$\langle E_{GS} \rangle = \int \psi_{GS} \, \mathrm{H} \, \psi_{GS}^{*} \, d\vec{r} \qquad (2.12)$$

From the normalized ψ_{Tri} we can clarify that $E_{Tri} > E_{GS}$ or $E_{Tri} = E_{GS}$. The best chose for E_{Tri} is therefore the one in which E_{Tri} is reduced [3].

2.3 The Hohenberg-Kohn Theorems

P. Hohenberg and W. Kohn demonstrated in 1964 [2] that there is a relationship between the ground state energy and the density, $\rho(r)$,of an interacting electron system. The Hohenberg-Kohn theorems are two simple but strong statements:

a) The external potential, V_{ext}, is a density-specific functional (r). Given that V_{ext} fixes the system's Hamiltonian, H, it is obvious that the complete many-body ground state is a unique functional of $\rho(r)$.

b) The ground state, E_{HK} , is a ground state density $\rho(r)$.

It is a straightforward matter of reduction ad absurdum to demonstrate the validity of the first theorem presented above. Assume we have two external potentials, V_{ext}^{1} and V_{ext}^{2}, that vary by a constant. Assume that the two external potentials provide the same ground-state density $\rho(r)$. Each system's Hamiltonians are designated by $H^{(1)}$ and $H^{(2)}$ and, since they vary, they will have distinct ground-state wavefunctions, $\psi^{(1)}$ and $\psi^{(2)}$. We have $\psi^{(2)}$ since it is not a ground state of $H^{(1)}$, we have:

$$E^{(1)} = \langle \psi^{(1)} | H^{(1)} | \psi^{(1)} \rangle < \langle \psi^{(2)} | H^{(1)} | \psi^{(2)} \rangle \tag{2.13}$$

Similarly:

$$E^{(2)} = \langle \psi^{(2)} | H^{(2)} | \psi^{(2)} \rangle < \langle \psi^{(1)} | H^{(1)} | \psi^{(1)} \rangle \tag{2.14}$$

The simplified assumption is that our ground states are non-degenerate. The problem has been formulated to incorporate degeneracies in the literature [10, 17]. We can rewrite equation 2.14:

$$\begin{aligned} \langle \psi^{(2)} \left| H^{(1)} \right| \psi^{(2)} \rangle &= \langle \psi \left| H^{(2)} \right| \psi^{(2)} \rangle \langle \psi^{(2)} \left| H^{(1)} - H^{(2)} \right| \psi^{(2)} \rangle \\ &= E^{(2)} + \int dr \left(V_{ext}^{(1)}(r) - V_{ext}^{(2)}(r) \right) \rho_o(r) \end{aligned} \tag{2.15}$$

Also, equation 2.15:

$$\langle \psi^{(2)} \left| H^{(1)} \right| \psi^{(2)} \rangle = E^{(2)} + \int dr \left(V_{ext}^{(1)}(r) - V_{ext}^{(2)}(r) \right) \rho o\ (r) \tag{2.16}$$

When we combine equations 2.14 and 2.15, we get the following contradiction:

$$E^{(1)} + E^{(2)} < E^{(1)} + E^{(2)}$$

Two or more potentials may vary by no more than a constant and can produce the same ground-state density, hence it is impossible for there to be two such potentials.

The second theorem is just as easy to prove as the first. Consider the following equation for the system's total energy, E:

$$E(\rho) = T(\rho) + E_{int}(\rho) + \int dr V_{ext}(\rho)(r) \tag{2.17}$$

The kinetic term, T and internal interaction of the electrons, E_{int} , are, by definition, universal.

Consider a system with a ground-state density of ρ_o , an external potential of V_{ext} , and a wavefunction of ψ_0 . According to the first theorem, ρ_o determines the Hamiltonian, therefore for any density and wavefunction, ψ, other than the ground state, we get:

$$E_o = \langle\psi_0|H|\psi_0\rangle < \langle\psi|H|\psi\rangle = E \tag{2.18}$$

This reduces the functional density of the ground, ρ_o, equation 2.18. As a result, if we know the functional: $T(\rho) + E_{int}(\rho)$, we can extract the ground-state of the system and compute all ground-state attributes by minimising equation 2.18.

2.4 The Kohn-Sham Theorems

We have already shown that by acquiring the ground-state density, we can calculate the ground-state energy, and it is theoretically possible to compute the ground-state energy by getting the ground-state density. The precise form of the functional indicated in equation 2.18, however, is unknown. The kinetic term as well as the internal energy of the interacting particles cannot be represented as a function of density in general. The solution was introduced by Kohn and Sham in 1965 [3].

The original Hamiltonian can be substituted, according to Kohn and Sham, with an effective Hamiltonian of non-interacting particles, with a real external potential having the same ground-state density as the original system. Because this is not a defined recipe, it is merely an ansatz, but a non-interacting problem is far easier to resolve. Contrary to equation 2.18, the functional energy of the ansatz Kohn-Sham will have the formula:

$$E_{KS}(\rho) = T_{KS}(\rho) + + \int drV_{ext}(r)\rho(r) + E_H(\rho) + E_{xc}(\rho) \tag{2.19}$$

T_{KS} is the non-interacting system's kinetic energy. The kinetic energy of the interacting system was employed in equation 2.18. T the distinction is known as the exchange correlation functional, E_{xc} , equation 2.21.

The Hartree functional, E_H , represents the electron-electron interaction using the Hatree-Fock method and has the following form:

$$E_H(\rho) = \frac{1}{2}\int \frac{\rho(r)\rho(r')}{|r-r'|}\, drdr' \tag{2.20}$$

This is a roughly E_{int} version, as previously defined. Again, E_{xc} refers to the difference. As a result, the exchange correlation functional, E_{xc} , represents the difference between the exact and approximation solutions to the kinetic energy term and the electron-electron interaction term. Its definition is as follows:

$$E_{xc}(\rho) = \big(E_{int}(\rho) - E_H(\rho)\big) + \big(T(\rho) - T_{KS}(\rho)\big) \tag{2.21}$$

In practice, the first three functionals of equation 2.19 are easily defined and account for the majority of the contribution to ground-state energy. In comparison, the exchange correlation functional makes a minor contribution. Despite decades of investigation, there is no exact remedy. The next part discusses several excellent approximations that have been developed.

2.5 The Exchange Correlation Functionals

Several modifications on the exchange and correlation energy have been published in the literature. The first successful form was the Local Density Approximation (LDA) [26, 27], That depends on the density only, and hence is functional locally. Then the next step was the Generalized Gradient Approximation (GGA) [17-20], Including the density derivative, it also includes neighbourhood information and is thus semi-local.

One of the most commonly used approximations in density functional theory is LDA and GGA.LDA and GGA can't be considered the only possible functionals. Some of these functionals are tailored to fit specific needs of basis sets used in solving the Kohn-Sham equations, equation 2.12 and a large category is the so-called hybrid functionals (e.g. B3LYP [3], HSE [30] and Meta hybrid GGA [29, 31]), which combine the LDA and GGA forms.

One of the most recent and universal features, the Van der Waals density functional (vdW-DF) [32], contains non-local terms and has proven to be very accurate in systems where dispersion forces are important [33, 34].

Following sections will provide a brief introduction to the Local Density Approximation and the Generalized Gradient Approximation.

2.5.1 Local Density Approximation (LDA)

The exchange correlation functional in LDA simply depends on the local density. This approximation can be expected to produce satisfactory results for systems where the density is does not change too rapidly.

In some ways, the LDA is the most basic representation of the exchange and correlation energy. It is a basic yet powerful functional, and it is known to be correct for graphene and carbon nanotubes, as well as where the electron density is not changing rapidly. For example, for atoms that have d and f-type orbits, a bigger inaccuracy is expected. But LDA has numerous drawbacks: the band gap in semiconductors and insulators is sometimes underestimated with a significant inaccuracy (alternative to 10 –30%), for example. For instance. So, it is advisable to try to improve your functionality.

2.5.2 Generalized Gradient Approximation (GGA)

When derivatives are included in the functional form of the exchange and correlation energies the GGA is obtained. In this condition there is no closed form for the functional exchange, so analytical solutions have to have been used to calculate the correspondence contributions. Just as in the case of the LDA there exist many parameterizations for the exchange and correlation energies in GG [17- 19, 35].

For the approximation of exchange-correlation energies in the DFT, LDA and GGA are two of the most widely utilized approximations. Several functionalities, beyond LDA and GGA, are also provided. In overall, the validity of these functions is not a sensible theory. Tests are performed on diverse materials to test functional properties for a wide range of systems and then statistical comparisons are performed to establish valid data.

2.6 Pseudopotentials

I have demonstrated how to transform a huge interacting problem into an effective non-interacting problem using the Kohn Sham formalism and an exchange-correlation functional. This greatly simplifies the situation from a physical point of view. When molecules with a significant number of atoms are involved, however, the calculation becomes too massive and computationally intensive to use. By introducing pseudopotentials, the number of core electrons in an atom can be reduced. Pseudopotentials were first introduced by Fermi in 1934 [19, 20] and since then methods have evolved from creating not so realistic empirical pseudopotentials [21, 22] to more realistic ab-initio pseudopotentials [22, 24].

Electrons, which are commonly found in the nucleus of an atom, can be classified into two types: core and valence. Core electrons are found within the nucleus while the valence electrons are located in partially filled atomic shells. As long as core electrons are restricted around the nucleus, the only valence electron states overlap when atoms are brought together. This makes it possible to remove the core electron and replace it with a pseudopotential that allows the valence electrons to still be screened

as if the core electrons are still present. This dramatically lowers the number of electrons in a system and reduces the time and stored properties of molecules that contain a significant number of electrons.

2.7 Basis Sets

Obviously, the Hamiltonian must be diagonalized to find the wavefunctions. This procedure includes inverting a big matrix. The Hamiltonian must be sparse with several zeros for effective calculations. SIESTA uses a Linear Atomic Orbital Combination (LCAO) basis set, which decays to zero after a certain specified cut-off radius, and is created from atom orbitals. As the overlap between basis functions is reduced, the former produces the required sparse form of the Hamiltonian, even if the latter allows even a slight basis set to produce similar properties with that of the studied system. The simplest form of the atomic basis set for an atom is called a single ξ basis, which corresponds to a single basis function, $\psi_{nlm(r)}$ per electron orbital. In this case each basis function consists of a product of one radial wavefunction, Φ^1_{nl} and spherical harmonic Y_{lm}:

$$\psi_{nlm(r)} = \Phi^1_{nl}(r) Y_{lm}(\theta, \Phi) \tag{2.22}$$

The radial part of the wavefunction is found by using the method proposed by Sankey [25], where the Schrodinger equation is solved for the atom placed inside a spherical box. It is under the constraint to vanish at a cut-off radius r_c. This constraint produces an energy shift δE within the Schrödinger equation such that the eigen functions first node occurs at r_c:

$$\left[-\frac{d^2}{dr^2} + \frac{l(l+1)}{2r^2} + V^{ion}_{nl}(r)\right] \Phi^1_{nl}(r) = (\varepsilon_{nl} + \delta E)\, \Phi^1_{nl}(r)) \tag{2.23}$$

For higher accuracy basis sets, multiple, additional radial wavefunctions can be included for each electron orbital. The additional radial wavefunctions, Φ_{nl}^{i} for > 1 , are calculated using a split-valence method. This involves defining a split valence cut off for each additional wavefunction, r_s^i , so it is split into two piecewise functions: a polynomial below the cut-off and the previous basis wavefunction above it:

$$\Phi_{nl}^{1}(r) = \begin{cases} r^l(a_{nl} - b_{nl}r^2) & r < r_s^i \\ \Phi_{nl}^{i-1} & r_s^i < r < r_s^{i-1} \end{cases} \tag{2.24}$$

Further parameters are located at the point when such wavefunction and its derivative are supposed to be continuous.

Further accuracy (multiple-ξ polarized) can be obtained by including wavefunctions with different angular momenta corresponding to orbitals which are unoccupied in the atom. This is done by solving Eq. 2.23 in an electric field such that the orbital is polarized or deformed due to the field (see [6] for details) so a different radial function is obtained. This is now combined with the appropriate angular dependent spherical harmonic which increases the size of the basis. Table 2.1 shows the number of basis orbitals for a selected number of atoms for single-ξ , single-ξ polarised, double-ξ , double-ξ polarised.

Table 2.1: Example of the number of radial basis functions per atom as used within the SIESTA for different degrees of precision.

Atom	**Valence configuration**	**SZ**	**SZP**	**DZ**	**DZP**
H	$1s$	1	4	2	5
C	($2s^2$ $2P^2$)	4	9	8	13
S	($3S^2$ $3P^4$)	4	9	8	13
Au	($6S^1$ $5d^{10}$)	6	9	12	15

2.8 Basis Set Superposition Error Correction (BSSE) and Counterpoise Correction (CP)

Basis Set Superposition Error Correction (BSSE) is one of the fundamental factors that impact the precision of energy interactions calculations with incomplete bases. It is usually understood in addition to intermolecular interactions, particularly for systems that have weak intermolecular interactions. The SIESTA implementation of DFT, applied in this thesis, means that the BSSE starts employing the linear combination of the atomic orbital formalism, consisting of a final nuclei-focusing basis when atoms are close enough to overlap their basis functions. This may artificially reinforce the atomic connection and artificially shorten the atomic distances and so alter the overall system energy.

In1970, Boys and Bernardi presented a method of reducing BSSE in molecular complexes made up of a so-called counterpoise-correction scheme [25, 26, 29] with two geometrical configurations. Consider two molecular systems A and B, separated by a distance R. The interactive energy can be expressed in [28]

$$\Delta E_{inter}^{AB}(R) = E^{AB}(R) - E^{A} - E^{B} \qquad (2.25)$$

where ΔE_{inter} AB is the overall energy of the supersystem, E^A and E^B are the energies of the isolated subsystems [32]. Figure 2.1 highlights the counterpoise correction for dimers A and B.

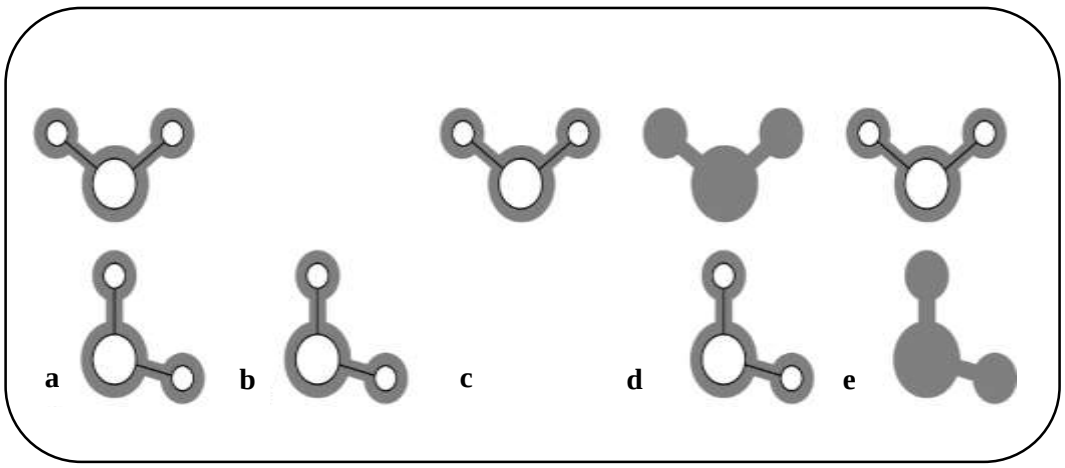

Figure 2.1. Illustrating the Counterpoise method to calculate the binding energy. (**a**) represents the basis functions for a total system where atoms are shown in white, and the basis functions are in grey. (**b**) and (**c**) show the basis function for the individual monomers whereas (**d**) and (**e**) represent the counterpoise correction. Every single molecule is evaluated with the same basis function as the total system in (**a**) [30].

Figures 2.1 a, b and c represent the two isolated molecules with their individual and corresponding basis functions, while the shaded grey atoms in figure 2.1 d and e represent the ghost states (basis set functions having no electrons or protons). The Basis Set Superposition Error Correction (BSSE) is calculated by recalculating the binding energy E_{Bin} using the mixed basis sets obtained by introducing the ghost orbitals and then reducing the error from the uncorrected energy.

$$E_{Bin} = E_a - (E_d + E_e) \tag{2.26}$$

where E_a, E_d and E_e are the total energy of (a), (d) and (e) systems in figure 2.1, respectively. In what follows, this an important concept that has been successfully implemented in many systems to give reliable and realistic energies [26, 35, 38].

2.9. Conclusion

In conclusion, I have presented a summary of the DFT formalism and the SIESTA DFT code, which is used throughout this thesis to compute the electronic structure. The first step in identifying the electron transport properties of a molecule is to obtain a DFT mean-field Hamiltonian describing the isolated molecule. The next step is to connect the molecule, to semi-infinite leads, as will be explained in the next chapter.

Bibliography

1. Soler, J. M., Artacho, E., Gale, J. D., García, A., Junquera, J., Ordejón, P., and Sánchez-Portal, D. (2002). The SIESTA method for ab initio order-N materials simulation. *Journal of Physics: Condensed Matter*, *14*(11), 2745.
2. Hohenberg, P., and Kohn, W. (1964). Inhomogeneous electron gas. *Physical review*, *136*(3B), B864.
3. Kohn, W., and Sham, L. J. (1965). Self-consistent equations including exchange and correlation effects. *Physical review*, *140*(4A), A1133.
4. Gross, E. K., Runge, E., and Heinonen, O. H (1991). Many Particle Theory.
5. Probert, M. (2011). Electronic Structure: Basic Theory and Practical Methods, by Richard M. Martin: Scope: graduate level textbook. Level: theoretical materials scientists/condensed matter physicists/computational chemists.
6. Gross, E.K. and R.M. Dreizler. (1995). *Density functional theory*. Vol. 337: Springer.
7. Parr, R. G., and Weitao, Y. (1989). Chemical potential derivatives. In *Density-Functional Theory of Atoms and Molecules*. Oxford University Press.
8. Born, M., and Oppenheimer, R. (1927). On the quantum theory of molecules. *Annalen der Physik*, 84:20.
9. Levy, M., and Perdew, J. P. (1985). The constrained search formulation of density functional theory. In *Density functional methods in physics* (pp. 11-30). *Springer, Boston*, MA.
10. Levy, M. (1982). Electron densities in search of Hamiltonians. *Physical Review A*, *26*(3),1200.
11. Martin, R. M. (2020). *Electronic structure: basic theory and practical methods*. Cambridge university press.
12. Griffiths, D. J. (2005). *Introduction to quantum mechanics*. Pearson Prentice Hall.

13. Fermi, E. (1934). Sopra lo spostamento per pressione delle righe elevate delle serie spettrali. *Il Nuovo Cimento (1924-1942)*, *11*(3), 157-166.

14. Fermi, E. (1936). Motion of neutrons in hydrogenous substances. *Ricerca Scientifica*, *7*(2), 13-52.

15. Levy, M. (1979). Universal variational functionals of electron densities, first-order density matrices, and natural spin-orbitals and solution of the v-representability problem. *Proceedings of the National Academy of Sciences*, *76*(12), 6062-6065.

16. Levy, M. (1985). Density Functional Methods in Physics. *The inhomogeneous electron gas*, 32-94.

17. Becke, A. D. (1988). Density-functional exchange-energy approximation with correct asymptotic behavior. *Physical review A*, *38*(6), 3098.

18. Hammer, B. H. L. B., Hansen, L. B., and Norskov, J. K. (1999). Improved adsorption energetics within density-functional theory using revised Perdew-Burke-Ernzerhof functionals. *Physical review B*, *59*(11), 7413.

19. Perdew, J. P., Burke, K., and Ernzerhof, M. (1996). Generalized gradient approximation made simple. *Physical review letters*, *77*(18), 3865.

20. Ismael, A., Wang, X., Bennett, T., Wilkinson, L., Robinson, B., Long, N., Cohen, L., and Lambert, C. J. (2020). Tuning the thermoelectrical properties of anthracene-based self-assembled monolayers. *Chemical science*, 11(26), 6836-6841.

21. Ismael, A. K., Al-Jobory, A., Grace, I., and Lambert, C. J. (2017). Discriminating single-molecule sensing by crown-ether-based molecular junctions. *The Journal of Chemical Physics*, *146*(6), 064704.

22. Lieb, E. H. (1982). Density functionals for coulomb systems. Physics as Natural Philosophy: Essays in Honor of Laszlo Tisza on His 75th Birthday. *A. Shimony and H. Feshbach (MIT, Cambridge, MA)*, 111.

23. Zunger, A., and Cohen, M. L. (1978). First-principles nonlocal-pseudopotential approach in the density-functional formalism: Development and application to atoms. *Physical Review B*, *18*(10), 5449.

24. Hamann, D. R., Schlüter, M., and Chiang, C. (1979). Norm-conserving pseudopotentials. *Physical Review Letters*, *43*(20), 1494.

25. Boys, S. F., and Bernardi, F. J. M. P. (1970). The calculation of small molecular interactions by the differences of separate total energies. Some procedures with reduced errors. *Molecular Physics*, *19*(4), 553-566.

26. Haynes, P. D., Skylaris, C. K., Mostofi, A. A., and Payne, M. C. (2006). Elimination of basis set superposition error in linear-scaling density-functional calculations with local orbitals optimised in situ. *Chemical physics letters*, *422*(4-6), 345-349.

27. Langreth, D. C., and Perdew, J. P. (1977). Exchange-correlation energy of a metallic surface: Wave-vector analysis. *Physical Review B*, *15*(6), 2884.

28. Senent, M. L., and Wilson, S. (2001). Intramolecular basis set superposition errors. *International journal of quantum chemistry*, *82*(6), 282-292.

29. Mierzwicki, K., and Latajka, Z. (2003). Basis set superposition error in N-body clusters. *Chemical physics letters*, *380*(5-6), 654-664.

30. Heyd, J., Scuseria, G. E., and Ernzerhof, M. (2003). Hybrid functionals based on a screened Coulomb potential. *The Journal of chemical physics*, *118*(18), 8207-8215.

31. Zhao, Y., and Truhlar, D. G. (2011). Applications and validations of the Minnesota density functionals. *Chemical Physics Letters*, *502*(1-3), 1-13.

32. Dion, M., Rydberg, H., Schröder, E., Langreth, D. C., and Lundqvist, B. I. (2004). Van der Waals density functional for general geometries. *Physical review letters*, *92*(24), 246401.

33. Klimeš, J., Bowler, D. R., and Michaelides, A. (2011). Van der Waals density functionals applied to solids. *Physical Review B, 83*(19), 195131.

34. Gantenbein, M., Wang, L., Al-Jobory, A. A., Ismael, A. K., Lambert, C. J., Hong, W., and Bryce, M. R. (2017). Quantum interference and heteroaromaticity of para-and meta-linked bridged biphenyl units in single molecular conductance measurements. *Scientific reports, 7*(1), 1-9.

35. Boese, A. D., Jansen, G., Torheyden, M., Höfener, S., and Klopper, W. (2011). Effects of counterpoise correction and basis set extrapolation on the MP2 geometries of hydrogen bonded dimers of ammonia, water, and hydrogen fluoride. *Physical Chemistry Chemical Physics, 13*(3), 1230-1238.

36. Lee, C., Yang, W., and Parr, R. G. (1988). Development of the Colle-Salvetti correlation-energy formula into a functional of the electron density. *Physical review B, 37*(2), 785.

37. Ceperley, D. M., and Alder, B. J. (1980). Ground state of the electron gas by a stochastic method. *Physical review letters, 45*(7), 566.

38. Daza, M. C., Dobado, J. A., Molina, J. M., Salvador, P., Duran, M., and Villaveces, J. L. (1999). Basis set superposition error-counterpoise corrected potential energy surfaces. Application to hydrogen peroxide X (X= F−, Cl−, Br−, Li+, Na+) complexes. *The Journal of chemical physics, 110*(24), 11806-11813.

Chapter 3

Single Particle Transport

Density functional theory, which may be used to determine the electrical structure of an isolated molecule, was discussed in chapter 2. Connecting this isolated molecule to semi-infinite leads and computing the transmission coefficient out across system are the next step. This is performed by using the Green's function scattering formalism, which I discuss in this chapter and which is employed throughout the thesis. The electric and thermoelectric characteristics of nanoscale systems sandwiched between a number of macroscopic sized metal electrodes are described using scattering theory and Green's function techniques.

3.1 Introduction

In this chapter, I begin with a brief overview of the Landauer formula. Subsequently, I introduce the simplest form of a retarded Green's function for a Scattering Theory in one-dimensional tight binding chain. After this, I break the periodicity of this lattice at a single connection and show that the Green's function is related directly to the transmission coefficient across the scattering region. The methods used on these simple systems will then be used to derive the transmission coefficient of mesoscopic conductors of arbitrarily complex geometry The method presented here assumes negligible interaction between carriers, the absence of inelastic processes, and zero temperature.

3.2 The Landauer Formula

The Landauer formula [1, 6] is used to describe electron transport in mesoscopic systems and is applicable to phase coherent systems, in the absence of inelastic scattering. It relates the conductance of a mesoscopic sample to the transmission properties of electrons passing through it. The method used to calculate the transmission properties will be discussed later in this chapter.

Figure 3.1. A mesoscopic scatterer linked to contacts with ballistic leads. μ_L and μ_R represent the chemical potential of the left and right contacts, respectively.

A mesoscopic scattering region connected to contacts by ballistic leads. The chemical potential in the contacts is μ_L and μ_R respectively. If an incident wave packet hits the scattering region from the left, it will be transmitted with probability $T = tt^*$ and reflected with probability $R = rr^*$. Charge conservation requires $T + R = 1$.

To begin, consider a mesoscopic scatter coupled to two contacts that operate as electron reservoirs through two ideal ballistic leads Figure 3.1. All inelastic relaxation processes are limited to the reservoirs [1]. The reservoirs have slightly different chemical potentials, μL and μR, such that $\mu L - \mu R$ is small. Here we use the notation $\mu L - \mu R = \delta E = e\delta V > 0$, which will drive electrons from the left to the right reservoir. Initially, I will discuss the solution for one open channel (i.e. where only one electron is allowed to travel in a given direction).

The incident current passing through this system from the left to the write reservoir is:

$$\delta \mathrm{I} = \mathrm{e}v \left(\frac{\partial \mathrm{n}}{\partial \mathrm{E}}\right)(\mu \mathrm{L} - \mu \mathrm{R}) \tag{3.1}$$

Where e is the electronic charge, v in the group velocity and $\frac{\partial \mathrm{n}}{\partial \mathrm{E}}$ is the density of states per unit lengthin the lead in the energy window defined by the chemical potentials of the contacts.

$$\frac{\partial \mathrm{n}}{\partial \mathrm{E}} = \frac{\partial \mathrm{n}}{\partial \mathrm{k}} \frac{\partial \mathrm{k}}{\partial \mathrm{E}} = \frac{\partial \mathrm{n}}{\partial \mathrm{k}} \frac{1}{v\hbar} \tag{3.2}$$

In one dimension, after including a factor of 2 for spin dependency, $\frac{\partial \mathrm{n}}{\partial \mathrm{k}} = \frac{1}{\pi}$ Substituting this Into Equation 3.2, we find that $\frac{\partial \mathrm{n}}{\partial \mathrm{k}} = \frac{1}{v\hbar}$. This simplifies Equation 3.1 to:

$$\delta I = \frac{2e}{h}(\mu_L - \mu_R) = \frac{2e^2}{h}\delta V \tag{3.3}$$

Where δV is the voltage generated by the chemical potential mismatch. From equation 3.3 it is clear that in the absence of a scattering region, the conductance of a quantum wire with one open channel is $\frac{2e^2}{h}$, which is approximately $77.5\mu S$ (or in other words, aresistance of 12.9 $k\Omega$). This is an everyday quantity; it typically appears on the circuit boards of everyday electrical appliances. If now we consider a scattering region, the current collected in the right contacts will be

$$\delta \mathrm{I} = \frac{2e^2}{h} T\delta V \rightarrow \frac{\delta I}{\delta V} = G = \frac{2e^2}{h} T \tag{3.4}$$

This is the well-known Landauer formula, relating the conductance, G of a mesoscopic scatterer to the transmission probability,T of the electrons traveling through it. It describes the linear response conductance, hence it only holds for small bias voltages $\delta V \approx 0$.

The Landauer formula has been generalized for the case of more than one open channel by Buttiker [3]. In this case the transmission coefficient is replaced by the sum of all the transmission amplitudes

describing electrons incoming from the left contactand arriving to the right contact. The Landauer formula equation 3.3 for many open channelshence becomes:

$$\frac{\delta \mathrm{I}}{\delta I} = G = \frac{2e^2}{h}\sum_{i,j}|t_{i,j}|^2 = \frac{2e^2}{h}Trace(tt^{\dagger}) \qquad (3.5)$$

Where t_{ij} is the transmission amplitude describing the scattering from the j^{th} channel of the left lead to the i^{th} channel of the right lead. With the definition of the transmission amplitudes, one can similarly introduce the reflection amplitudes r_{ij} which describe the scattering processes where theparticle is scattered from the j^{th} channel of the left lead to the i^{th} channel of the same lead. Combining reflection and transmission amplitudes, one can define the S matrix, which connects the states coming from the left lead to the right lead and vice versa.

$$S = \begin{pmatrix} r & \mathrm{t}' \\ t & \mathrm{r}' \end{pmatrix} \qquad (3.6)$$

Here r and t describe electrons coming of the left and t' and r' describe electrons coming from the right. Equation 3.6 suggests that $r, t, \acute{r}$ and t' are matrices for more than one channel, and could be complex (in the presence of a magnetic field for example). On the other hand charge conservation demands the S matrix be unitary: $SS^{+}=I$. The S matrix is a central object of scatteringtheory. It is useful not just in describing transport in the linear response regime, but also in other problems, such as adiabatic pumping.

3.3 Thermoelectric coefficients S

Seebeck, Peltier and Thompson developed the relationship between heat, current, temperature and voltage at the turn of the 19th century [16]. The Seebeck effect explains the production of electrical current as a result of a temperature difference, while the Thompson and Peltier effects explain the

cooling or heating of a current-carrying conductor. A deeper mechanism can be imagined where the difference temperature is $\Delta\mathcal{T}$ and a theoretical drop in value ΔV occurs in the system that causes heat and charge fluctuations. For heat ($\mathcal{Q}$) and charge (I) currents under the linear base and temperature schematic, the common Landauer-Büttiker formulas can be generalised to determine the thermoelectric coefficients of a device with two terminals. The system is composed of a scattering region that has connections to two leads, which are themselves connected to a pair of electron reservoirs. These reservoirs are constructed using the chemical potentials μ_L and μ_R, temperatures $\mathcal{T}_L$ and $\mathcal{T}_R$, and the Fermi distribution function [17]:

$$f_i\,(E) = \left(1 + e^{\frac{E-\mu_i}{k_B \mathcal{T}_i}}\right)^{-1} \tag{3.7}$$

It is possible to write the right moving charge current of an individual *k*-state emerging from the left reservoir on the basis of the number of electrons per unit length n, Fermi distribution f_L, group velocity v_g as well as the scattering region's transmission coefficient $T(E)$.

$$I_k^+ = nev_g(E(k))\,T\big(E(k)\big)\;f_L(E(k)) \tag{3.8}$$

The overall charge from right moving states may therefore be found by summing up all positive k states and then integrating them into an integral form;

where $n = 1/L$ for the electron density and $v_g = \frac{1}{\hbar}\frac{\partial E(k)}{\partial k}$.

$$I_k^+ = \sum_k e\,\frac{1}{L}\,\frac{1}{\hbar}\,\frac{\partial E(k)}{\partial k}\,T(E(k))\,f_L(E(k)) = \int_{-\infty}^{+\infty}\frac{2e}{h}\,T(E)\,f_L(E)\,dE \tag{3.9}$$

Consequently, for the left moving states, we obtain:

$$I_k^- = \int_{-\infty}^{+\infty} \frac{2e}{h}\, T(E)\, f_R(E)\, dE \tag{3.10}$$

As a result, the entire right-moving current can be written as:

$$I = I^+ - I^- = \frac{2e}{h} \int_{-\infty}^{+\infty} T(E)\, (f_L(E) - f_R(E))\, dE \tag{3.11}$$

Equation 3.11 represents the Landauer-Büttiker formula. An analogous derivation can be performed for the heat current (alternatively, energy current) of the identical system by beginning with the relation $\mathcal{Q} = Env_g$ instead of $I = nev_g$. The outcome is comparable to the previous result, but includes two additional terms:

$$\begin{pmatrix} I \\ \dot{Q} \end{pmatrix} = \begin{pmatrix} G & L \\ M & K \end{pmatrix} \begin{pmatrix} \Delta V \\ \Delta \mathcal{T} \end{pmatrix} \tag{3.12}$$

The thermoelectric coefficients L and M, in the absence of a magnetic field, are related by the Onsager relation:

$$M = -L\mathcal{T} \tag{3.13}$$

where $\mathcal{T}$ is temperature. By rearranging these equations, the current relations can be expressed in terms of the measurable thermoelectric coefficients, electrical resistance $R = 1/G$, thermopower $S = -\Delta V/\Delta \mathcal{T}$, Peltier coefficient Π, and the thermal constant k:

$$\begin{pmatrix} \Delta V \\ \dot{Q} \end{pmatrix} = \begin{pmatrix} \frac{1}{G} & -\frac{L}{G} \\ \frac{M}{G} & K - \frac{LM}{G} \end{pmatrix} \begin{pmatrix} 1 \\ \Delta \mathcal{T} \end{pmatrix} = \begin{pmatrix} R & S \\ \Pi & -K \end{pmatrix} \begin{pmatrix} 1 \\ \Delta \mathcal{T} \end{pmatrix} \tag{3.14}$$

The thermopower S is defined as the potential drop due to a temperature difference in the absence of an electrical current:

$$S = -\left(\frac{\Delta V}{\Delta \mathcal{T}}\right)_{I=0} = \frac{L}{G'} \tag{3.15}$$

The Peltier coefficient Π is defined as the heat transferred purely due to the charge current in the absence of a temperature difference:

$$\Pi = \left(\frac{\dot{Q}}{I}\right)_{\Delta \mathcal{T}=0} = \frac{M}{G} = -S\mathcal{T} \tag{3.16}$$

Lastly, the thermal conductance k is defined as the heat current caused by a temperature drop in the absence of an electric current:

$$k = -\left(\frac{\dot{Q}}{\Delta \mathcal{T}}\right)_{I=0} = -\left(1 + \frac{S^2 G \mathcal{T}}{k}\right) \tag{3.17}$$

Obviously, the evaluation of S or Π gives an idea of how well the device will act as a heat-driven current generator or a current driven cooling device.

The thermoelectric figure of merit, $Z\mathcal{T}$ [18, 19], can alternatively be defined in terms of these observable thermoelectric coefficients:

$$Z\mathcal{T} = \frac{S^2 G \mathcal{T}}{k} \tag{3.18}$$

In classical electronics, the $Z\mathcal{T}$ is calculated by computing the maximum induced temperature difference produced by an applied electrical current while Joule heating is present. Consider a current-carrying conductor sandwiched between two heat baths $\mathcal{T}_L$ and $\mathcal{T}_R$, as well as two electrical potentials V_L and V_R

The thermoelectric figure of merit is obtained by calculating the highest induced temperature differential in a conductor caused by an electrical current. By defining ($\dot{Q}$) as the gain in heat from bath L to R, then from equation 3.14 we obtain:

$$\dot{Q} = \Pi\, I - k\Delta\mathcal{T} \tag{3.19}$$

This heat transfer will cause the left bath to cool and the right bath to heat, with a result that $\Delta\mathcal{T}$ increases. The amount of Joule heating can be expressed as $\dot{Q}_J = RI^2$, which is proportional to the electrical resistance and the square of the current. This Joule heating will also affect the temperature difference induced by the heat transfer, and therefore in the steady state case:

$$\Pi\, I - k\Delta\mathcal{T} = \frac{R\, I^2}{2} \tag{3.20}$$

where, $R/2$ is the sum of two parallel resistances (internal and external resistance). After rearranging this, the temperature difference is

$$\Delta\mathcal{T} = \frac{1}{k}\left(\Pi\, I - \frac{R\, I^2}{2}\right) \tag{3.21}$$

This expression shows how the temperature difference depends on the current. To find the maximum temperature difference, the derivative of equation 3.21 with respect to the electric current is taken:

$$\frac{\partial \Delta\mathcal{T}}{\partial I} = \frac{\Pi - IR}{k} = 0 \tag{3.22}$$

Finally, by writing back $I = \Pi\,/R$ and substituting equation 3.16 into equation 3.22, for the maximum of the temperature different we obtain:

$$(\Delta\mathcal{T})_{max} = \frac{\Pi^2}{2kR} = \frac{S^2\mathcal{T}^2 G}{2k} \tag{3.23}$$

$$\frac{(\Delta\mathcal{T})_{max}}{\mathcal{T}} = \frac{S^2 G\mathcal{T}}{2k} = \frac{1}{2} Z\mathcal{T} \tag{3.24}$$

A dimensionless number that can be used to describe a molecular device's 'efficiency'

3.4 Scattering Theory in One Dimension

It is useful to calculate the scattering matrix for a simple one-dimensional system before presenting the extended methods. This will provide a detailed description of the approach used. Because Green's functions will be utilised in the derivation, I go over the form of the Green's function for a simple one-dimensional discretized lattice section 3.4.1 and then move on to calculating the scattering matrix of a one-dimensional scattered section 3.4.2.

3.4.1 Perfect One-Dimensional Lattice

In this section, I will discuss the form of the Green's function for a simple one dimensional lattice with on-site energies ε_o and real hopping parameters $-\gamma$ as shown in Figure 3.2.

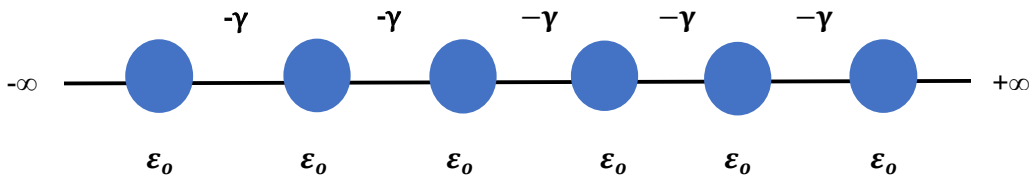

Figure 3.2. Tight-binding approximation of a one-dimensional periodic lattice with one site energies $\boldsymbol{\varepsilon_o}$ and coupling $\boldsymbol{\gamma}$.

The matrix form of the Hamiltonian can be simply written:

$$H = \begin{pmatrix} -\infty & . & . & . & . & . & . & . & . \\ . & . & . & . & . & . & . & . & . \\ . & . & \varepsilon_o & -\gamma & 0 & 0 & 0 & . & . \\ . & . & -\gamma & \varepsilon_o & -\gamma & 0 & 0 & . & . \\ . & . & 0 & -\gamma & \varepsilon_o & -\gamma & 0 & . & . \\ . & . & 0 & 0 & -\gamma & \varepsilon_o & -\gamma & . & . \\ . & . & 0 & 0 & 0 & -\gamma & \varepsilon_o & . & . \\ . & . & . & . & . & 0 & -\gamma & . & . \\ . & . & . & . & . & . & . & . & +\infty \end{pmatrix} \quad (3.25)$$

Within the tight-binding approximation, the Schrödinger equation (Equation 3.26) can be expanded at a lattice site z in terms of the energy and wavefunction ψ_z (Equation 3.27).

$$(E - H)\psi = 0 \quad (3.26)$$

$$\varepsilon_o\psi_z - \gamma\psi_z + 1 - \gamma\psi_z - 1 = E\psi_z \quad (3.27)$$

The wavefunction for this perfect lattice takes the form of a propagating Bloch state equation 3.28, normalized by its group velocity v in order for it to carry unit current flux. When this is substituted into equation 3.27, it leads to the well-known one-dimensional dispersion relation equation 3.29.

$$\psi_z = \frac{1}{\sqrt{v}} e^{ikZ} \quad (3.28)$$

$$E = \varepsilon_0 - 2\gamma \cos(\mathrm{k}) \quad (3.29)$$

Where we introduced the quantum number, k, commonly referred to as the wavenumber. The retarded Greens function $g(z, \acute{z})$ is closely related to the wavefunction and is in fact the solution to an equation very similar to that of the Schrödinger equation:

$$(E - H)\, g(z, z') = \delta_{(z,z')} \tag{3.30}$$

Physically, the retarded Greens function, $g(z, z')$, describes the response of a system at a point z due to a source at a point z'. Intuitively, we expect such an excitation to give rise to two waves, traveling outwards from the point of excitation, with amplitudes A^+ and A^- as shown in Figure 3.3

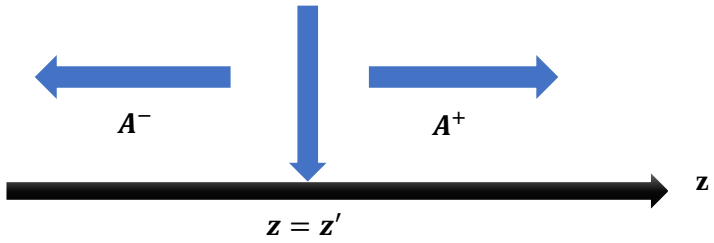

Figure 3.3. The structure of Retarded Green's Function of an infinite one-dimensional lattice. The excitation at z = z′causes wave to propagate left and right with amplitudes $\boldsymbol{A}^+$ and $\boldsymbol{A}^-$ respectively.

These waves can be expressed simply as:

$$g(z, z') = \begin{cases} A^+ e^{ikz}, & z \geq z' \\ A^- e^{-ikz}, & z \leq z' \end{cases} \tag{3.31}$$

This solution satisfies equation 3.30 at every point but $z = \acute{z}$. To overcome this, the Green's function must be continuous equation 3.32, so we equate the two at $z = \acute{z}$

$$A^{+}\, e^{ikz'} = A^{-}\, e^{-ik\acute{z}} \tag{3.32}$$

$$A^{+}\, e^{2ikz'} = A^{-} \tag{3.33}$$

Substituting equation 3.33 into the Green's functions equation 3.31 yields:

$$\begin{aligned} g(z,z') &= A^{+} e^{ikz'} e^{ik(z-z')} \quad z' > z \\ g(z,z') &= A^{+} e^{ikz'} e^{ik(z'-z)} \quad z' < z \end{aligned} \tag{3.34}$$

It is obvious that this can be stated as:

$$g(z,z') = A^{+} e^{ikz'} e^{ik\,|z-z'|} \tag{3.35}$$

Where:

$$A^{+} = \frac{e^{-iK\acute{z}}}{i\hbar v} \tag{3.36}$$

$$g(z,z') = \frac{e^{ik\,|z-z'|}}{i\hbar v} \tag{3.37}$$

It is possible to find a more extended derivation in the literature [6- 8].

$$v = \frac{dE(k)}{\hbar dk} = \frac{2\gamma sin(k)}{\hbar} \tag{3.38}$$

3.4.2 One-Dimensional Scattering

I study two single-axis, half-infinite leads that are linked by a coupling element $-\alpha$. Both leads have equal on-site potentials, ε_o, and hopping elements, $-\gamma$ (see Figure 3.4). The analytical solutions for the transmission and reflection coefficients can be calculated easily.

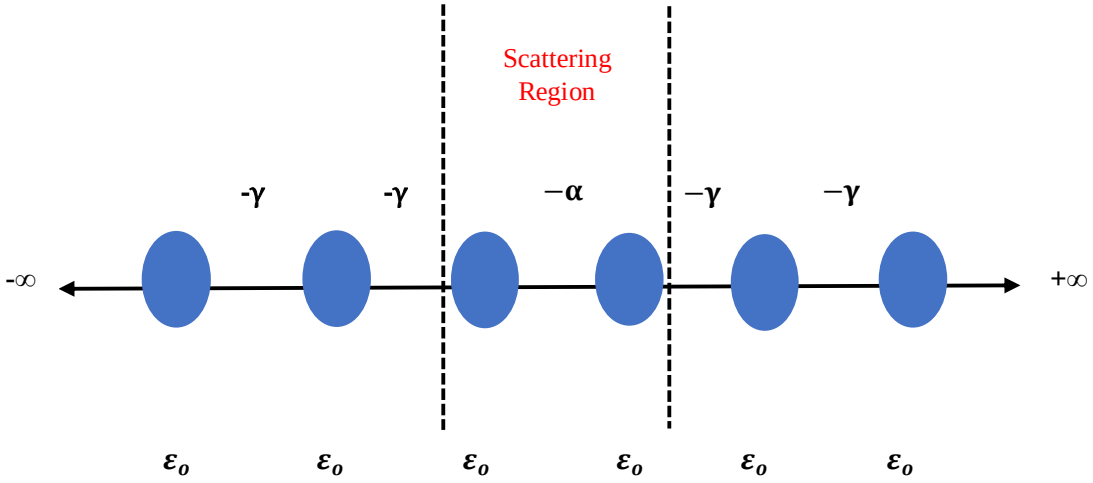

Figure 3.4. Simple tight-binding model of a one dimensional scattered attached to one dimensional leads.

We need to define a Hamiltonian, which takes the form of an infinite matrix.

$$H = \begin{pmatrix} \ddots & . & . & . & . & . & . & . & . \\ . & . & . & . & . & . & . & . & . \\ . & . & \varepsilon_o & -\gamma & 0 & 0 & 0 & . & . \\ . & . & -\gamma & \varepsilon_o & -\gamma & 0 & 0 & . & . \\ . & . & 0 & -\gamma & \varepsilon_o & -\alpha & 0 & . & . \\ . & . & 0 & 0 & -\alpha & \varepsilon_o & -\gamma & . & . \\ . & . & 0 & 0 & 0 & -\gamma & \varepsilon_o & . & . \\ . & . & . & . & . & 0 & -\gamma & . & . \\ . & . & . & . & . & . & . & . & \ddots \end{pmatrix} \tag{3.39}$$

For real γ, the dispersion relation corresponding to the leads introduced above was given in equation 3.29 and the group velocity was given in equation 3.38:

$$E(k) = \varepsilon_0 - 2\gamma \cos(\mathrm{k}) \tag{3.40}$$

$$v = \frac{1}{\hbar}\frac{dE}{dk} \tag{3.41}$$

In order to obtain the scattering amplitudes we need to calculate the Green's function of the system. The formal solution to equation 3.30 can be written as:

$$G = (E - H)^{-1} \tag{3.42}$$

Equation 3. 42 is singular if the energy E is equal to an eigenvalues of the Hamiltonian H. To circumvent this problem, it is practical to consider the limit:

$$G_{\pm} = \lim_{\eta \to 0}(E - H \pm i\eta)^{-1} \tag{3.43}$$

Here η is a positive number and G_+, G_- is the retarded (advanced) Green's function. In this thesis I will only use retarded Green's functions and hence choose the + sign. The retarded Green's function for an infinite, one dimensional chain with the same parameters is defined in equation 3.37:

$$g^{\infty}(j,l) = \frac{e^{ik|j-l|}}{i\hbar v} \tag{3.44}$$

Where j, l are the labels of the sites in the chain. In order to obtain the Green's function of a semi-infinite lead we need to introduce the appropriate boundary conditions. In this case, the lattice is semi-infinite, so the chain must terminate at a given point, i_0, so that all points for which $i \geq i_0$ are missing. This is achieved by adding a wave function to the Green's function to mathematically represent this condition. The wavefunction in this case is:

$$\psi_{j,l}^{i_0} = \frac{-e^{ik(2i_0 - l - j)}}{i\hbar v} \tag{3.45}$$

The Green's function $g(j,l) = g_{j,l}^{\infty} + \psi_{j,l}^{i_0}$ will have the following simple form at the Boundary $j = l = i_0 - 1$:

$$g\,(i_0 - 1, i_0 - 1) = -\frac{e^{ik}}{\gamma} \tag{3.46}$$

If we consider the case of decoupled leads, $\alpha = 0$, the total Green's function of the system will simply be given by the decoupled Green's function:

$$g = \begin{pmatrix} -\frac{e^{ik}}{\gamma} & 0 \\ 0 & -\frac{e^{ik}}{\gamma} \end{pmatrix} = \begin{pmatrix} g_L & 0 \\ 0 & g_R \end{pmatrix} \tag{3.47}$$

If we now switch on the interaction, then in order to obtain the Green's function of the coupled system G ,we need to use Dyson's equation,

$$G^{-1} = (g^{-1} - V) \tag{3.48}$$

Where the operator V describing the interaction connecting the two leads will have the form:

$$V = \begin{pmatrix} 0 & V_c \\ V_c^{\dagger} & 0 \end{pmatrix} = \begin{pmatrix} 0 & \alpha \\ \alpha^* & 0 \end{pmatrix} \tag{3.49}$$

Substituted equation 3.47 and 3.49 into 3.48 to get the solution to the Dyson's equation:

$$G = \frac{1}{|\alpha|^2 - \gamma^2 e^{-2ik}} \begin{pmatrix} \gamma e^{-ik} & \alpha \\ \alpha^* & \gamma e^{-ik} \end{pmatrix} \tag{3.50}$$

The only remaining step is to calculate the transmission, t , and reflection, r , amplitudes from the Green's function equation 3.50. This is done by making use of the FisherLee relation [4, 6] which relates the scattering amplitudes of a scattering problem to the Green's function of the problem. The Fisher-Lee relations in this case becomes:

$$r = i\hbar\, v_L G_{00} - 1 \tag{3.51}$$

$$t = i\hbar\sqrt{v_R v_L}\, G_{10} \tag{3.52}$$

These amplitudes correspond to particles incident from the left. If one would consider particles coming from the right than similar expressions could be recovered for the transmission, $\acute{t}$, and reflection, $\acute{r}$, amplitudes.

Since we are now in the possession of the full scattering matrix we can use the Landauer formula equation 3.4 to calculate the zero bias conductance.

3.5 Generalization of the Scattering Formalism

In this section, I show a generalized approach to transport calculations following the derivation of Lambert, presented in [2]. This is similar to the previous approach. First the surface Green's function of crystalline leads is computed, and the scattering amplitudes are recovered by means of a generalization of the Fisher-Lee relation.

3.5.1 Hamiltonian and Green's Function of the Leads

We investigate a fundamental semi-infinite crystalline electrode of arbitrary complexity. Because the leads are crystalline, the structure of the Hamiltonian is a generalization of the one-dimensional electrode Hamiltonian in equation 3.7. Figure 3.5 shows the general system topology. Instead of site energies, we have Hamiltonians for each repeating layer of the bulk electrode, H_0 , and a coupling matrix to describe the hopping parameters between these layers, H_1.

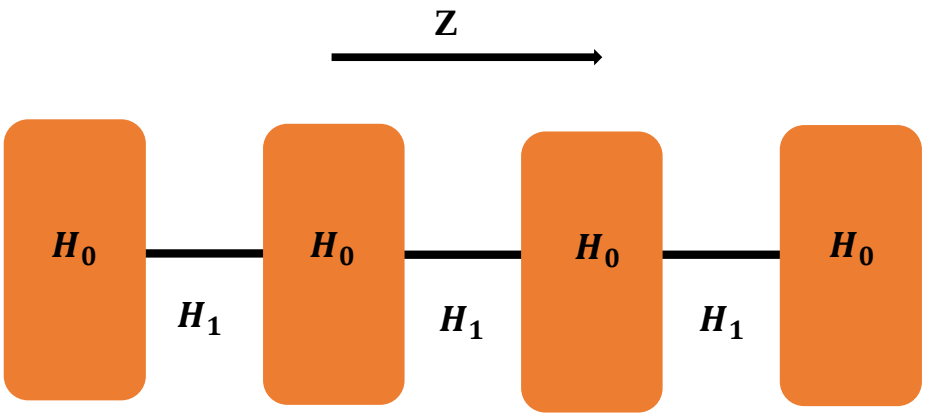

Figure 3.5. Schematic representation of a semi-infinite generalized lead. States described by the Hamiltonian H_0 are connected via a generalized hopping matrix H_1. The direction z is defined to be parallel to the axis of the chain. One can assign for each slice a label z.

The Hamiltonian for such a system has the form:

$$H = \begin{pmatrix} \bullet & \bullet & 0 & 0 & 0 & 0 & 0 & 0 \\ \bullet & \bullet & H_1 & 0 & 0 & 0 & 0 & 0 \\ 0 & H_1^{\dagger} & H_o & H_1 & 0 & 0 & 0 & 0 \\ 0 & 0 & H_1^{\dagger} & H_o & H_1 & 0 & 0 & 0 \\ 0 & 0 & 0 & H_1^{\dagger} & H_o & H_1 & 0 & 0 \\ 0 & 0 & 0 & 0 & H_1^{\dagger} & H_o & H_1 & 0 \\ 0 & 0 & 0 & 0 & 0 & H_1^{\dagger} & \bullet & \bullet \\ 0 & 0 & 0 & 0 & 0 & 0 & \bullet & \bullet \end{pmatrix} \tag{3.53}$$

Where H_o and H_1 are generally complex matrices and the only limitation is that the full Hamiltonian, H , must be Hermitian. In this section, the initial objective is for the Green's function of this type of lead to be calculated for general H_1 and H_0. to calculate the Green's function one has to calculate the spectrum of the Hamiltonian by solving the Schrödinger equation of the lead.

$$H_1^{\dagger}\psi_{z-1} + H_o\psi_z + H_1\psi_{z+1} = E\psi_z \tag{3.55}$$

Here, ψ_z is the wave function describing layer z, where z is an integer measured in units of inter-layer distance. We assume the system is infinitely periodic in the z direction only, so the on-site wavefunction, ψ_z, can be represented in Bloch form; consisting of a product of a propagating plane wave and a wavefunction, Φ_k , which is perpendicular to the transport direction, z. layer Hamiltonian, H_0, has dimensions $M \times M$ (or in other words consists of M site energies and their respective hopping elements), then the perpendicular wavefunction, Φ_k , will have M degrees of freedom and take the form of a $1 \times M$ dimensional vector. So the wave function, ψ_z, takes the form:

$$\psi_z = \sqrt{n_k}e^{ikz}\Phi_k \tag{3.56}$$

Where, n_k is an arbitrary normalization parameter. Substituting this into the Schrödinger equation (Equation 3.55) , these yields:

$$\left(H_0 + e^{ik}H_1 + e^{-ik}H_1^{\dagger} - E\right)\Phi_k = 0 \tag{3.57}$$

To dertmine the band structure for such a problem, one would select values of k and calculate the eigenvalues at that point, $E = E_l(k)$, where $= 1,2,3, \ldots, M$. Here, l denotes the band index. For every k value, the eigenvalue problem will have M solutions, and thus, M energy values. By selecting multiple values for k, it is relatively simple to build up a band structure. In a scattering problem, the problem is tackled using the different approach. Instead of finding the eigenvalues at a given k, we find the values

of k at a given E. In order to accomplish this, a root-finding might have been used, but this would have required an enormous numerical effort since the wave numbers are in general complex. However, we can write down an alternative eigenvalue problem in which energy is the result and wave numbers are the result by introducing the function:

$$v_k = e^{-ikz}\Phi_k \tag{3.58}$$

which is then combined with equation 3.57:

$$\begin{pmatrix} -H_1^{-1}(H_o - E) & -H_1^{-1}H_1^{\dagger} \\ I & 0 \end{pmatrix}\begin{pmatrix} \Phi_k \\ v_k \end{pmatrix} = e^{ikz}\begin{pmatrix} \Phi_k \\ v_k \end{pmatrix} \tag{3.59}$$

Given a layer Hamiltonian, H_o, that has dimensions of M×M, equation 3.59 will produce $2M$ eigenvalues, $e^{ik_l z}$ and eigenvectors, Φ_k , with magnitude M. These states can then be sorted into four categories based on whether they are propagating or decaying and whether they are left going or right going. A state is considered to be propagating when it has a real k_l value. Where the wave number has a positive imaginary part, it is defined as a left decaying state, whereas if the imaginary part is negative, it is defined as a right decaying state. The sorting of propagating states is based on the state's group velocity, which is given by:

$$v_{kl} = \frac{1}{\hbar}\frac{\partial E_{k,l}}{\partial k} \tag{3.60}$$

If the group velocity, v_{kl} , of the state is positive than it is a right propagating state if it is negative than it is a left propagating state.

Table 3.1: Sorting the eigenstates into left and right propagating or decaying states according to the wave number and group velocity.

Category	Left	Right
Decaying	$Im(k_l) > 0$	$Im(k_l) < 0$
Propagation	$Im(k_l) = 0, v_g^{k_l} < 0$	$Im(k_l) = 0, v_g^{k_l} > 0$

Now, I will denote the k_l wave numbers which belong to the left propagating-decaying set of wave numbers by k_l and the right propagating decaying wave numbers will remain plainly k_r. Hence, ϕ_{kr} is a wave function associated to a right state and ϕ_{kl} is associated to a left state. If H_1 is invertible, there must be exactly the same number, M, of left and right going states. It is clear that if H_1 is singular, the matrix in equation 3.59 cannot be constructed, since it relies of the inversion of H_1. Furthermore, any one of several methods can be used to overcome this problem. The first [2, 8, 10] uses the decimation technique to create an effective, non-singular H_1. Another possibility is to populate a solitary H_1 with small random numbers, introducing an explicit numerical mistake. The introduced numerical error could be as little as the numerical error introduced by decimation, making this approach reasonable. Another solution is to rewrite equation 3.59 without inverting H_1:

$$\begin{pmatrix} -(H_o - E) & -H_1^{\dagger} \\ I & 0 \end{pmatrix} \begin{pmatrix} \Phi_k \\ v_k \end{pmatrix} = e^{ikz} \begin{pmatrix} H_1 & 0 \\ 0 & I \end{pmatrix} \begin{pmatrix} \Phi_k \\ v_k \end{pmatrix} \tag{3.61}$$

However, solving this generalized Eigen-problem is more computationally expensive. Any of the aforementioned methods work reasonably in tackling the problem of a singular H_1 matrix, and so can the condition that there must be exactly the same number, M, of left and right going states, whether H_1 is singular or not [11-15].

The solutions to the eigenvalue equation 3.57 at a given wave number, k,will form an orthogonal basis set, however, the eigenstates, Φ_{k_l} ,obtained by solving the Eigen problem equation 3.61 at a given energy, E,will not generally form an orthogonal set of states. This is very significant, as we will have to calculate the Green's function non-orthogonally when constructing the Green's function. It is, therefore, necessary to introduce the duals to, Φ_{k_l}, and, $\Phi_{\bar{k}_l}$, in such a way that they obey:

$$\widetilde{\Phi}^{\dagger}_{(k_i)}\Phi_{k_j} = \widetilde{\Phi}^{\dagger}_{(\bar{k}_i)}\Phi_{\bar{k}_j} = \delta_{ij} \tag{3.62}$$

This yields the generalized completeness relation:

$$\sum_{l=1}^{M} \widetilde{\Phi}^{\dagger}_{(k_l)}\Phi_{(k_l)} = \sum_{l=1}^{M} \widetilde{\Phi}^{\dagger}_{(\bar{k}_l)}\Phi_{(\bar{k}_l)} = I \tag{3.63}$$

We are in possession of the whole set of eigenstates at a given energy we can calculate the Green's function first for the infinite system and then, if suitable boundary conditions are satisfied, for the semi-infinite leads at their surface. Since the Green's function satisfies the Schrödinger equation when $z = z'$, we can build up the Green's function from the mixture of the eigenstates Φ_{k_l} and $\Phi_{\bar{k}_l}$:

$$g(z,z') = \begin{cases} \sum_{l=1}^{M} \Phi_{(k_l)} e^{ik_l(z-z')}\, \omega^{\dagger}_{k_l}, & z \geq z' \\ \sum_{l=1}^{M} \Phi_{(\bar{k}_l)} e^{i\bar{k}_l(z-z')}\, \omega^{\dagger}_{\bar{k}_l}, & z \leq z' \end{cases} \tag{3.64}$$

Where the M-component vectors ω_{k_l} and $\omega_{\bar{k}_l}$ are to be determined. It is important to note the structural similarities between this equation and equation 3.31 and also that all the degrees of freedom in the transverse direction are contained in the vectors Φ_k and ω_k.

The big picture now is to obtain the vectors. As stated in section 3.4.1, equation 3.64 must be continuous at $z = z'$ and must satisfy Green's function equation (equation 3.30). The first condition is written as:

$$\sum_{l=1}^{M} \Phi_{(k_l)} \omega_{k_l}^{\dagger} = \sum_{l=1} \Phi_{(\bar{k}_l)} \omega_{\bar{k}_l}^{\dagger} \tag{3.65}$$

and the second:

$$\sum_{l=1}^{M} \left[(E - H_o) \Phi_{(k_l)} \omega_{k_l}^{\dagger} + H_1 e^{ik_l} \omega_{k_l}^{\dagger} + H_1^{\dagger} \Phi_{(\bar{k}_l)} e^{-i\bar{k}_l} \omega_{\bar{k}_l}^{\dagger} \right] = I$$

$$\sum_{l=1}^{M} \left[(E - H_o) \Phi_{(k_l)} \omega_{k_l}^{\dagger} + H_1 \Phi_{(k_l)} e^{ik_l} \omega_{k_l}^{\dagger} + H_1^{\dagger} \Phi_{(\bar{k}_l)} e^{-i\bar{k}_l} \omega_{\bar{k}_l}^{\dagger} + H_1^{\dagger} e^{-ik_l} \omega_{k_l}^{\dagger} - H_1^{\dagger} e^{-ik_l} \omega_{k_l}^{\dagger} \right] = I$$

$$\sum_{l=1}^{N} \left[H_1^{\dagger} \Phi_{(\bar{k}_l)} e^{i\bar{k}_l} \omega_{\bar{k}_l}^{\dagger} - H_1^{\dagger} \Phi_{(k_l)} e^{-ik_l} \omega_{k_l}^{\dagger} \right] + \sum_{l=1}^{M} \left[(E - H_o) + H_1 e^{ik_l} + H_1^{\dagger} e^{-ik_l} \right] \Phi_{(k_l)} \omega_{k_l}^{\dagger} = I$$

We also know that from the Schrödinger equation.

$$\sum_{l=1}^{M} \left[(E - H_o) + H_1 e^{ik_l} + H_1^{\dagger} e^{-ik_l} \right] \Phi_{(k_l)} = 0 \tag{3.66}$$

This yields to:

$$\sum_{l=1}^{N} H_1^{\dagger} \left[\Phi_{(\bar{k}_l)} e^{i\bar{k}_l} \omega_{\bar{k}_l}^{\dagger} + \Phi_{(k_l)} e^{-ik_l} \omega_{k_l}^{\dagger} \right] = I \tag{3.67}$$

Next, the dual vectors defined in equation 3.62 are used. The multiplication of equation 3.65 by $\widetilde{\Phi}_{(k_p)}$ yields:

$$\sum_{l=1}^{M} \widetilde{\Phi}^{\dagger}_{(k_p)} \Phi_{(\bar{k}_l)} \omega^{\dagger}_{\bar{k}_l} = \omega^{\dagger}_{k_p} \tag{3.68}$$

and similarly multiplying by $\widetilde{\Phi}^{\dagger}_{(\bar{k}_p)}$ gives:

$$\sum_{l=1}^{M} \widetilde{\Phi}^{\dagger}_{(\bar{k}_p)} \Phi_{(k_l)} \omega^{\dagger}_{k_l} = \omega^{\dagger}_{\bar{k}_p} \tag{3.69}$$

Using the continuity equation 3.65 and equations 3.68 and 3.69, the Green's function equation (equation 3.67) becomes:

$$\sum_{l=1}^{M} \sum_{p=1}^{M} H_1^{\dagger} \left(\Phi_{(\bar{k}_l)} e^{-i\bar{k}_l} \widetilde{\Phi}^{\dagger}_{(\bar{k}_l)} - \Phi_{(k_l)} e^{-ik_l} \widetilde{\Phi}^{\dagger}_{(k_l)} \right) \Phi_{(\bar{k}_p)} \omega^{\dagger}_{\bar{k}_p} = I \tag{3.70}$$

Hence, it follows that:

$$\begin{aligned} &\sum_{l=1}^{M} \left[H_1^{\dagger} \left(\Phi_{(\bar{k}_l)} e^{-i\bar{k}_l} \widetilde{\Phi}^{\dagger}_{(\bar{k}_l)} - \Phi_{(k_l)} e^{-ik_l} \widetilde{\Phi}^{\dagger}_{(k_l)} \right) \right]^{-1} \\ &= \sum_{p=1}^{M} \Phi_{(\bar{k}_p)} \omega^{\dagger}_{\bar{k}_p} = \sum_{p=1}^{M} \Phi_{(k_p)} \omega^{\dagger}_{k_p} \end{aligned} \tag{3.71}$$

This immediately gives us an expression for $\omega_k^{\dagger}$:

$$\omega_k^{\dagger} = \widetilde{\Phi}^{\dagger}_{(k)} \nu^{-1} \tag{3.72}$$

where ν is defined as:

$$\nu = \sum_{l=1}^{M} H_1^{\dagger} \left(\Phi_{(\bar{k}_l)} e^{-i\bar{k}_l} \widetilde{\Phi}^{\dagger}_{(\bar{k}_l)} - \Phi_{(k_l)} e^{-ik_l} \widetilde{\Phi}^{\dagger}_{(k_l)} \right) \tag{3.73}$$

In equation 3.72, the wave number (k) denotes both left and moving states. The substitution of equation 3.72 into equation 3.64 produces the Green's function of an infinite system:

$$g_{z,z'}^{\infty} = \begin{cases} \sum_{l=1}^{M} \Phi_{(k_l)} e^{ik_l(z-z')} \widetilde{\Phi}_{(k_l)}^{\dagger} v^{-1}, & z \geq z' \\ \sum_{l=1}^{M} \Phi_{(\bar{k}_l)} e^{i\bar{k}_l(z-z')} \widetilde{\Phi}_{(\bar{k}_l)}^{\dagger} v^{-1}, & z \leq z' \end{cases} \tag{3.74}$$

To obtain the Green's function for a semi-infinite lead, a wave function must be added to the Green's function so that the boundary conditions at the lead's edge can be satisfied, similar to the one-dimensional example. In this case, the boundary condition stipulates that the Green's function must disappear at a particular place ($z = z_o$). For this to be achieved,

$$\triangle = -\sum_{l,p=1}^{M} \Phi_{\bar{k}_l} e^{i\bar{k}_l(z-z_o)} \widetilde{\Phi}_{(\bar{k}_l)}^{\dagger} \Phi_{(k_p)} e^{ik_p(z_o-z)} \widetilde{\Phi}_{(k_p)}^{\dagger} v^{-1} \tag{3.75}$$

To the Green's function, equation 3.74, $g = g^{\infty} + \triangle$. This yields the surface Green's function fora semi-infinite lead going left:

$$g_L = \left(I - \sum_{l,p=1}^{M} \Phi_{(\bar{k}_l)} e^{-i\bar{k}_l} \widetilde{\Phi}_{(\bar{k}_l)}^{\dagger} \Phi_{(k_p)} e^{ik_p} \widetilde{\Phi}_{(k_p)}^{\dagger} \right) v^{-1} \tag{3.76}$$

and going right:

$$g_R = \left(I - \sum_{l,p=1}^{M} \Phi_{(k_l)} e^{ik_l} \widetilde{\Phi}_{(k_l)}^{\dagger} \Phi_{(\bar{k}_p)} e^{-i\bar{k}_p} \widetilde{\Phi}_{(\bar{k}_p)}^{\dagger} \right) v^{-1} \tag{3.77}$$

All that remains is to obtain the Hamiltonian of the scattering region using DFT and combine this with the surface Green's functions via Dyson's equation, to obtain the total Green's function and transmission amplitude t_{kl} [16].

$$G_{total} = \left[\begin{pmatrix} g_L & 0 \\ 0 & g_R \end{pmatrix} - H_{scattering}\right] \tag{3.78}$$

$$t_{kl} = \tilde{\Phi}^{\dagger}_{(k_l)} G_{total} v \Phi_{(k_l)} \sqrt{\frac{v_k}{v_l}}\, e^{ik_l} \tag{3.79}$$

3.6 Conclusion

In this chapter, I have discussed the Landauer formula for the electrical conductance G and thermoelectric coefficients, such as the Seebeck coefficient S. This chapter also shows how to calculate the scattering matrix of a system linked to one-dimensional leads using the Green's function approach to scattering Theory. This was generalised to transport calculations in higher dimensions, which form a basis of the GOLLUM transport code and will be used in the following chapters.

Bibliography

1. Landauer,R.(1957). Spatial variation of currents and fields due to localized scatterers in metallic conduction. IBM *Journal of research and development*, 1(3), 223-231.
2. Sanvito, S. (1999). Giant Magnetoresistance and Quantum Transport in Magnetic Hybrid Nanostructures. (Doctoral dissertation, Lancaster University).
3. Büttiker,M., Imry, Y., Landauer, R., and Pinhas, S. (1985). Generalized many-channel conductance formula with application to small rings. *Physical Review B*, 31(10), 6207.
4. Fisher, D. S., and Lee, P. A. (1981). Relation between conductivity and transmission matrix. *Physical Review B*, 23(12), 685.
5. Finch, C. M., Sirichantaropass, S., Bailey, S. W., Grace, I. M., Garcia-Suarez, V. M., and Lambert, C. J. (2007). Conformation dependence of molecular conductance: chemistry versus geometry. *Journal of Physics: Condensed Matter*, *20*(2), 022203.
6. Datta, S. (1997). Electronic transport in mesoscopic systems. Cambridge university press.
7. Economou, E. N. (1983). Two or More Impurities; Disordered Systems. In Green's Functions in Quantum Physics (pp. 128-195). *Springer*, Berlin, Heidelberg.
8. Mello, P. A., Mello, P. A., Kumar, N., and Narendra Kumar, D. (2004). Quantum transport in mesoscopic systems: complexity and statistical fluctuations: a maximum-entropy viewpoint (Vol. 4). Oxford University Press on Demand.
9. Milan, D. C., Krempe, M., Ismael, A. K., Movsisyan, L. D., Franz, M., Grace, I., Brooke, R., schwarzacher, W., Higgins, S., Anderson, H., Lambert, C. J., Tykwinski, R., and Nichols, R. J. (2017). The single-molecule electrical conductance of a rotaxane-hexayne supramolecular assembly. *Nanoscale*, *9*(1), 355-361.

10. MacKinnon, J. G., and White, H. (1985). Some heteroskedasticity-consistent covariance matrix estimators with improved finite sample properties. *Journal of econometrics*, 29(3), 305-325).
11. Davidson, R. J., Milan, D. C., Al-Owaedi, O. A., Ismael, A. K., Nichols, R. J., Higgins, S. J., Lambert, C. J., Yufit, D., and Beeby, A. (2018). Conductance of 'bare-bones' tripodal molecular wires. *RSC advances*, *8*(42), 23585-23590.
12. Koltai, J., Cserti, J., and Lambert, C. J. (2004). Andreev bound states for a superconducting-ferromagnetic box. *Physical review B*, 69(9), 092506.
13. Athanasopoulos, S. (2005). Electronic properties of hybrid carbon nanotubes (Doctoral dissertation, Lancaster University).
14. Ismael, A. K., Grace, I., & Lambert, C. J. (2017). Connectivity dependence of Fano resonances in single molecules. *Physical Chemistry Chemical Physics*, *19*(9), 6416-6421.
15. Polinák, P. K., Lambert, C. J., Koltai, J., and Cserti, J. (2006). Andreev drag effect via magnetic quasiparticle focusing in normal-superconductor nanojunctions. *Physical Review B*, 74(13), 132508.
16. Lambert, C. J. (2021). Quantum Transport in Nanostructures and Molecules. *IoP publishing.*
17. Finch, C. M. (2008). *An understanding of the the electrical characteristics of organic molecular devices* (Doctoral dissertation, Lancaster University).
18. Athanasopoulos, S. (2005). *Electronic properties of hybrid carbon nanotubes* (Doctoral dissertation, Lancaster University).
19. Goldsmid, H. (2013). *Thermoelectric refrigeration*. *Springe.*

Chapter 4

Electronic structure investigation of endohedral metallofullerenes (EMFs)

This work was a joint collaboration between the group of Prof. Nicolas Agrait (Departamento de Física de la Materia Condensada, Universidad Autónoma de Madrid, Spain), who conducted the experiments and the group of Prof. Kyriakos Porfyrakis (Department of Materials, University of Oxford), who synthesised the molecules. This work has been submitted as part of the following paper:

"*Exploiting fluctuations in the search for high-thermoelectric performance molecular junctions*"

Laura Rincón-García, Charalambos Evangeli, Panagiotis Dallas, *Turki Alotaibi*, Alaa A. Al-Jobory, Gabino Rubio-Bollinger, Kyriakos Porfyrakis, Nicolas Agrait and Colin J. Lambert.

In this chapter, the electronic structure of three endohedral metallofullerenes (EMFs), including $Sc_3N@C_{80}$, $Sc_3C_2@C_{80}$, and $Er_3N@C_{80}$, in addition to an empty cage such as C_{60} are intensively explored. I start these investigations with wave function plots of the studied molecules. Three different methods including Mulliken, Hirshfeld [11] and Voronoi population analyses [12], were employed to track down the charge transfer between metallic moieties and the cage. The charge transfer analyses were carried out in the gas phase and on a gold substrate. To determine the most probable orientation for metallic moieties such as Sc_3N, Er_3N and Sc_3C_2 inside the cage, the counterpoise method was employed for their different rotation angles θ, Φ and β (defined below) in the gas phase. A similar approch was used on a Au-substrate in which case, rotations about four different rotation axes θ, Φ, α and β are explored.

I also investigate how θ, Φ, α and β axes pass through the metallic moieties and how the total energy varies with the angle of rotation, both in the presence and absence of a gold substrate. There are an infinite number of inequivalent orientations of the metallic moieties relative to their fullerene cage. However, for each of the four axes, I consider one mode of rotation in the gas phase and three modes of rotation on a substrate.

4.1 Introduction

Since the discovery of fullerenes in 1985 [1] significant attention has been devoted to study the solid-state properties of fullerenes and their derivatives, because they are a well-known class of n-type semiconductors, that are promising candidates for practical application in molecular electronics such as organic thin-film transistors and organic photovoltaic devices [2]. The encapsulation of one or more atoms into fullerenes leads to the formation of endohedral metallofullerenes (EMFs). Because of the influence of interaction between endohedral metal atoms and the fullerene cage, the electronic properties of EMFs are changed drastically from those of empty fullerenes [3]. Fullerene derivatives, like endohedral fullerenes, are now widely used in organic photovoltaics [4], catalysis [5], and biological and medicinal applications [6]. Fullerenes with over 60 carbon atoms are called higher fullerenes. In this thesis, I shall study the C_{80} fullerene cage which can encapsulate metallic moieties to form EMFs as shown in Figure 4.1.

4.2 Studied Molecules

Figure 4.1 shows four molecules, $Sc_3C_2@C_{80}$ which has three scandium and 82 carbon atoms (a), $Sc_3N@C_{80}$ which has three scandium, one nitrogen and eighty carbon atoms (b), $Er_3N@C_{80}$ which has three erbium and eighty carbon atoms (c), C_{60} with sixty carbon atoms (d). The metallic moieties are called scandium carbide, scandium nitride and erbium nitride Sc_3C_2, Sc_3N and Er_3N respectively. The C_{60} is empty cage as shown in Figure 4.1d.

Using the DFT code SIESTA, the optimum geometries of the isolated molecules were obtained by relaxing the molecules until all forces on the atoms were less than 0.05 eV/Å. A double-zeta plus

polarization orbital basis set, norm-conserving pseudopotentials were utilised, an energy cut-off of 200 Rydbergs defined the real space grid and the local density approximation (LDA) was chosen to be the exchange correlation functional. I also computed results using GGA and found that the resulting transmission functions were comparable with those obtained using LDA [8-10].

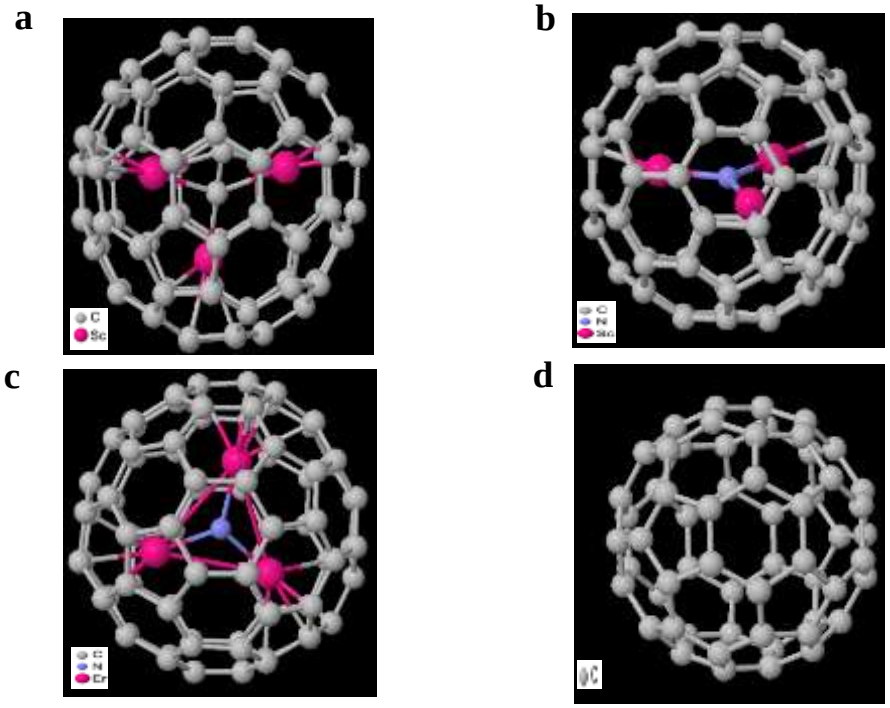

Figure 4.1. Endohedral metallofullerenes and fullerene studied Molecules. Schematic of the three endohedral metallofullerenes (EMFs), namely, **a:** $Sc_3C_2@C_{80}$, **b:** $Sc_3N@C_{80}$, and **c:** $Er_3N@C_{80}$ and an empty cage **d:** C_{60}.

4.3 Frontier orbitals of the EMFs molecules and the C_{60}

To obtain a better understanding of the electronic properties of these structures (see Figure 4.1), the methods introduced in chapter 2 have been employed. Thus, I will investigate the wave function plots of the EMFs molecules and C_{60}. The highest occupied molecular orbitals (**HOMO**), lowest unoccupied orbitals (**LUMO**), **HOMO+1** and **LUMO+1** along with their energies are calculated. The blue and red colours correspond to the regions in space of positive and negative orbital amplitude.

4.3.1 Frontier orbitals of $Sc_3C_2@C_{80}$ EMF

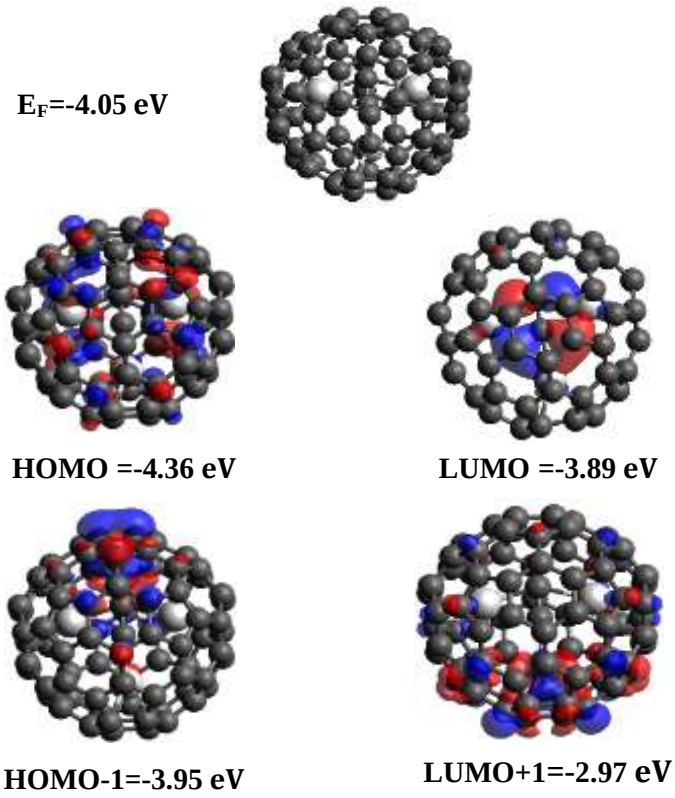

Figure 4.2. Wave function plots of $Sc_3C_2@C_{80}$. **Top panel**: fully optimised geometry of $Sc_3C_2@C_{80}$ EMF. **Lower panel**: HOMO, LUMO, HOMO-1, LUMO+1 of Sc_3 $C_2@C_{80}$ molecule along with their energies.

4.3.2 Frontier orbitals of $Sc_3N@C_{80}$ EMF

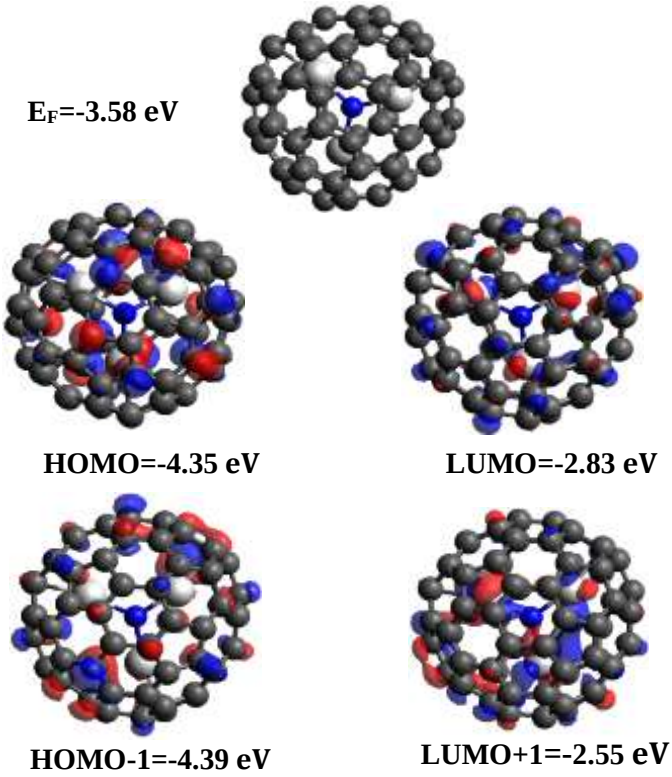

Figure 4.3. Wave function plots of $Sc_3N@C_{80}$. **Top panel**: fully optimised geometry of $Sc_3N@C_{80}$ EMF. **Lower panel**: HOMO, LUMO, HOMO-1, LUMO+1 of $Sc_3N@C_{80}$ molecule along with their energies.

4.3.2 Frontier orbitals of $Er_3N@C_{80}$ EMF

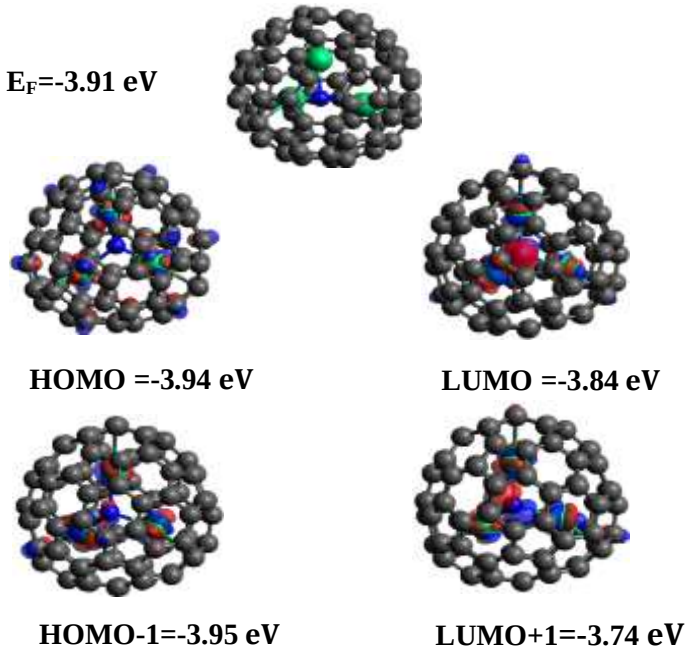

Figure 4.4. Wave function plots of $Er_3N@C_{80}$. **Top panel**: fully optimised geometry of $Er_3N@C_{80}$ EMF. **Lower panel**: HOMO, LUMO, HOMO-1, LUMO+1 of Er_3 $N@C_{80}$ molecule along with their energies.

4.3.4 Frontier orbitals of C_{60} cage

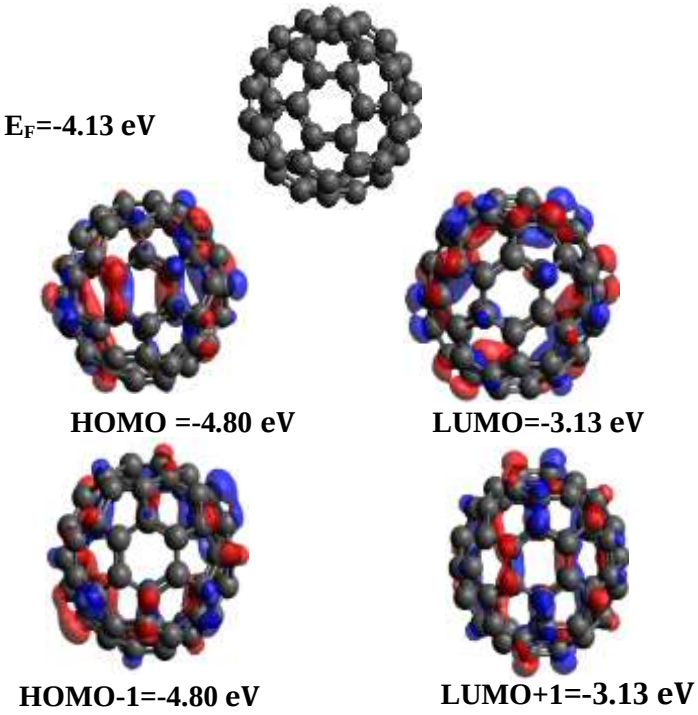

Figure 4.5. Wave function plots of C_{60}. **Top panel**: fully optimised geometry C_{60} EMF. **Lower panel**: HOMO, LUMO, HOMO-1, LUMO+1 of C_{60} molecule along with their energies.

It is worth mentioning that for C_{60}, the HOMO is five-fold degenerate, with states denoted HOMO, HOMO-1, HOMO-2, HOMO-3 and HOMO-4. The energy of the HOMO degenerate state is -4.8 eV. In the LUMO level, there are three-fold degenerate states LUMO, LUMO+1 and LUMO+2 with an energy of -3.13 eV. My DFT predictions for these degenerate states are well supported by a published work [17]. I did not see any degeneracy for EMFs.

The Frontier orbitals for EMFs did not depend on the orientation of the inner moiety inside the cage.

4.4 Charge transfer analyses

Net atomic charge is a common idea in all chemical sciences. It is difficult to imagine learning chemistry without discussing net atomic charges [14]. For example, experiments measuring the water molecule's dipole moment imply a negative net atomic charge on its oxygen atom and a positive net atomic charge on each of its two hydrogen atoms [15]. Net atomic charge also plays an important role in solid state physics, where oxygen atoms in solid oxides carry negative net atomic charges to enable oxygen ion transport [16]. There are many methods to calculate the charge transfer in Density Functional Theory. In this chapter, I am going to focus on three methods, that are implemented in SIESTA code, including Mulliken populations, Hershfield and Voronoi charge analyses.

I will investigate the electrical properties of the 3 EMFs molecules first in the gas phase, then I will repeat the same calculations, but on an Au substrate. Electrons are expected to be transferred from the donor moiety (the metallic moetiy) to the acceptor (the cage). The three methods Mulliken, Hirshfeld and Voronoi) will be used to determine the charge transfer from the donor to the acceptor.

4.4.1. Charge transfer analyses of $Sc_3C_2@C_{80}$ EMF in gas phase

Table 4.1 shows the charge transfer from the metallic moiety Sc_3C_2 to the I_h-C_{80} cage. Table 4.1 illustrates that the metallic moiety Sc_3C_2 loses (+) in total 1.4 electrons. 1.146 is the net charge that has been gained (-) by the I_h-C_{80} cage, the difference of 0.254 electrons remains in the space between the metallic moiety Sc_3C_2 and I_h-C_{80} cage, as estimated by the Mulliken method. Hirshfeld and Voronoi charges follow a similar trend; the net charges are 1.146 and 1.067 electrons respectively.

It is worth mentioning that, the charge transferred from the metallic moetiy to the cage and the charge effected on the electrical conductance G and Seebeck coefficients S.

Table 4.1: Charge transfer analyses using Mulliken, Hirshfeld and Voronoi methods of $Sc_3C_2@C_{80}$ EMF, in gas phase.

Metallic Moiety	Mulliken charge		Hirshfeld charge		Voronoi charge	
	Moiety	Ih-C_{80} cage	Moiety	Ih-C_{80} cage	Moiety	Ih-C_{80} cage
Sc_3C_2	+1.400	-1.146	+1.146	-0.730	+1.067	-0.618

4.4.2 Charge transfer analyses of $Sc_3N@C_{80}$ EMF in gas phase

Table 4.2 shows the amount of charge transfer from the metallic moiety Sc_3N to the Ih-C_{80} cage. Table 4.2 illustrates that the metallic moiety Sc_3N loses (+)1.50 electrons. 1.36 is the net charge gained (-) by the I_h-C_{80} cage; the difference of 0.153 electrons resides in the space between the metallic moiety Sc_3C_2 and I_h-$C_{80,}$ as estimated by the Mulliken method. The Hirshfeld and Voronoi methods follow a similar trend; the net charges are 1.36 and 1.27 electron respectively.

It is worth mentioning that, the charge transferred from the metallic moetiy to the cage and the charge effected on the electrical conductance G and Seebeck coefficients S.

Table 4.2: Charge transfer analyses using Mulliken, Hirshfeld and Voronoi methods of $Sc_3N@C_{80}$ EMF, in gas phase.

Metallic Moiety	Mulliken charge		Hirshfeld charge		Voronoi charge	
	Moiety	Ih-C_{80} cage	Moiety	Ih-C_{80} cage	Moiety	Ih-C_{80} cage
Sc_3N	+1.504	-1.369	+1.369	-0.938	+1.272	-0.792

4.4.3 Charge transfer analyses of $Er_3N@C_{80}$ EMF in gas phase

Table 4.3 shows the amount of charge transfers from the metallic moiety Er_3N to I_h-C_{80} cage. Table 4.3 shows that the metallic moiety Er_3N loses (+)1.962 electrons. 0.447 is the net charge gained (-) by the I_h-C_{80} cage. The difference of 1.515 electrons is located in the space between the metallic moiety Er_3C_2 and I_h-C_{80} . 1.962 is the net Mulliken charge that has been gained by the I_h-C_{80} cage. Hirshfeld and Voronoi charges follow a net charge of 7.484 and 7.145 electrons respectively.

It is worth mentioning that, the charge transferred from the metallic moetiy to the cage and the DFT results for $Er_3N@C_{80}$ EMF are unreliable due to the fact that this EMF possesses *f*-electrons. Due to this reason I can not calculate the electrical conductance G and Seebeck coefficients S in my thesis.

Table 4.3: Charge transfer analyses using Mulliken, Hirshfeld and Voronoi methods of $Er_3N@C_{80}$ EMF, in gas phase.

Metallic Moiety	Mulliken charge		Hirshfeld charge		Voronoi charge	
	Moiety	Ih-C_{80} cage	Moiety	Ih-C_{80} cage	Moiety	Ih-C_{80} cage
Er_3N	+1.962	-0.447	+7.484	-6.145	+7.145	-5.823

4.5 Axes and rotation modes of EMFs

There are an infinite number of inequivalent orientations of the metallic moiety relative to the fullerene cage. In what follows, I consider a selection of rotations about high-symmetry axes. In the gas phase, I consider rotation of the metallic moiety relative to a fixed fullerene cage. For this rotational mode, rotations about the β and Φ axes are equivalent, so in total I consider 3 distinct axes of rotation (imagine Figure 4.6 without an Au-substrate). On a substrate, Figure 4.6 shows four axes of rotation θ, Φ, α and β, I will discuss this later.

Figure 4.7 shows how these axes pass through the metallic moieties. For each of the four axes of rotation, I investigate how the total energy varies with angle of rotation, both in presence and absence of the gold substrate. For each of these four axes, I consider one mode of rotation in the gas phase and three modes of rotation on a substrate, I will discuss this later.

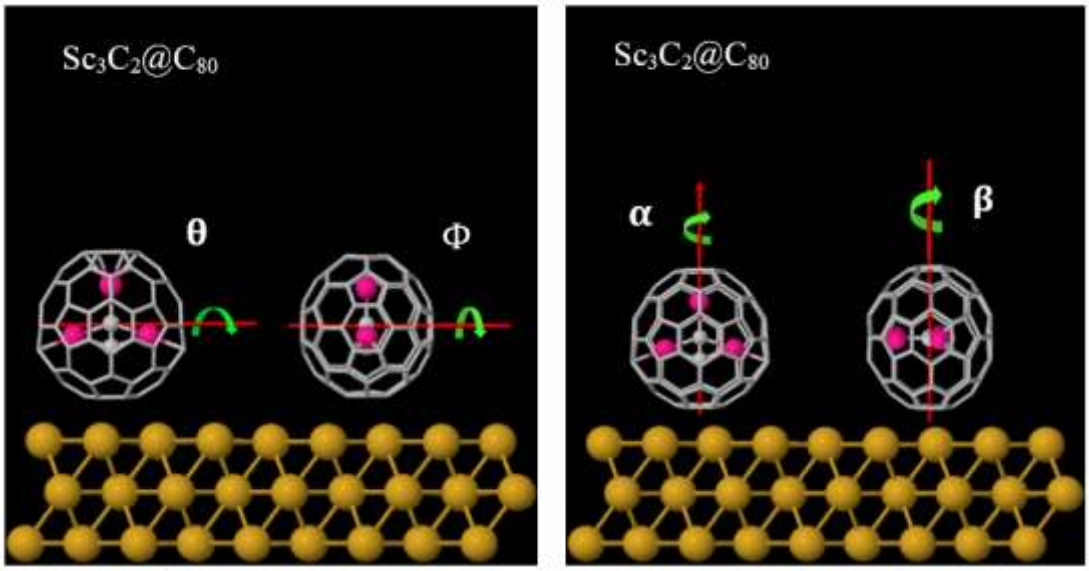

Figure 4.6. Illustration of the four rotation axes: θ, Φ are horizontal axes, α and β are vertical axes.

This Figure shows how the axes pass through the I_h-C_{80} cage + metallic moiety.

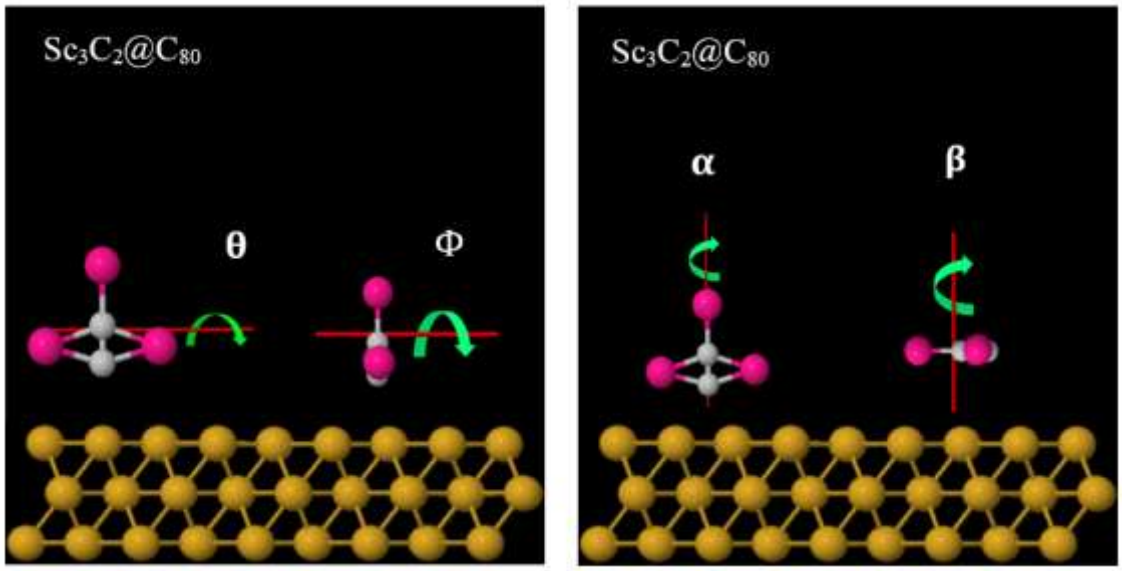

Figure 4.7. Illustration of how the four rotation axes θ, Φ, α and β, pass through the metallic moiety.

In what follows, the same symbol (e.g. θ) is used to label both the rotation axis and the angle of rotation about the axis.

4.6 Distance between the metallic moiety and the Au-substrate

In the gas phase, I consider rotation of the metallic moiety relative to a fixed fullerene cage. For this rotational mode, rotations about the β and Φ axes are equivalent, so in the gas phase, rotations about 3 distinct axes are investigated. In the presence of the gold substrate, I consider three modes of rotation about each of the four axes: rotation of the bare metallic moiety (in the absence of the cage), rotation of the metallic moiety in the presence of a fixed cage, and rotation of both the metallic moiety and cage, such that their relative orientation is fixed.

4.6.1 Distance between the metallic moiety and the Au-substrate of $Sc_3C_2@C_{80}$

Figure 4.8 illustrates how d varies during rotations about the four different rotation axes θ, Φ, α and β, and shows that rotation about θ causes the largest distance variation (black curve), followed by rotation about Φ (brown curve). In contrast, by symmetry, rotation about α and β causes no change in d (dark green or red curves, respectively).

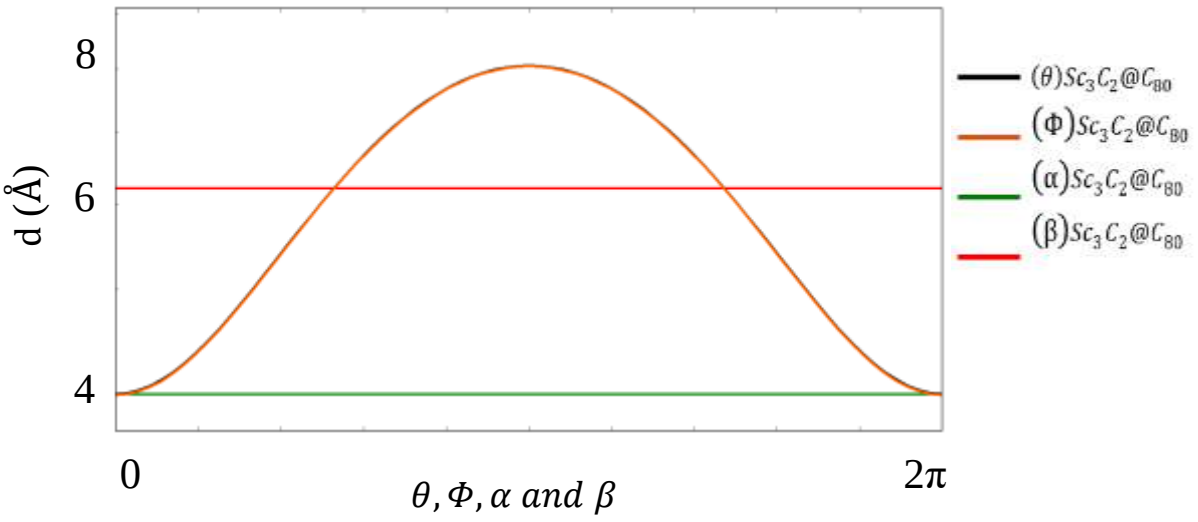

Figure 4.8. Distance variation between the metallic moiety and the gold substrate in four different rotation axes θ, Φ, α and β of $Sc_3C_2@C_{80}$.

4.6.2 Distance between the metallic moiety and the Au-substrate of $Sc_3N@C_{80}$

Figure 4.9 illustrates how d varies during rotations about the four different rotation axes θ, Φ, α and β, and shows that rotation about θ cause the largest distance variation (grey curve), followed by rotation about Φ (orange curve). In contrast, by symmetry, rotation about α and β causes no change in d (light green or pink curves, respectively).

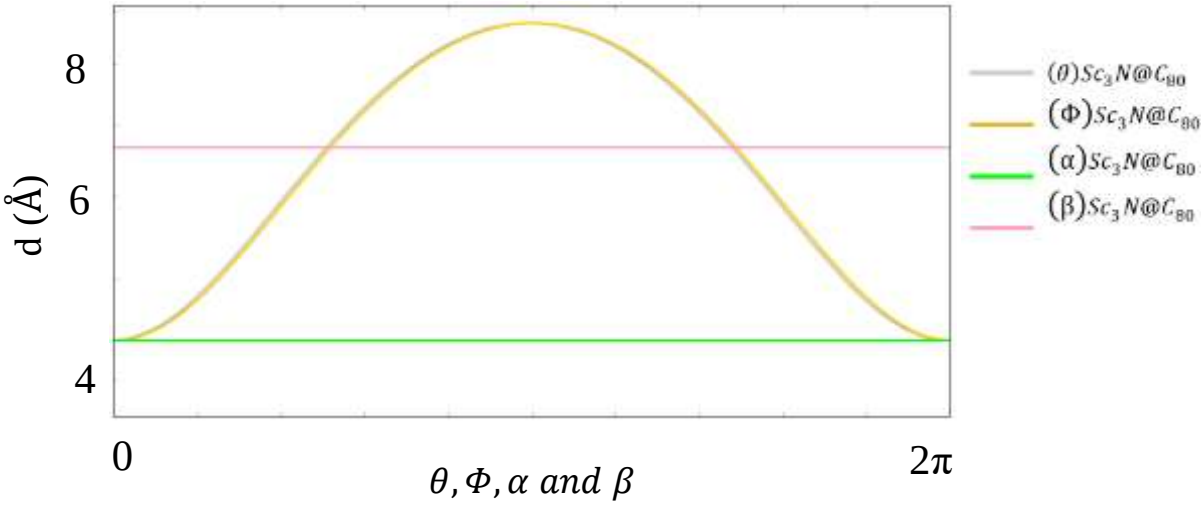

Figure 4.9. Distance variation between the metallic moiety and the gold substrate in four different rotation axes θ, Φ, α and β of $Sc_3N@C_{80}$.

4.6.3 Distance between the metallic moiety and the Au-substrate of $Er_3N@C_{80}$

Figure 4.10 illustrates how d varies during rotations about the four different rotation axes θ, Φ, α and β, and shows that rotation about θ cause the largest distance variation (light blue curve), followed by rotation about Φ (brown curve). In contrast, by symmetry, rotation about α and β causes no change in d (light yellow purpel curves, respectively).

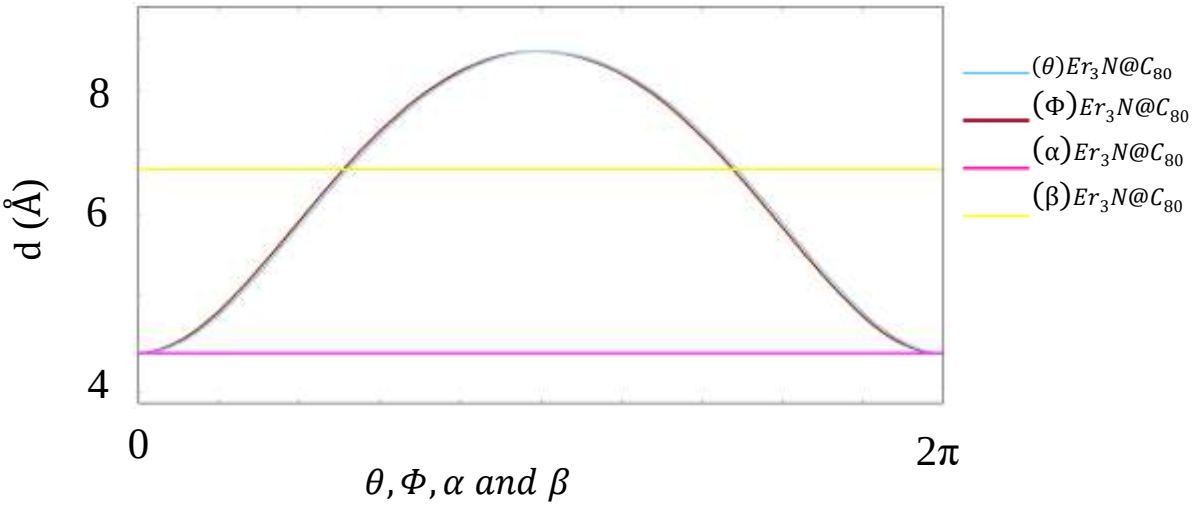

Figure 4.10. Distance variation between the metallic moiety and the gold substrate in four different rotation axes θ, Φ, α and β of $Er_3N@C_{80}$.

One should notice that $Sc_3N@C_{80}$ and $Er_3N@C_{80}$ have identical results, due to the fact that the two moieties (Sc_3N and Er_3N), have the same number of atoms and shape (see Figure 4.16). For clarity, I shall compare $Sc_3C_2@C_{80}$ against $Sc_3N@C_{80}$, as shown in Figure 4.11. This Figure shows that rotation about θ causes the largest distance variation (black and grey curves), followed by rotation about Φ (brown and orange curves). In contrast, by symmetry, rotation about α and β causes no change in d (light and dark green or red and pink curves, respectively). Furthermore, the distance variation d of $Sc_3N@C_{80}$ in general is higher than $Sc_3C_2@C_{80}$ in the 4 axes. This is again due to the number of atom in Sc_3N is less and the shape is more symmetric compared Sc_3C_2 as shown in Figure 4.16.

To quantify this variation, Table 4.4 shows the standard deviation σ of the distance d, associated with rotations about the four axes. This shows that the standard deviations σ follow the order $\sigma_\theta > \sigma_\Phi > \sigma_\alpha = \sigma_\beta$.

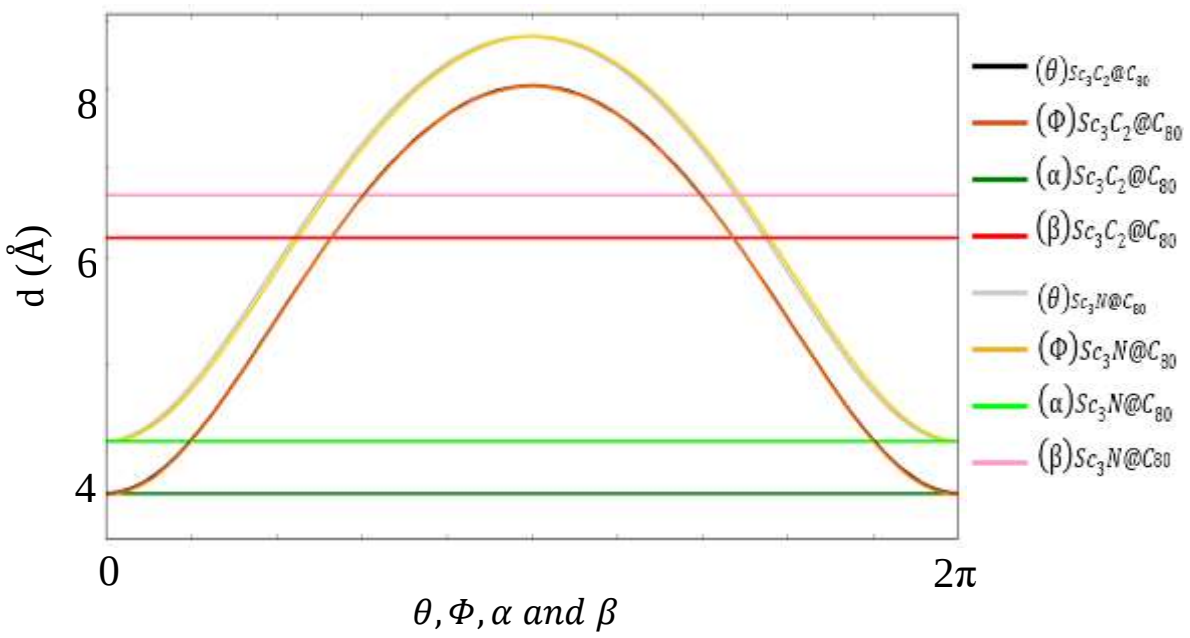

Figure 4.11. Distance variation between the metallic moiety and the gold substrate in four different rotation axes θ, Φ, α and β of $Sc_3C_2@C_{80}$, and $Sc_3N@C_{80}$.

Table 4.4: Standard deviations σ of the distance d, associated with rotations about the four axes, for the three EMFs $Sc_3C_2@C_{80}$, $Sc_3N@C_{80}$ and $Er_3N@C_{80}$. In the latter case, the distance d is defined to be the smallest vertical distance between the top-most plane of the Au substrate and the closest Er atom.

	σ_d (Å)			
EMF	σ_θ	σ_Φ	σ_α	σ_β
$Sc_3C_2@C_{80}$	1.47	1.09	0	0
$Sc_3N@C_{80}$	1.43	0.95	0	0
$Er_3N@C_{80}$	1.43	0.95	0	0

4.7 Gas phase energy barriers to rotation for the 3 moieties within a I_h-C_{80} cage

In this section, the metallic moieties Sc_3C_2, Sc_3N or Er_3N are rotated about horizontal axes θ and Φ and about a vertical axis α using equation (4.1) as shown in Figure 4.12. Following equation (4.1), the angle-dependent energy differences $\Delta(\theta)$, $\Delta(\Phi)$ and $\Delta(\alpha)$ are defined to be

$$\left.\begin{aligned}\Delta(\theta) &= E_{AB}^{AB}(\theta) - E_A^{AB} - E_B^{AB}\\ \Delta(\Phi) &= E_{AB}^{AB}(\Phi) - E_A^{AB} - E_B^{AB}\\ \Delta(\alpha) &= E_{AB}^{AB}(\alpha) - E_A^{AB} - E_B^{AB}\end{aligned}\right\} \quad (4.1)$$

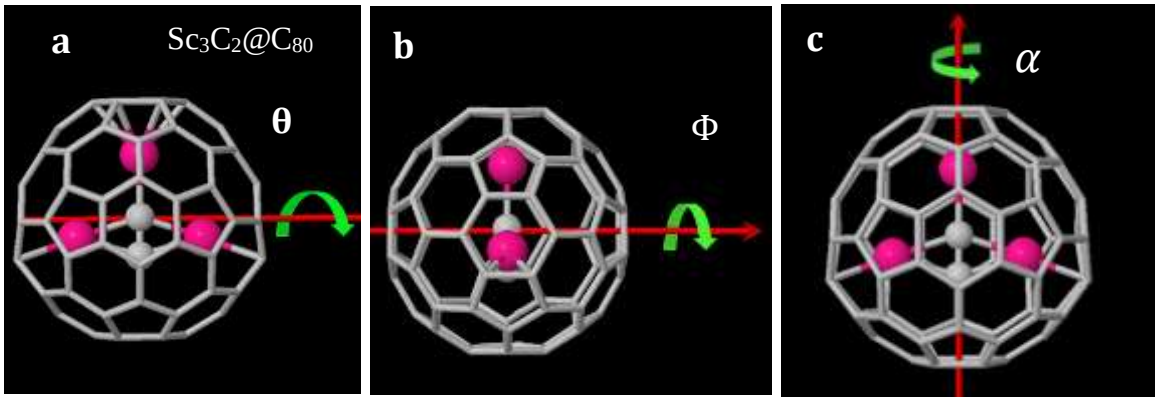

Figure 4.12. (a): Horizontal rotation axis used to compute $\Delta(\theta)$, **(b):** Horizontal rotation axis used to compute $\Delta(\Phi)$, **(c):** Vertical rotation axis used to compute $\Delta(\alpha)$, ($Sc_3C_2@C_{80}$ shown here as an example).

4.7.1 Gas phase energy barriers to rotation for Sc_3C_2 within a I_h-C_{80} cage

Figure 4.13 shows the gas-phase energy differences $\Delta(\theta)$ of $Sc_3C_2@C_{80}$ as a function of the rotation angle θ of the Sc_3C_2 inside the cage. This shows that the energy barrier to rotation about this horizontal axis is approximately 400 meV, and that the Sc_3C_2 within the fullerene cage have preferred

orientations θ of approximately 0°, 190° and 360°. The energy barrier to rotation Φ is 350 meV , and therefore the moiety Sc_3C_2 has preferred orientations of Φ ≈ (0°, 110°, 180°, 210°, 270° and 360°). The energy barrier to rotation α is 300 meV, and therefore the moiety Sc_3C_2 has preferred orientations of α ≈ (0°, 75°, 160°, 240° and 320°).

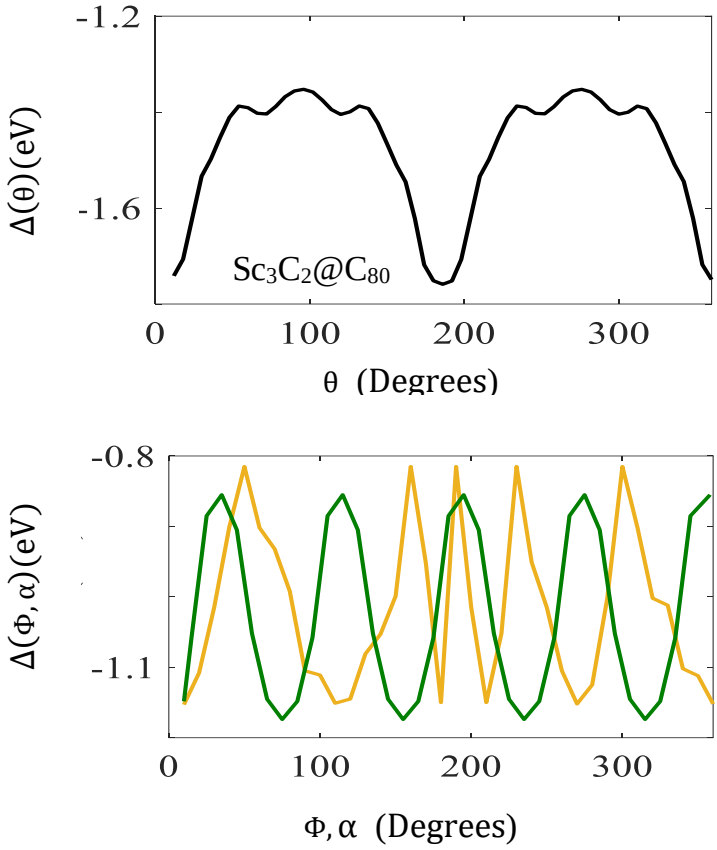

Figure 4.13. Top panel: The energy difference Δ(θ) as a function of rotation angle θ of Sc_3C_2within the fixed I_h-C_{80} cage**. Bottom panel:** The energy differecne Δ(Φ, α) as a function of rotation angles Φ and α (orange and green respectively), of Sc_3C_2 within the fixed I_h-C_{80} cage. The energy barriers ΔE(θ) to rotation about θ (obtained from the difference between the maxima and minima of $\Delta(\theta)$) are 400, 300 and 130 meV respectively, and the moiety Sc_3C_2 has preferred orientations of θ ≈ 0°, 190° and 360°, corresponding to the minima of $\Delta(\theta)$. The energy barriers ΔE(Φ) to rotation about Φ are 350, 250 and 100 meV respectively, and therefore the moiety Sc_3C_2 has preferred orientations of Φ ≈ (0°, 110°, 180°, 210°, 270° and 360°). The energy barriers to rotation about α are

300, 150 and 60 meV respectively, and therefore the moiety Sc_3C_2 has preferred orientations of $\alpha \approx$ (0°, 75°, 160°, 240° and 320°).

4.7.2 Gas phase energy barriers to rotation for Sc_3N within a I_h-C_{80} cage

Figure 4.14 shows the gas-phase energy differences $\Delta(\theta)$ of $Sc_3N@C_{80}$ as a function of the rotation angle θ of the Sc_3N inside the cages. This shows that the energy barrier to rotation about this horizontal axis is approximately 300 meV, and that the Sc_3N within the fullerene cage have preferred orientations θ of approximately 0°, 190° and 360°. The energy barrier to rotation Φ is 250 meV , and therefore the moiety Sc_3N have preferred orientations of $\Phi \approx$ (10°, 95°, 200°, 280° and 340°). The energy barrier to rotation α is 300 meV, and therefore the moiety Sc_3N has preferred orientations of $\alpha \approx$ (0°, 75°, 100°, 150°, 200° 250°, 300° and 350°)

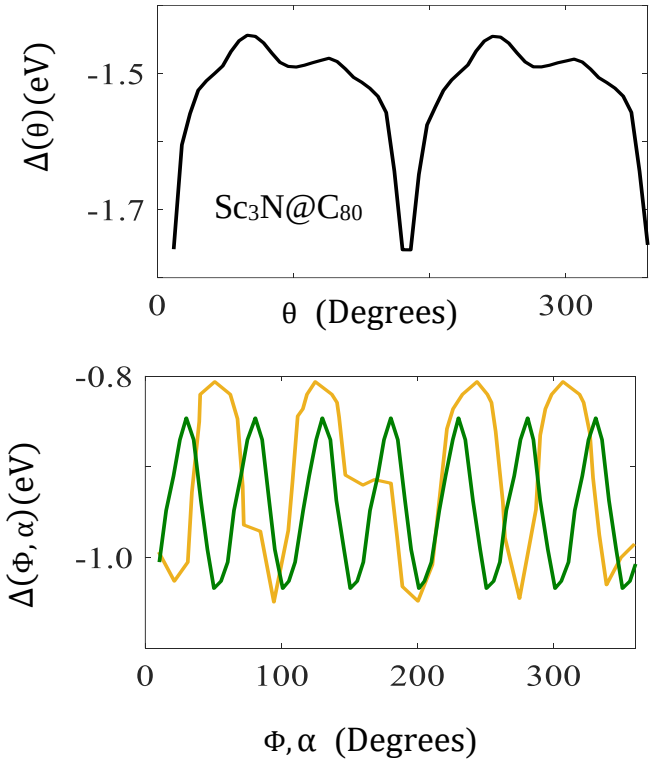

Figure 4.14. Top panel: The energy difference $\Delta(\theta)$ as a function of rotation angle θ of Sc_3Nwithin the fixed I_h-C_{80} cage**. Bottom panel:** The energy differecne $\Delta(\Phi, \alpha)$ as a function of rotation angles Φ and α (yellow and green respectively), of Sc_3N within the fixed I_h-C_{80} cage. The energy barriers

$\Delta E(\theta)$ to rotation about θ (obtained from the difference between the maxima and minima of $\Delta(\theta)$) are 400, 300 and 130 meV respectively, and the moiety Sc_3N has preferred orientations of $\theta \approx$ 0°, 190° and 360°, corresponding to the minima of $\Delta(\theta)$. The energy barriers $\Delta E(\Phi)$ to rotation about Φ are 350, 250 and 100 meV respectively, and therefore the moiety Sc_3N has preferred orientations of $\Phi \approx$ (10°, 95°, 200°, 280° and 340°). The energy barriers to rotation about α are 300, 150 and 60 meV respectively, and therefore the moieties Sc_3N has preferred orientations of $\alpha \approx$ (0°, 75°, 100°, 150°, 200° 250°, 300° and 350°).

4.7.3 Gas phase energy barriers to rotation for Er_3N within a I_h-C_{80} cage

Figure 4.15 shows the gas-phase energy differences $\Delta(\theta)$ of $Er_3N@C_{80}$ as a function of the rotation angle θ of the Er_3N inside the cages. This shows that the energy barrier to rotation about this horizontal axis is approximately 130 meV, and that the Er_3N within the fullerene cage have preferred orientations θ of approximately 0°, 190° and 360°. The energy barrier to rotation Φ is 100 meV , and therefore the moiety Er_3N has preferred orientations of $\Phi \approx (0°, 120°, 250° \text{ and } 350°)$. The energy barrier to rotation α is 300 meV, and therefore the moiety Er_3N has preferred orientations of $\alpha \approx$ (0°, 80°, 150°, 225°, 320°and 360°

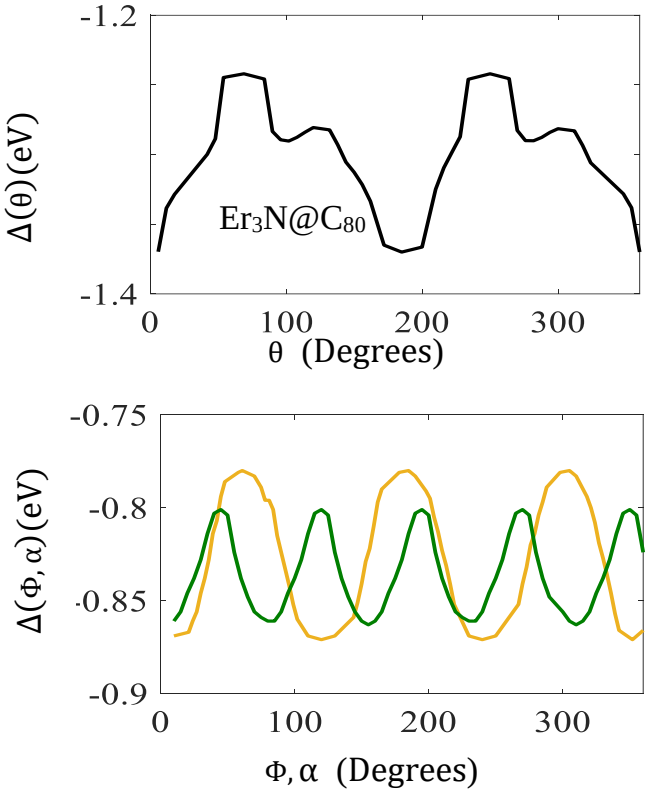

Figure 4.15. Top panels: The energy difference $\Delta(\theta)$ as a function of rotation angle θ of Er_3N within the fixed I_h-C_{80} cage**. Bottom panels:** The energy differecne $\Delta(\Phi, \alpha)$ as a function of rotation angles Φ and α (yellow and green respectively), of Er_3N within the fixed I_h-C_{80} cage. The energy barriers $\Delta E(\theta)$ to rotation about θ (obtained from the difference between the maxima and minima of $\Delta(\theta)$) are $400, 300$ and 130 meV respectively, and the moiety Er_3N has preferred orientations of $\theta \approx 0°, 190°$ and $360°$, corresponding to the minima of $\Delta(\theta)$. The energy barriers $\Delta E(\Phi)$ to rotation about Φ are $350, 250$ and 100 meV respectively, and therefore the moiety Er_3N has preferred orientations of $\Phi \approx (0°, 120°, 250°$ and $350°)$. The energy barriers to rotation about α are $300, 150$ and 60 meV respectively, and therefore the moiety Er_3N has preferred orientations of $\alpha \approx (0°, 80°, 150°, 225°, 320°$and $360°)$.

Table 4.5: Gas phase energy barriers $\Delta E(\theta), \Delta E(\Phi), \Delta E(\alpha)$ associated with rotations about θ, Φ, α of Sc_3C_2, Sc_3N and Er_3N within the fixed I_h-C_{80} cage, along with the preferred orientations angles for the three rotation axes.

EMF	**$\Delta E(\theta)$ meV**	**Preferred orientations (θ)**	**$\Delta E(\Phi)$ meV**	**Preferred orientations (Φ)**	**$\Delta E(\alpha)$ meV**	**Preferred orientations (α)**
Sc_3C_2@ C_{80}	400	0°, 190° and 360°	350	0°, 110°, 180°, 210°, 270° and 360°	300	0°, 75°, 160°, 240° and 320°
Sc_3N@C_{80}	300	0°, 190° and 360°	250	10°, 95°, 200°, 280° and 340°	150	0°, 75°, 100°, 150°, 200° 250°, 300° and 350°
Er_3N@C_{80}	130	0°, 190° and 360°	100	0°, 120°, 250° and 350°	60	0°, 80°, 150°, 225°, 320°and 360°

Table 4.5 shows the energy barrier $\Delta E(\theta)$ for Er_3N inside the C_{80} cage is of order 130 meV, which means that the Er_3N cluster rotates more easily than the scandium-based moieties, Sc_3N and Sc_3C_2. Table 4.5 also shows that the barrier to rotation about a vertical axis $\Delta E(\alpha)$ is even lower, at approximately 60 meV.

Figure 4.16 shows a comparison between the Sc_3C_2, Sc_3N and Er_3N moieties. This figure shows there are 5 atoms in Sc_3C_2 moiety and 4 atoms in Sc_3N and Er_3N moieties. It also shows that Sc_3N and Er_3N have an identical shape and are more symmetric than Sc_3C_2.

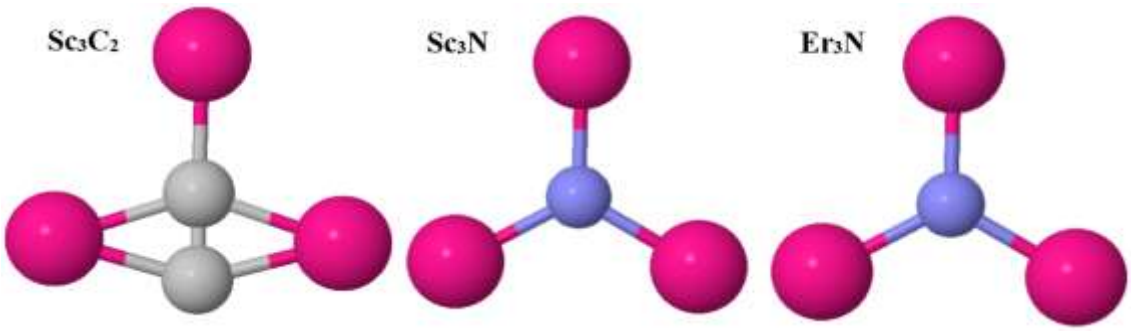

Figure 4.16. Geometries of Sc_3C_2, Sc_3N and Er_3N metallic moieties (left to right).

4.8 Charge transfer analyses of EMFs on an Au substrate

In this section, I shall repeat the above calculations of the charge transfer, but on an Au substrate. In the gas phase analyses, the focus was on two parameters, the metallic moiety and the cage. In on a substrate, there are extra features associated with the presence of the substrate.

4.8.1 Charge transfer analyses of $Sc_3C_2@C_{80}$ EMF

As mentioned above, the analyses here are built on the 3 factors, namely a metallic moiety, a cage and a substrate. Table 4.6 shows the amount of charge transfer from the metallic moiety Sc_3C_2 and a gold substrate to I_h-C_{80} cage. Table 4.6 shows that the metallic moiety Sc_3C_2 and substrate lose (+) in total 1.635 electrons. 1.391 is the net charge that has been gained (-) by the I_h-C_{80} cage, the difference of 0.244 electrons resides in the space between the metallic moiety Sc_3C_2 and I_h-C_{80} cage, as estimated by the Mulliken method. Hirshfeld and Voronoi charges follow similar trends; the net charges are 1.137 and 1.112 electrons respectively.

Table 4.6: Charge transfer immigration among three segments including metallic moiety, cage and Au substrate. Mulliken, Hirshfeld and Voronoi methods are used to analyse the cahrge transfer for $Sc_3C_2@C_{80}$ EMF.

Metallic Moiety	Mulliken charge		Hirshfeld charge		Voronoi charge	
	Moiety + Au	I_h-C_{80} cage	Moiety + Au	I_h-C_{80} cage	Moiety + Au	I_h-C_{80} cage
Sc_3C_2	+1.635	-1.391	+1.137	-0.648	+1.112	-0.562

4.8.2 Charge transfer analyses of $Sc_3N@C_{80}$ EMF

Table 4.7 shows the charge transfers from the metallic moiety Sc_3N and a gold substrate to I_h-C_{80} cage. Table 4.7 illustrates that the metallic moiety Sc_3N and substrate lose (+) in total 2.37 electrons. 1.96 is the net charge gained (-) by the I_h-C_{80} cage. The difference 0.41 remains in the space between the metallic moiety Sc_3C_2 and I_h-C_{80} , as estimated by the Mulliken method. Hirshfeld and Voronoi methods follow a net charge of 1.32 and 1.28 electron respectively.

Table 4.7: Charge transfer immigration among three segments including metallic moiety, cage and Au substrate. Mulliken, Hirshfeld and Voronoi methods are used to analyse the cahrge transfer for $Sc_3N@C_{80}$ EMF.

Metallic Moiety	Mulliken charge		Hirshfeld charge		Voronoi charge	
	Moiety + Au	I_h-C_{80} cage	Moiety + Au	I_h-C_{80} cage	Moiety + Au	I_h-C_{80} cage
Sc_3N	+2.379	-1.967	+1.320	-0.887	+1.286	-0.803

4.8.3 Charge transfer analyses of $Er_3N@C_{80}$ EMF

Table 4.8 shows the charge transfers from the metallic moiety Er_3N and a gold substrate to I_h-C_{80} cage. Table 4.8 reveals that the metallic moiety Er_3N and substrate lose (+) in total 1.87 electrons. 0.32 is the net charge gained (-) by the I_h-C_{80} cage. The difference 1.545 resides in the space between the metallic moiety Sc_3C_2 and I_h-C_{80}, as estimated by the Mulliken method. Hirshfeld and Voronoi methods follow a net charge of 7.34 and 7.05 electrons respectively. However, the $Er_3N@C_{80}$ EMF is inaccurate owing to the presence of *f*-electrons; hence, I am unable to compute the electrical conductance G and Seebeck coefficients S in my thesis.

Table 4.8: Charge transfer immigration among three segments including metallic moiety, cage and Au substrate. Mulliken, Hirshfeld and Voronoi methods are used to analyse the cahrge transfer for $Er_3N@C_{80}$ EMF.

Metallic Moiety	Mulliken charge		Hirshfeld charge		Voronoi charge	
	Moiety + Au	I_h-C_{80} cage	Moiety + Au	I_h-C_{80} cage	Moiety + Au	I_h-C_{80} cage
Er_3N	+1.870	-0.325	+7.342	-5.983	+7.056	-5.709

4.9 Binding energies of EMFs and C_{60} on a gold surface

For calculating binding energies, the counterpoise method described in chapter 2, section 2.5 will be employed. In this section, I calculate the optimum binding distance between the gold (111) surface and the EMFs/C_{60}. I use DFT, combined with the counterpoise method, which removes basis set superposition errors (BSSE).

The ground state energy of the total system is calculated using SIESTA [7] and is denoted E_{AB}^{AB}. Here, the gold lead consists of 3 layers of 25 atoms. The EMFs and C_{60} molecules are defined as monomer A and the gold electrode as monomer B. The binding energy of each molecules is then calculated in a fixed basis, which is achieved through the use of ghost atoms in SIESTA. Hence, the energy of the isolated EMFs and C_{60} molecules in the presence of the fixed basis is defined as E_A^{AB} and for the isolated gold is E_B^{AB}. The energy difference ($\Delta(z)$) between the isolated entities and their total energy when placed a distance z apart is then calculated using the following equation:

$$\text{Energy difference } = \Delta(z) = E_{AB}^{AB}(z) - E_A^{AB} - E_B^{AB} \tag{4.2}$$

5.9.1 Binding energies of $Sc_3C_2@C_{80}$ EMF

As shown by the Figure 4.17, the equilibrium distance for $Sc_3C_2@C_{80}$, corresponding to the minimum energy difference, is found to be approximately 2.5 Å. with an energy value about 0.9 eV, using equation 4.2.

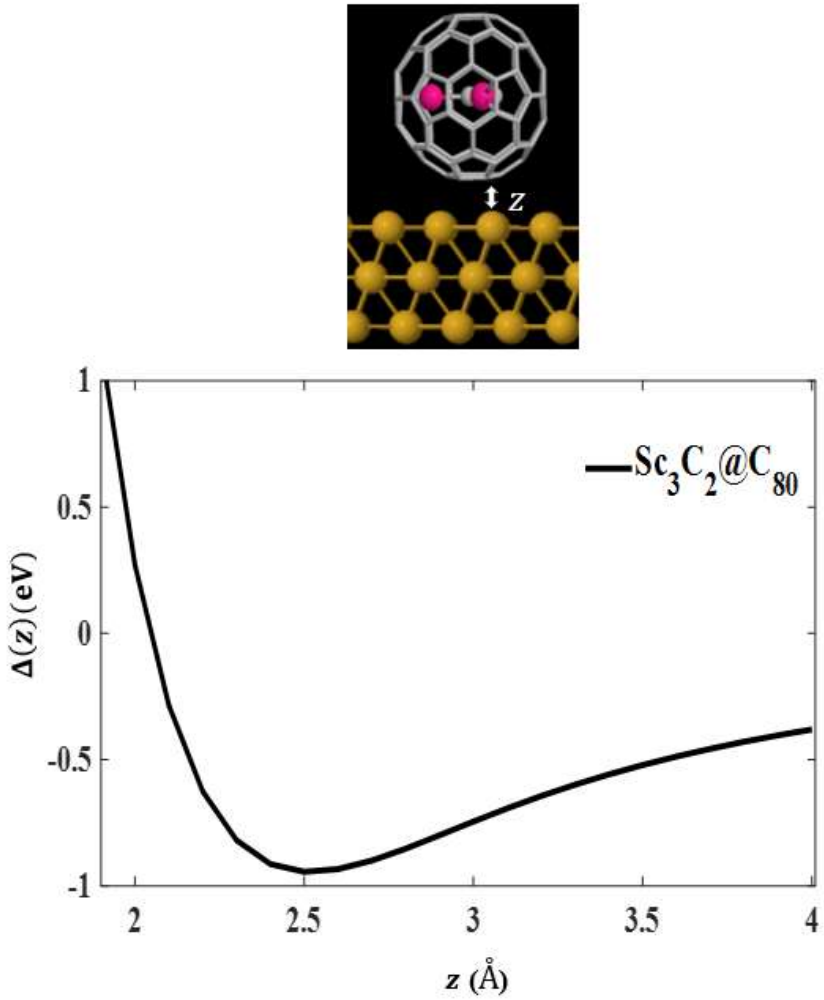

Figure 4.17. $Sc_3C_2@C_{80}$ on a gold surface (**Top panel**). Energy difference of $Sc_3C_2@C_{80}$/gold complex as a function of molecule-gold distance. The equilibrium distance corresponding to the energy minimum is found to be approximately 2.5 Å (**Bottom panel**).

5.9.2 Binding energies of the $Sc_3N@C_{80}$ EMF

As shown by the Figure 4.18, the equilibrium distance for $Sc_3N@C_{80}$, corresponding to the minimum energy difference, is found to be approximately 2.5 Å, with an energy value about 0.45 eV. The equilibrium distance 2.5 Å, that theoretically calculated for the same EMF by [13].

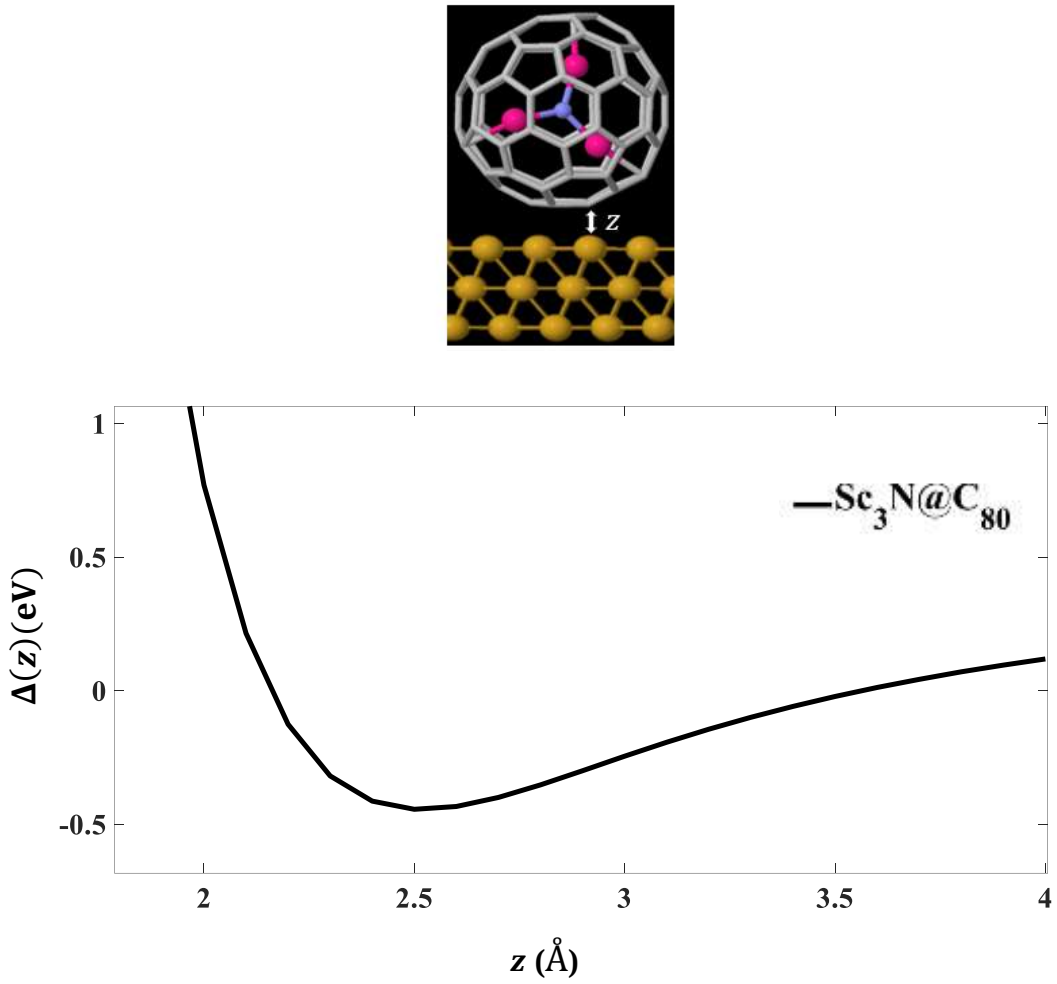

Figure 4.18. $Sc_3N@C_{80}$ on a gold surface (**Top panel**). Energy difference of $Sc_3N@C_{80}$/gold complex as a function of molecule-gold distance. The equilibrium distance corresponding to the energy minimum is found to be approximately 2.5 Å (**Bottom panel**).

5.9.3 Binding energies of C_{60}

As shown by the Figure 4.19, the equilibrium distance between the C_{60} cage and Au substrate, which is, corresponding to the minimum energy difference, is found to be approximately 2.5 Å. with an energy value of 0.9 eV.

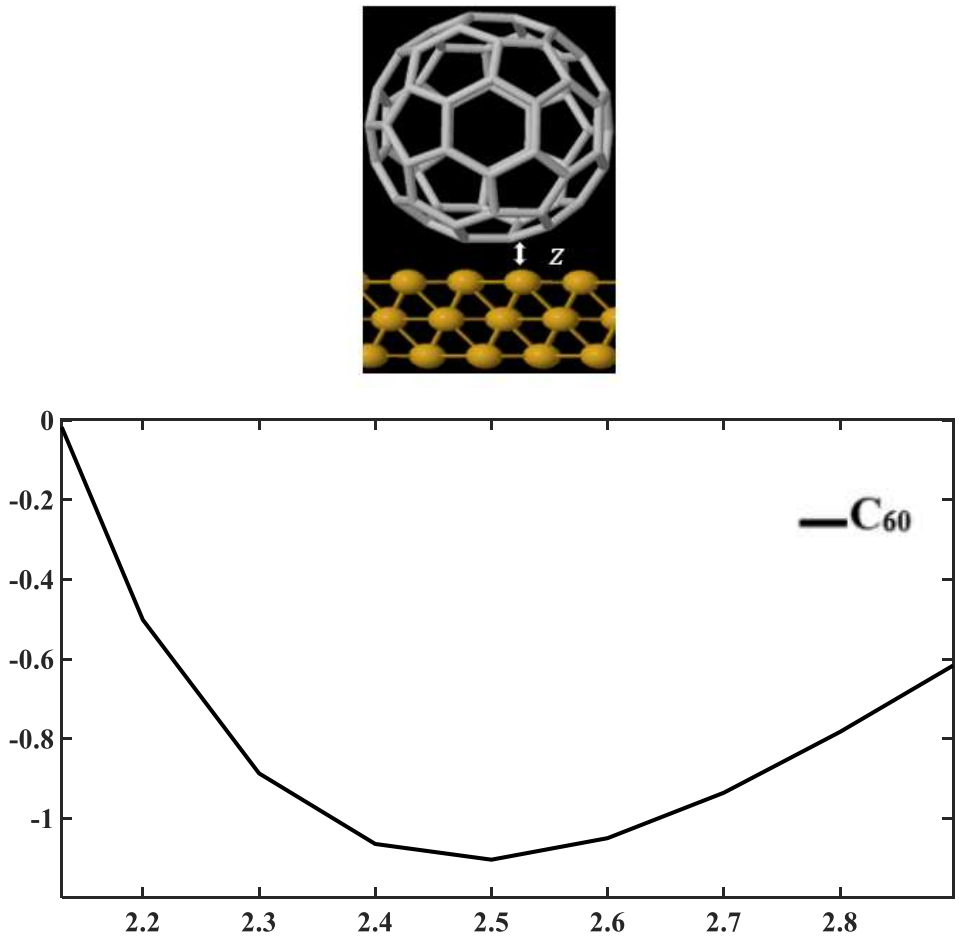

Figure 4.19. C_{60} on a gold surface (**Top panel**). Energy difference of C_{60}/gold complex as a function of molecule-gold distance. The equilibrium distance corresponding to the energy minimum is found to be approximately 2.5 Å (**Bottom panel**).

The equilibrium distance and energy difference for two EMFs including $Sc_3C_2@C_{80}$, $Sc_3N@C_{80}$ and an empty cage are shown in Table 4.9. This table shows that the energy difference of $Sc_3C_2@C_{80}$ is double than that $Sc_3N@C_{80}$, whereas the equilibrium distance is approximately similar. It is worth mentioning that, the equilibrium distance and energy difference have been not calculated to $Er_3N@C_{80}$.

This is because the electrical conductance and Seebeck coefficients of $Er_3N@C_{80}$ EMF are unreliable due to the fact that this EMF possesses *f*-electrons.

Table 4.9: Summarises the optimum distance (Å), and the binding energy (eV), of two EMFs and C_{60} cage.

Molecule	B. E (eV)	Optimum distance (Å)
$Sc_3C_2@C_{80}$	0.90	2.5
$Sc_3N@C_{80}$	0.45	2.5
$Er_3N@C_{80}$	==	==
C_{60}	1.1	2.5

4.10 Energy barriers to rotation for endohedral fullerenes on a gold (111) surface

Having discussed barriers to rotation in the gas phase, I now calculate the energy $\Delta(\theta)$ when the whole EMFs (cage plus metallic moiety) is rotated in the vicinity of a gold (111) surface, at various distances z relative to the surface. The rotation axis θ is shown in Figure 4.20 along with the definition of the distance z of EMF the relative to the Au surface for $Sc_3C_2@C_{80}$, $Sc_3N@C_{80}$ and $Er_3N@C_{80}$ EMFs.

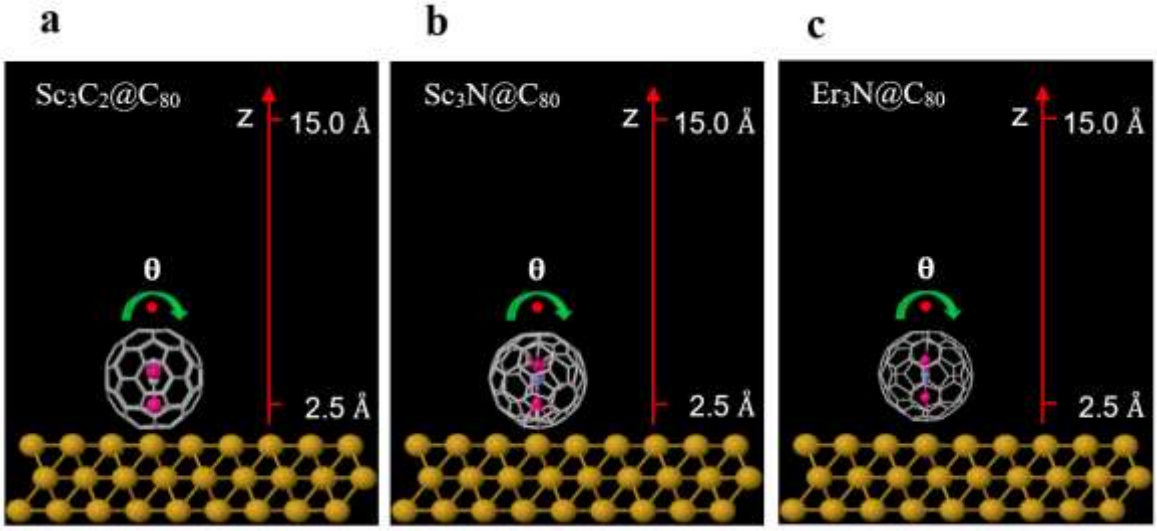

Figure 4.20. Illustration of the rotation axis θ and the Au-EMF distance (z) of **a:** $Sc_3C_2@C_{80}$, **b:** $Sc_3N@C_{80}$ and **c:** Er_3 $Er_3N@C_{80}$ used to compute the results in Figures 4.21 and 4.22.

For each of $Sc_3N@C_{80}$, $Sc_3C_2@C_{80}$ and $Er_3N@C_{80}$ EMF, Figure 4.21 shows the energy $\Delta(\theta)$ obtained at different Au-EMF distances z, starting from the optimum distance z = 2.5 Å (see Figures 4.17 and 4.18). At each distance z, $\Delta(\theta)$ is computed for values of θ ranging from 0 to 2π. At the optimum value z, the three black curves show that $Er_3N@C_{80}$ possesses the smallest rotation barrier ($\Delta E(\theta) = 0.1$ eV), whereas $Sc_3C_2@C_{80}$ and $Sc_3N@C_{80}$ possess energy barriers to rotation of $\Delta E(\theta) = 0.6$ eV and 0.3 eV, respectively. All those barriers decrease with increasing distance z, until they vanish at large z (z =15.0 Å, which is approximately equivalent to the gas phase of the whole EMF). The three green curves in Figure 4.21 show the corresponding energies obtained by rotating the metallic moieties alone in the vicinity of a gold surface in the absence of the C_{80} cage, at z = 2.5 Å (see Figure 4.7). This shows that for bare Sc_3C_2 and Sc_3N (i.e. in the absence of the cage, see Figure 4.7) the rotational energy barriers are slightly smaller and are negligible for the bare Er_3N.

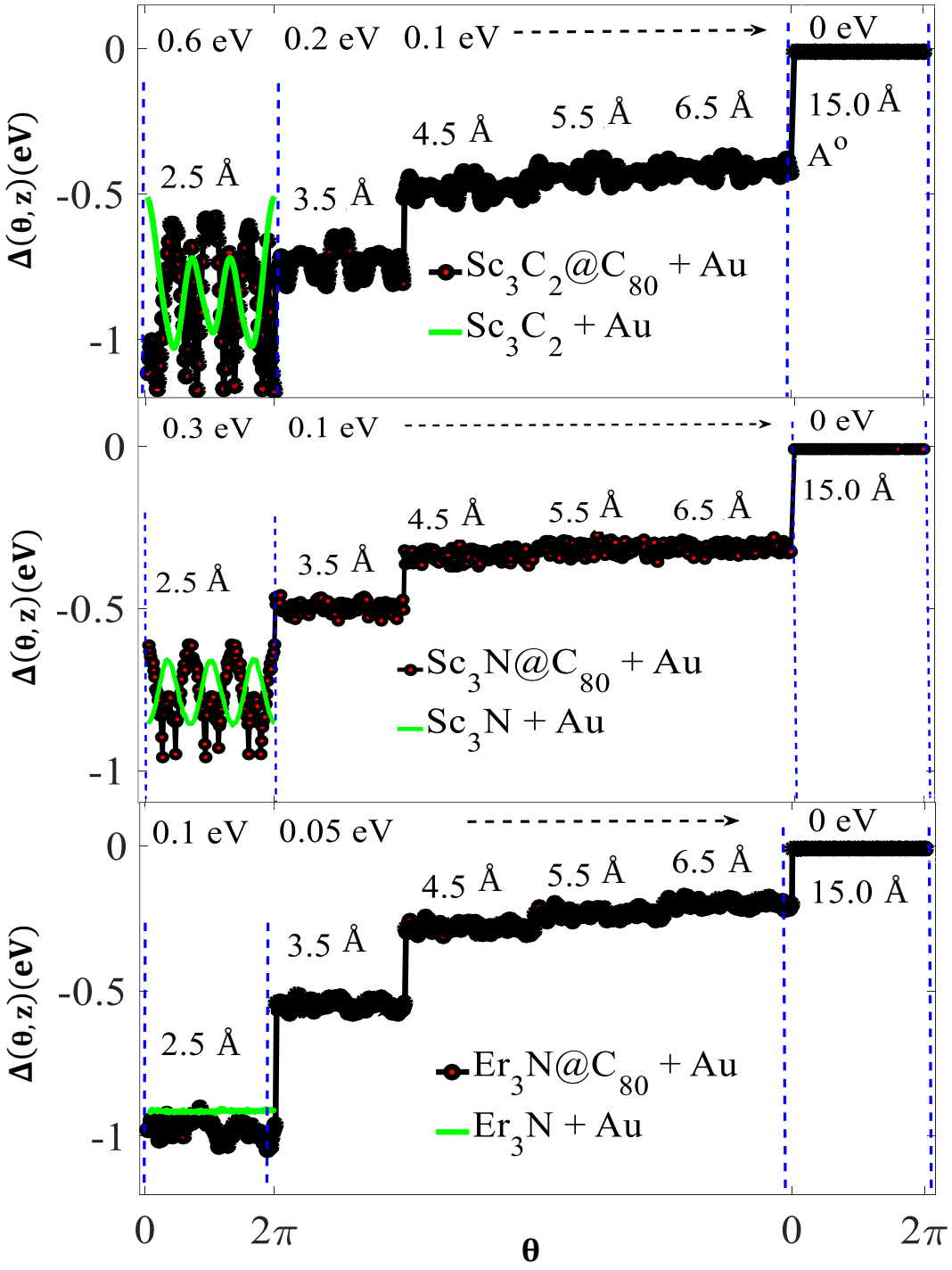

Figure 4.21. Rotational energy barriers of the three EMFs on a gold surface $Sc_3C_2@C_{80}$, $Sc_3N@C_{80}$ and $Er_3N@C_{80}$, respectively computed at different distances z from the surface, for the rotation axis θ. The energy barriers to rotation are of the order 0.6, 0.3 and 0.1 eV at z = 2.5 Å and tend to zero for large

z (black lines). The green curves show the energy barriers to rotation for the three bare metallic moieties near a gold surface, at z = 2.5 Å, in the absence of C_{80}. z = 15.0 Å, (black lines). The green curves show the energy barriers to rotation for the three bare metallic moieties near a gold surface, at z = 2.5 Å, in the absence of C_{80} cage.

It is worth mentioning that, in the above calculations, the whole EMF or just the bare metallic cluster were rotated in the vicinity of a gold substrate. As a separate check on the energy barriers, I now keep the cage at a fixed orientation and compute the energy $\Delta(\theta, z)$ versus z for rotation angles θ of the metallic cluster inside the cage, which correspond to the energy minima of Table 4.5.

For Sc_3C_2 moiety, (Figure 4.22a) the four different angles used are $\theta = 0°, 90°, 180°, 270°$. While for Sc_3N moiety (Figure 4.22b), the three different angles are $\theta = 0°, 90°, 180°$. The differences between the energy minima of these plots match the results of the middle panel of Figure 4.21. These results show that Sc_3C_2 possesses the highest barrier, in agreement with the top panel of Figure 4.21. On the other hand, For Er_3N, (Figure 4.22c) three different angles are used $\theta = 0°, 90°, 180°$. This shows that the energy barrier is relatively small and in agreement with the bottom panel of Figure 4.21.

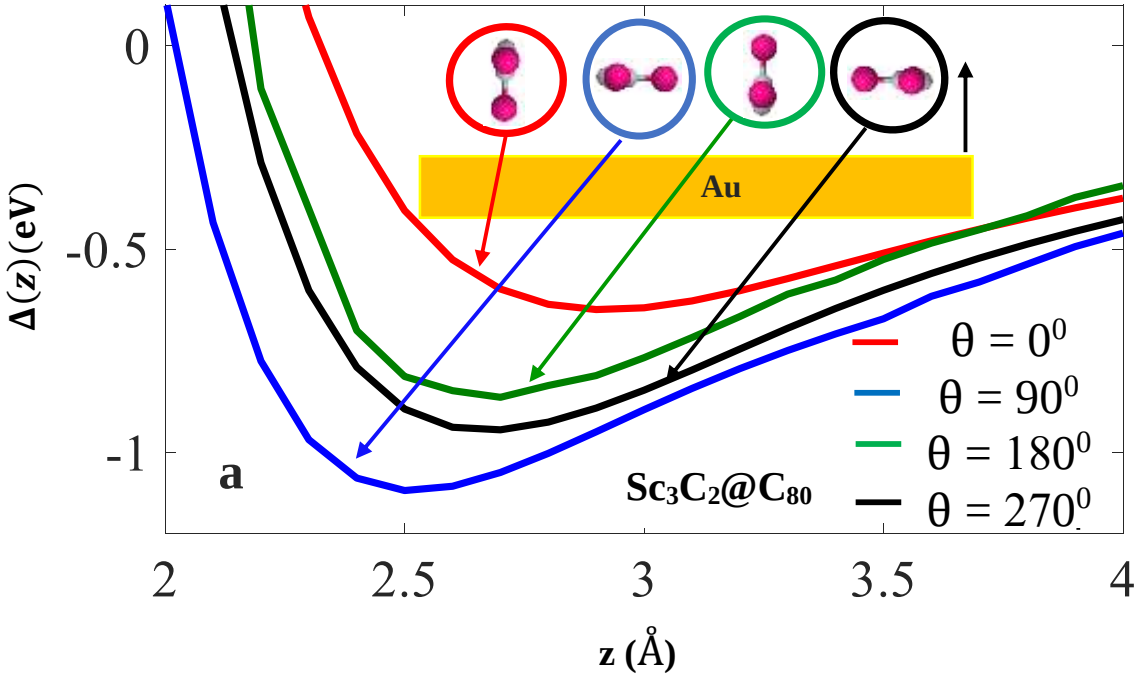

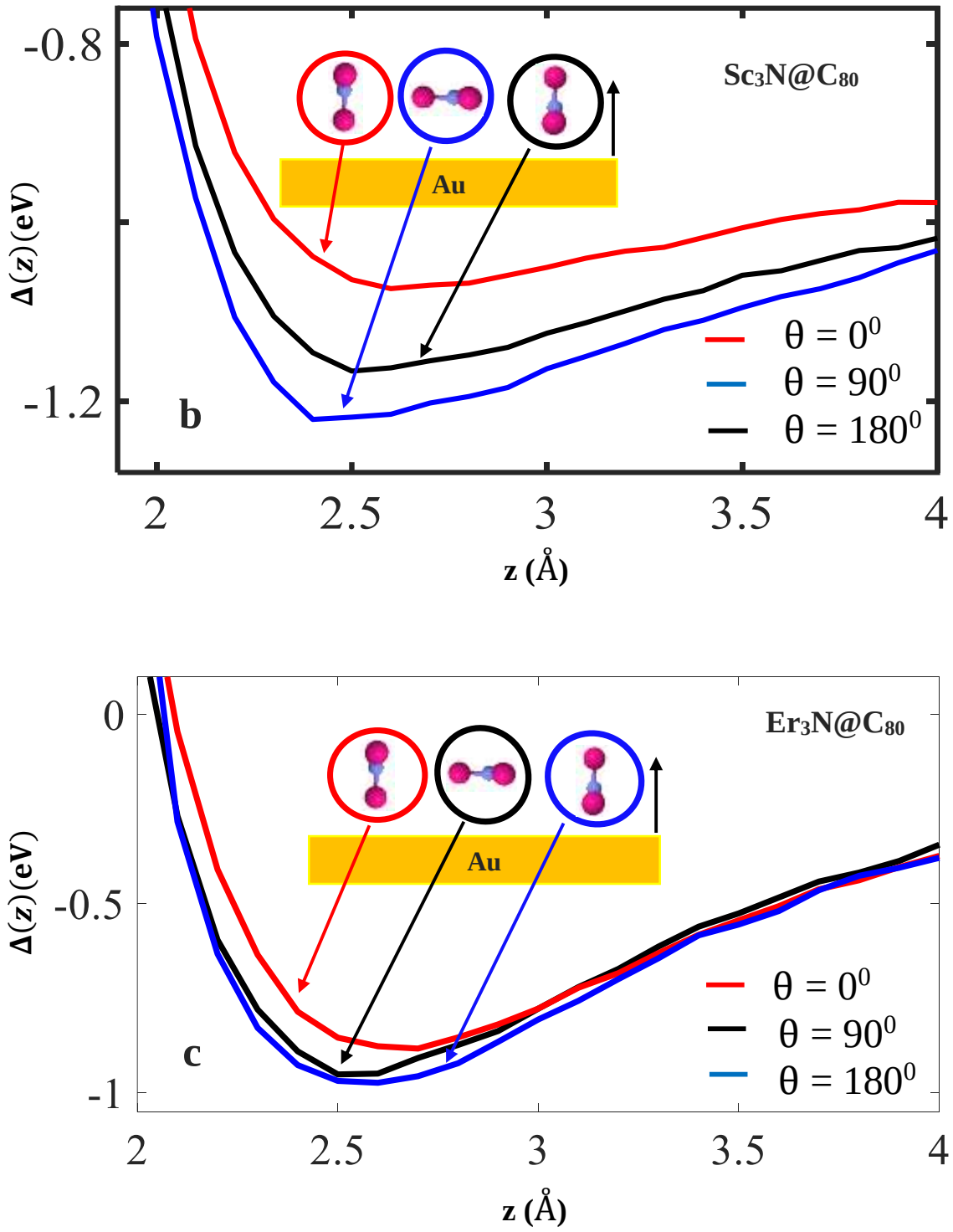

Figure 4.22. The energy difference $\Delta(z)$ as a function of the distance z for different orientations of the metallic clusters inside the cage **a, b** and **c** correspond to $Sc_3C_2@C_{80}$, $Sc_3N@C_{80}$, and $Er_3N@C_{80}$, respectively.

For a clearer picture, I now repeat the calculations shown in Figure 4.21 using the different rotation axes θ, Φ, α and β on the Au substrate as shown in Figure 4.23 as an example. I calculate the energies $\Delta(\theta), \Delta(\Phi), \Delta(\alpha), \Delta(\beta)$ when the whole EMF (cage plus metallic moiety) is rotated in the vicinity of a gold (111) surface.

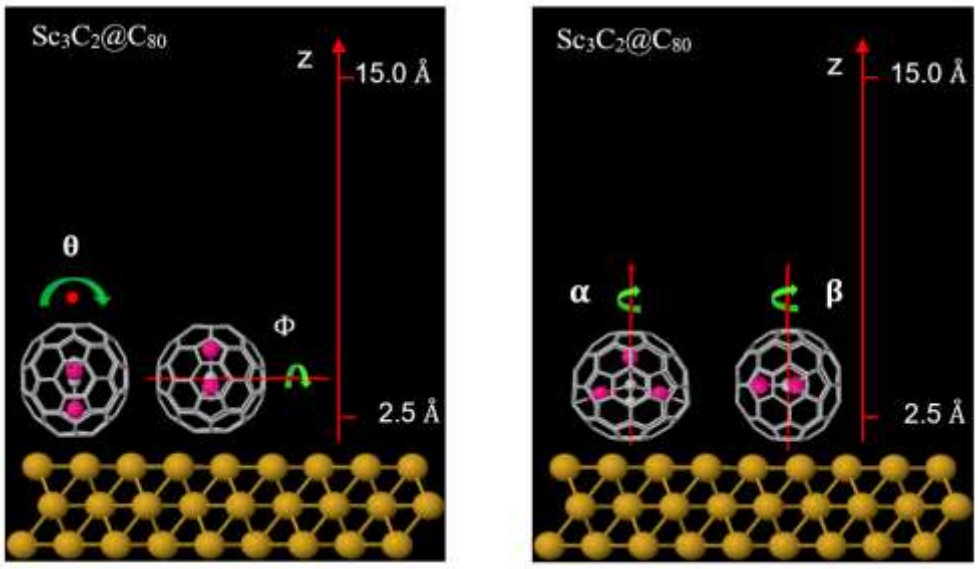

Figure 4.23. Illustration of the rotation axes and the Au-EMF distance (z), used to compute the results in Figure 4.24.

Figure 4.24 shows the binding energy is rather sensitive to rotation about the θ and Φ axes and are relatively insensitive to rotation about axes α and β. Consequently, the energy barriers to rotation follow the order $\Delta E(\theta) > \Delta E(\Phi) > \Delta E(\alpha) > \Delta E(\beta)$. This ordering illustrates a rather intuitive structure-function relation, because it is correlated with the standard deviations σ of Table 4.4, which follow the order $\sigma_\theta > \sigma_\Phi > \sigma_\alpha = \sigma_\beta$. This shows that large variations in the distance between the metal atom and the substrate lead to large variations in the binding energy and larger energy barriers to rotation, whereas the negligible variations in the distance associated with the α and β axes lead to much smaller energy barriers.

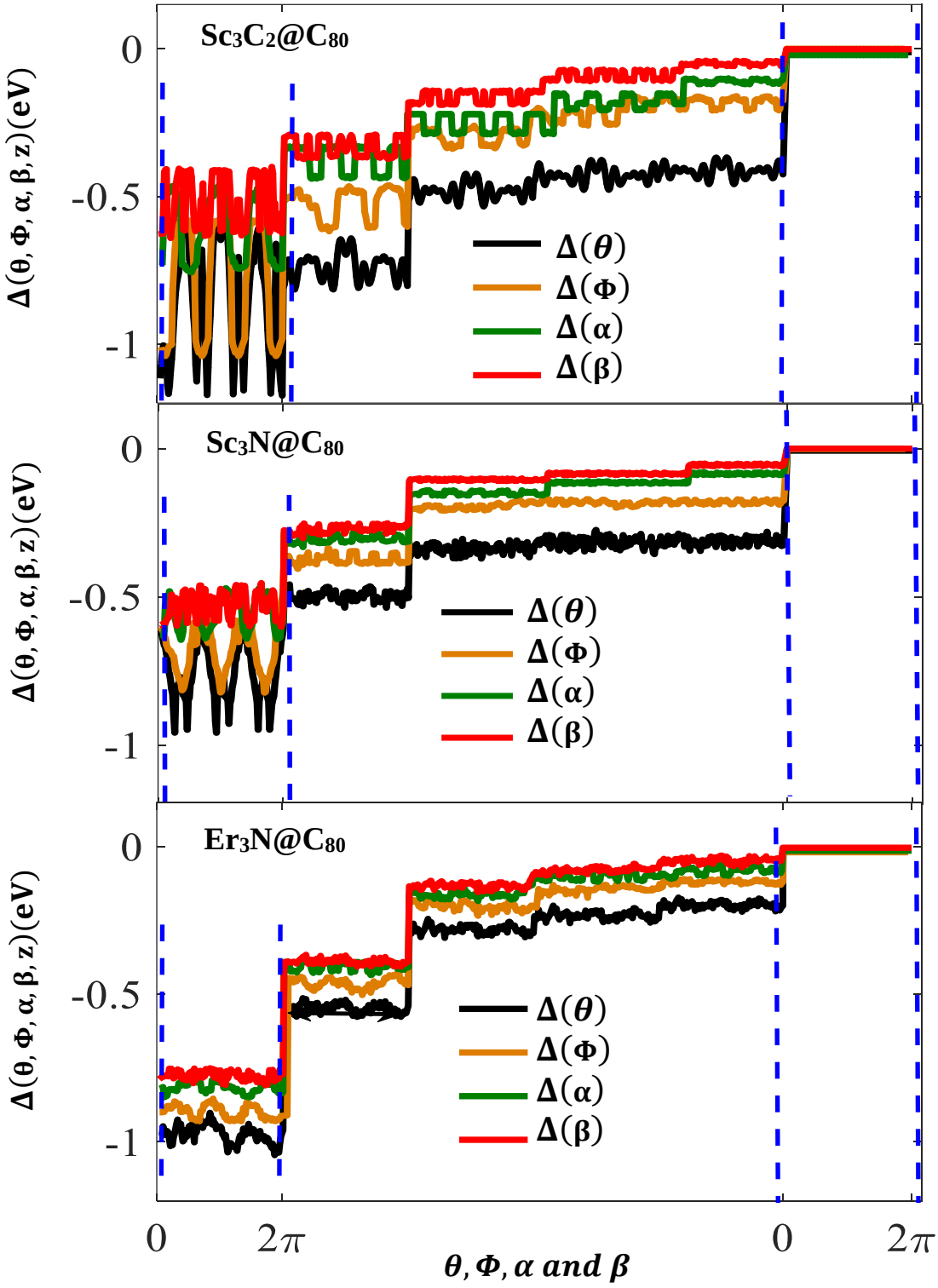

Figure 4.24. Rotational energy barriers of the three EMFs onto a gold surface $Sc_3C_2@C_{80}$, $Sc_3N@C_{80}$, and $Er_3N@C_{80}$, respectively as a function of rotation and distance to the surface in four rotational axes θ, Φ, α and β. The energy barrier to rotation (β-axes) is of the order of 0.25, 0.1 and 0.04 eV at z = 2.5 Å and tends to zero for large z (red lines z = 15.0 Å).

4.11 Conclusion

In summary, I studied the frontier orbital for the three EMFs and C_{60} molecules and find the degeneracy for the C_{60} cage is fivefold in the HOMO energy levels and threefold in the LUMO. I analysed the charge transfer trends of the three EMFs molecules in the gas-phase and on a gold substrate using Mulliken, Hirshfeld and Voronoi population analyses.

In the next step, I employed the DFT to examine the binding energies of these junctions under various rotation axes. There are an infinite number of different ways that the metallic parts of the fullerene cages can be oriented. I investigate how the total energy varies with angle of rotation, both in presence and absence of the gold substrate. I study the gas-phase energy differences $\Delta(\theta)$ of $Sc_3C_2@C_{80}$, $Sc_3N@C_{80}$ and $Er_3N@C_{80}$ EMFs as a function of the rotation angle θ, Φ, α of the Sc_3C_2, Sc_3N and Er_3N inside the cages. It is clear, that the energy barriers follow the order $\theta > \Phi > \alpha$ for $Sc_3C_2@C_{80}$, $Sc_3N@C_{80}$ and $Er_3N@C_{80}$ EMFs. Similarly, the energy barriers follow the order $Sc_3C_2@C_{80}$ > $Sc_3N@C_{80}$ > $Er_3N@C_{80}$, the metallic moiety is rotated in respect to a fixed fullerene cage. For this rotational mode, rotations about the β and Φ axes are equivalent, so in the gas phase, rotations about 3 distinct axes are investigated. In the presence of the gold substrate, I consider three modes of rotation. Rotation of the metallic moiety in the presence of a fixed cage, and rotation of both the metallic moiety and cage, such that their relative orientation is fixed. This means that in total, on a substrate, 12 distinct cases are considered (4 axes x 3 modes of rotation). The energy barriers to rotation about the above axes were computed, to obtain the preferred angles of rotation, which minimise the total energy. Thus, the energy barriers to rotation follow the order $\Delta E(\theta) > \Delta E(\Phi) > \Delta E(\alpha) > \Delta E(\beta)$. This ordering illustrates a rather intuitive structure-function relation, because it is correlated with the standard deviations σ, this shows that large variations in the distance between the metal atom and the substrate lead to large variations in the binding energy and larger energy barriers to rotation, whereas the negligible variations in the distance associated with the α and β axes lead to much smaller energy barriers. As shown in figure 4.21 these results show that Sc_3C_2 possesses the highest barrier.

All the studied parameters in this chapter have a significant effect on the electric and thermoelectric properties of the endohedral metallofullerenes and fullerene as I will show in the next chapter.

Bibliography

1. Kroto, H. W., Heath, J. R., O'Brien, S. C., Curl, R. F., and Smalley, R. E. (1985). C 60: buckminsterfullerene. *nature*, *318*(6042), 162-163.
2. Liang, Y., and Yu, L. (2010). A new class of semiconducting polymers for bulk heterojunction solar cells with exceptionally high performance. *Accounts of chemical research*, *43*(9), 1227-1236.
3. Lu, X., Akasaka, T., and Nagase, S. (2011). Chemistry of endohedral metallofullerenes: the role of metals. *Chemical Communications*, *47*(21), 5942-5957.
4. He, Y., and Li, Y. (2011). Fullerene derivative acceptors for high performance polymer solar cells. *Physical chemistry chemical physics*, *13*(6), 1970-1983.
5. D'Souza, F., Chitta, R., Sandanayaka, A. S., Subbaiyan, N. K., D'Souza, L., Araki, Y., and Ito, O. (2007). Supramolecular Carbon Nanotube-Fullerene Donor− Acceptor Hybrids for Photoinduced Electron Transfer. *Journal of the American Chemical Society*, *129*(51), 15865-15871.
6. Castro, E., Garcia, A. H., Zavala, G., and Echegoyen, L. (2017). Fullerenes in biology and medicine. *Journal of Materials Chemistry B*, *5*(32), 6523-6535.
7. Soler, J. M., Artacho, E., Gale, J. D., García, A., Junquera, J., Ordejón, P., and Sánchez-Portal, D. (2002). The SIESTA method for ab initio order-N materials simulation. *Journal of Physics: Condensed Matter*, *14*(11), 2745.
8. Herrer, I. L., Ismael, A. K., Milan, D. C., Vezzoli, A., Martín, S., Gonzalez-Orive, A., Grace, I., Lambert, C., Serrano, J. L., Nichols, R. J., and Cea, P. (2018). Unconventional single-molecule conductance behavior for a new heterocyclic anchoring group: pyrazolyl. *The journal of physical chemistry letters*, *9*(18), 5364-5372.

9. Ismael, A. K., Wang, K., Vezzoli, A., Al-Khaykanee, M. K., Gallagher, H. E., Grace, I. M., Lambert, C. J., Xu, B., Nichols, R. J., and Higgins, S. J. (2017). Side-Group-Mediated Mechanical Conductance Switching in Molecular Junctions. *Angewandte Chemie International Edition*, *56*(48), 15378-15382.
10. Markin, A., Ismael, A. K., Davidson, R. J., Milan, D. C., Nichols, R. J., Higgins, S. J., Lambert, C. J., Hsu, Y. T., Yufit, D. S., and Beeby, A. (2020). Conductance Behavior of Tetraphenyl-Aza-BODIPYs. *The Journal of Physical Chemistry C*, *124*(12), 6479-6485.
11. Fonseca Guerra, C., Handgraaf, J. W., Baerends, E. J., and Bickelhaupt, F. M. (2004). Voronoi deformation density (VDD) charges: Assessment of the Mulliken, Bader, Hirshfeld, Weinhold, and VDD methods for charge analysis. *Journal of computational chemistry*, *25*(2), 189-210.
12. Hirshfeld, F. L. (1977). Bonded-atom fragments for describing molecular charge densities. *Theoretica chimica acta*, *44*(2), 129-138.
13. Rincón-García, L., Ismael, A. K., Evangeli, C., Grace, I., Rubio-Bollinger, G., Porfyrakis, K., Agraït, N., and Lambert, C. J. (2016). Molecular design and control of fullerene-based bi-thermoelectric materials. *Nature materials*, *15*(3), 289-293.
14. Shusterman, A. J., and Hoistad, L. M. (2001). Teaching Chemistry with Electron Density Models. 2. Can Atomic Charges Adequately Explain Electrostatic Potential Maps. *The Chemical Educator*, *6*(1), 36-40.
15. Clough, S. A., Beers, Y., Klein, G. P., and Rothman, L. S. (1973). Dipole moment of water from Stark measurements of H2O, HDO, and D2O. *The Journal of Chemical Physics*, *59*(5), 2254-2259.
16. Skinner, S. J., and Kilner, J. A. (2003). Oxygen ion conductors. *Materials Today*, *6*(3), 30-37.
17. Hands, I. D., Dunn, J. L., and Bates, C. A. (2010). Calculation of images of oriented C_{60} molecules using molecular orbital theory. *Physical Review B*, *81*(20), 205440.

Chapter 5

Exploiting fluctuations in the search for high-thermoelectric-performance molecular junctions

This work was a joint collaboration between the group of Prof. Nicolas Agrait (Departamento de Física de la Materia Condensada, Universidad Autónoma de Madrid, Spain), who conducted the experiments and the group of Prof. Kyriakos Porfyrakis (Department of Materials, University of Oxford), who synthesised the molecules.

5.1 Motivation

For the purpose of creating single-molecule junctions, which can convert a temperature difference $\Delta\mathcal{T}$ into a voltage ΔV via the Seebeck effect, it is of interest to screen molecules for their potential to deliver high values of the Seebeck coefficient $S = -\Delta V/\Delta\mathcal{T}$. When single molecules are placed between two electrodes to form single-molecule junctions, it is standard practice to make thousands of measurements of their Seebeck coefficients, because their values fluctuate due to random binding configurations of the molecule within the junction and variations in the electrode Fermi energy E_F relative to energies of frontier orbitals. Usually, one is interested in the most-probable values of S, which are obtained from the peaks in their histograms. Here we demonstrate that additional insight into molecular-scale structure-function relationships can be obtained by examining the widths and extreme values of such histograms. Using a combination of experimental scanning-tunnelling-microscopy-based transport measurements and density-functional-theory-based transport calculations, we study the electrical conductance and Seebeck coefficient of three endohedral metallofullerenes (EMFs)

$Sc_3N@C_{80}$, $Sc_3C_2@C_{80}$, and $Er_3N@C_{80}$, which based on their structures, are selected to exhibit different degrees of charge inhomogeneity and geometrical disorder within a junction. When placed on a flat gold surface, the distance d between the top-most plane of the Au substrate and the closest metallic atom inside the EMFs fluctuates due to rotations of the encapsulated moiety on the surface and the degree of variation is characterised by the associated standard deviation σ, which is a purely geometric quantity. Similarly, the degree of charge inhomogeneity on the fullerene cage can be characterised by a standard deviation σ_q associated with charge inhomogeneity. Here we report an interesting structure-function relationship by demonstrating that standard deviations in the Seebeck coefficient σ_S of EMF-based junctions are correlated with the geometric quantity σ and the charge inhomogeneity σ_q. We benchmark these molecules against C_{60} and demonstrate that both σ_q, σ_S are the largest for $Sc_3C_2@C_{80,}$ both are the smallest for C_{60} and for the other EMFs, they follow the order $Sc_3C_2@C_{80}$ >$Sc_3N@C_{80}$ > $Er_3N@C_{80}$ > C_{60}. A large value of σ_S is a sign that a molecule can exhibit a wide range of Seebeck coefficients and if orientations corresponding to high values can be selected and controlled, then the molecule has the potential to exhibit high-performance thermoelectricity. For the EMFs studied here, large values of σ_S are associated with distributions of Seebeck coefficients containing both positive and negative signs, which reveals that all these EMFs are bi-thermoelectric materials.

5.2 Introduction

Recently there has been much progress in understanding the thermoelectrical properties of single-molecule junctions [1-4]. stimulated in part by reports of high Seebeck coefficients of order 161 μVK^{-1} [5] In this regard, thermoelectricity in fullerenes and nanotubes has led to the observation that the sign of the Seebeck coefficient in fullerenes and nanotubes can be switched by pressure, strain and inter-molecular interactions [6-10].

During recent years, the search for non-toxic and easily processable thermoelectric materials has led several groups to explore the potential of molecular-scale devices for converting waste heat into electricity [11-48]. This is achieved via the Seebeck effect, which converts a temperature difference $\Delta \mathcal{T}$

into a voltage $\Delta V = -S\Delta\mathcal{T}$, where the constant of proportionality is the Seebeck coefficient S. Measured values of S are currently too low to create an economically viable technology and therefore there is a need to develop strategies for rapidly assessing the ability of a given molecule to deliver high values of S. In the 1980s, studies of sample-to-sample variations in electrical conductance G of mesoscopic, phase-coherent solids led to remarkable discoveries such as universal conductance fluctuations (UCFs), in which the standard deviation σ_G in the conductance is $\sigma_G = aG_0$, where $G_0 = \frac{2e^2}{h} \approx 77$ μS is the quantum of conductance [49-51]. In this expression, a is a number of order unity, which is independent of the average value of G, and depends only on the presence of an applied magnetic field or spin-orbit scattering. Since that time, the field of single-molecule electronics has been established, in which the electrical conductor is a single molecule located between electrodes separated by a few nanometres. However, even though many experiments have confirmed that transport through single molecules is phase coherent [52-61], even at room temperature, information contained in fluctuations has been largely ignored. Here, our aim is to demonstrate that studies of fluctuations in single-molecule transport properties are of particular interest in the search for molecules with high thermoelectrical performance, because rare examples of junctions exhibiting extreme values of Seebeck coefficients are a proof of principle that such junctions can exhibit high thermopowers.

To demonstrate that fluctuations can be used to search for molecules with potential for high thermoelectric performance, I report a combined experimental and theoretical study of a family of endohedral metallofullerenes (EMFs), specifically chosen to exhibit large fluctuations. EMFs are chosen because they can form single-molecule junctions without the need for anchor groups, which in the literature, are often used to bind molecules to electrodes. Such anchor groups would restrict the number of binding configurations within a junction and reduce fluctuations, whereas in this study, I would like to explore the full phase space of molecular configurations within a junction.

EMFs represent a fascinating class of nanomaterials, whose optical [62], electrochemical [63] or magnetic [64] properties are controlled by the type of metal atom(s) encapsulated by the fullerene cage. For example, erbium containing EMFs possess a characteristic 1520 nm emission associated with the erbium ion, which is of fundamental importance for telecommunication applications and the fabrication

of erbium doped amplifiers [65]. Moreover, there is a broad spectrum of scandium-containing metallofullerenes, including the paramagnetic $Sc@C_{82}$ and $Sc_3C_2@C_{80}$, which can find applications as spin probes and quantum information processing components [66]. The latter exhibits a unique diamond shaped EPR, with respect to the three equivalent scandium atoms (Appendix B see Figure 2). For the purpose of probing fluctuations in transport properties, these molecules are attractive, because they not only bind to electrodes with a range of different orientations, but also by making different choices for the encapsulated moiety, they can possess highly inhomogeneous charge distributions (for example as in the case of $Sc_3C_2@C_{80}$) or possess a relatively homogeneous charge distribution (as for C_{60}). Therefore, a study of their transport properties is expected to reveal how charge distributions and geometry are correlated with fluctuations in their Seebeck coefficients and their ability to exhibit high values of S.

To investigate correlations between Seebeck coefficient, geometry and charge inhomogeneity, our aim is to compare transport properties of $Sc_3N@C_{80}$ and C_{60} [21], with those of two other trimetallic EMFs, namely, the paramagnetic $Sc_3C_2@C_{80}$ (Appendix B see Figure 2) and a rare-earth-based EMF, $Er_3N@C_{80}$. Like $Sc_3N@C_{80}$, these EMFs are formed with the fullerene cage I_h-C_{80}, composed of 80 C atoms organised in an icosahedral structure (I_h symmetry also shared by C_{60}) (see Figure 4.1) [65-68] and their cages possess sizeable charge inhomogeneity. My main result is that the standard deviations of Seebeck coefficients of these four molecules are strongly correlated with standard deviations in the charge distributions on their fullerene cages, thereby establishing a structure-function relationship between Seebeck fluctuations and charge inhomogeneity. Furthermore, molecules with high charge inhomogeneity exhibit rare examples of high thermopower, which means that if these rare junction configurations could be isolated and controlled, then such molecules have the potential to deliver high-performance thermoelectricity.

5.3 Transmission coefficient $T(E)$

In this section, I employ the GOLLUM code to determine the electrical transport properties of endohedral metallofullerenes EMFs and C_{60} from SIESTA's divergence evolved mean-field DFT Hamiltonian, for more detail see chapter 2 section 2.6. As a mention in chapter 4 due of the presence of

f-electrons, the transmission coefficient $T(E)$ and Seebeck coefficients S of $Er_3N@C_{80}$ are not calculated (less reliable). Gollum code is based on stationary transport theory which is used to evaluate transmission coefficients $T(E)$ for electrons at energy E. The Landauer formula calculates the zero-bias electrical conductance G

$$G = G_0 \int_{-\infty}^{\infty} dE\, T(E) \left(\frac{\partial f(E,T)}{\partial E} \right) \tag{5.1}$$

where $G_0 = \left(\frac{2e^2}{h}\right)$ is the quantum of conductance and $f(E,T)$ is the Fermi distribution function defined as $f(E,T) = \left[e^{\frac{(E-E_F)}{k_B T}} + 1 \right]^{-1}$ with k_B is Boltzmann constant.

Figure 5.1, shows an example of transmission coefficient curve as a function energy for C_{60} cage. The physical meaning of the transmission coefficient is the probability of an electron to pass form the left electrode to the right electrode through the molecule at a certain energy.

Figure 5.1, also illustrates the HOMO and LUMO gap with a smooth curve and this is due to the fact that C_{60} is an empty cage. However, the case is different when there is an encapsulated moiety inside the cage to form endohedral metallofullerenes (EMFs), such as $Er_3N@C_{80}$ and $Sc_3N@C_{80}$. The encapsulated moiety causes an extra feature in the transmission curve, for instance resonances as shown in Figure 5.2. Furthermore, if the encapsulated moiety is metallic in whole or contains metallic atoms then a spin polarisation calculation is required. I provide more detail about the spin polarisation in the next section.

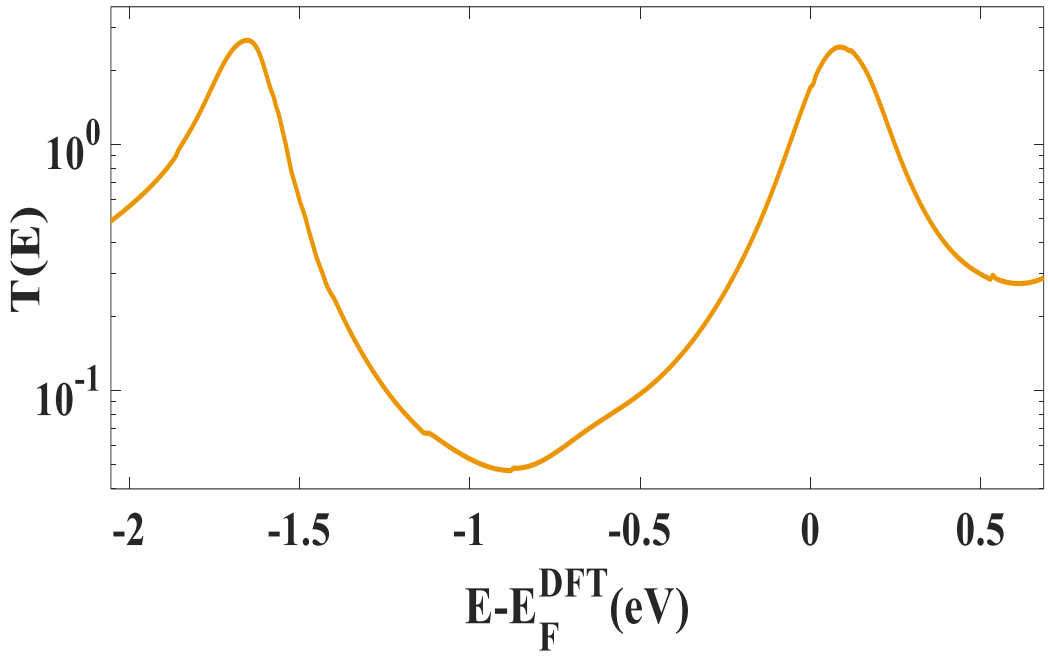

Figure 5.1. An example of transmission coefficient curve of C_{60} cage. A smooth transmission curve versus energy with HOMO and LUMO resonances.

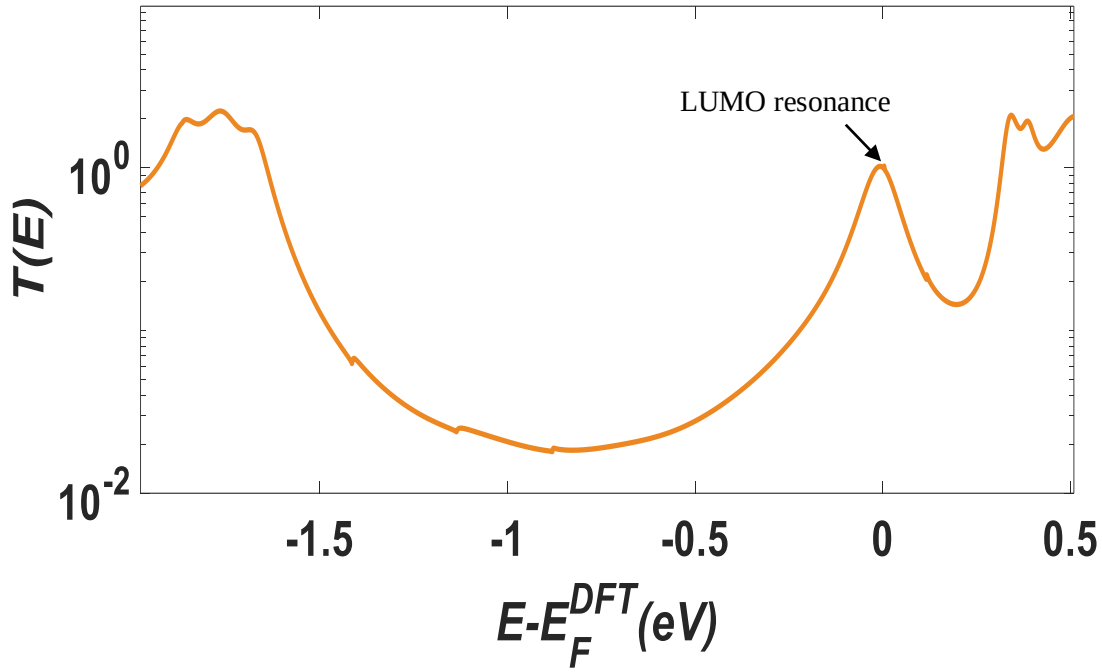

Figure 5.2. An example of transmission coefficient curve of $Sc_3N@C_{80}$ EMF. The transmission curve possesses an extra resonance close to LUMO, due to the encapsulated moiety Sc_3N inside the cage.

5.4 Spin polarisation

An active topic of nanotechnology research is concerned with the use of electron spin for storage and processing. Some recent spintronic devices are composed of inorganic materials, and the use of organic materials in spintronics is already a major topic in science and engineering fields [70,71]. Gohler *et al*. reported spin-selective electron transmission through double-stranded DNA (dsDNA) monolayers at room temperature [72]. They reported that spin polarisation goes up with dsDNA length and showed efficient spin filtered [73]. Charge transfer was investigated using double-stranded DNA oligomers linked to two electrodes by Xie *et al* [74]. They realized that dsDNA molecules will function as very effective spin filters. The Green's function approach was utilised in a theoretical physics research to evaluate spin polarisation and spin-dependent electron conductance on the helical symmetry, length, and environment-induced dephasing factors of dsDNA. Next section, I will explore spin-dependent transport calculations for different rotation angels $\theta, \Phi, \alpha \; and \; \beta$ of $Sc_3C_2@C_{80}$, $Sc_3N@C_{80}$ respectively.

As it mentioned above, since the studied EMFs have metallic moieties with unpaired spins, taking into account spin polarisation is essential, otherwise the simulations would be incorrect. In chapter 4, I explored number of parameters that have an effect on the electronic and thermoelectric properties. In section 4.5, I discussed the effect of axes and rotation, where I considered 4 distinct axes of rotation (see Figure 4.6), including θ, Φ, α and β.

5.4.1 Spin-dependent transport calculations for different rotation angles (θ) about a horizontal axis

Here, I am going to investigate the effect of the 4 rotation axes θ, Φ, α and β, on the transmission coefficient and Seebeck coefficient for both $Sc_3C_2@C_{80}$ and $Sc_3N@C_{80}$ EMFs. I will first begin with an example that illustrates the effect of the spin polarisation (spin-up and spin-down), how I apply this effect in my simulations.

Figure 5.3 shows the definition of the orientation angle of the $Sc_3C_2@C_{80}$ molecule from θ = 0º to 90º. Figure 5.4 shows an example of the spin-dependent transmission coefficients *T(E)* for the optimum geometry (60º) shown in Figure 5.3. These reveal that the calculated transmission for spin-up ($T_{up}(E)$) and spin-down ($T_{down}(E)$) show that the resonance is split as expected due to the charge transfer from the metallic moiety to the cage, which positions the resonance close to the Fermi energy. The total transmission is then given by $\frac{T_{up}(E)+T_{down}(E)}{2}$ as shown in Figure 5.4.

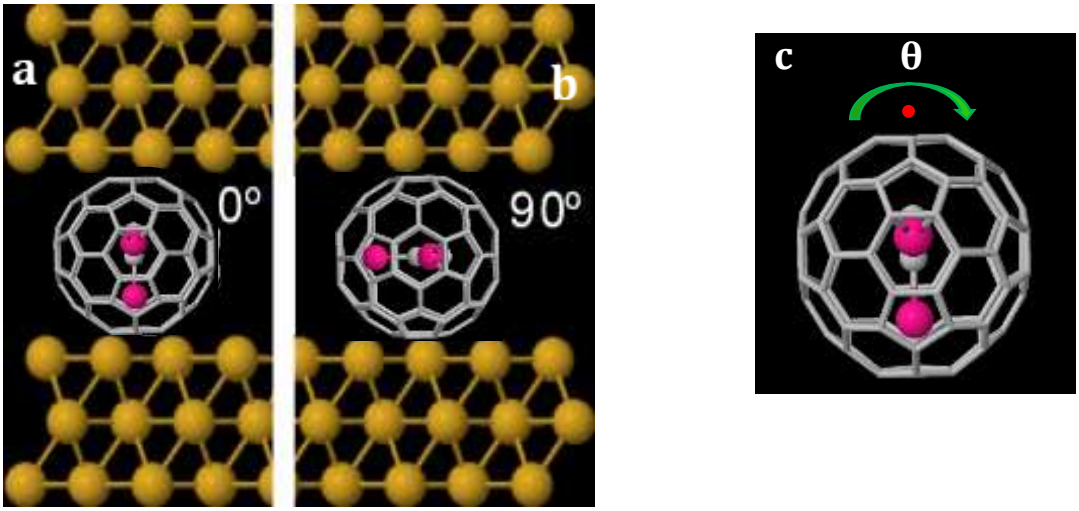

Figure 5.3. $Sc_3C_2@C_{80}$ EMF between gold surfaces. The orientation of the $Sc_3C_2@C_{80}$ molecule with respect to the gold leads corresponds to the defined angle (**a**) θ = 0°, (**b**) θ = 90°. (**a** and **b**): a view in which the rotation axis is perpendicular to the plane of the paper, **(c):** The horizontal rotation axis θ.

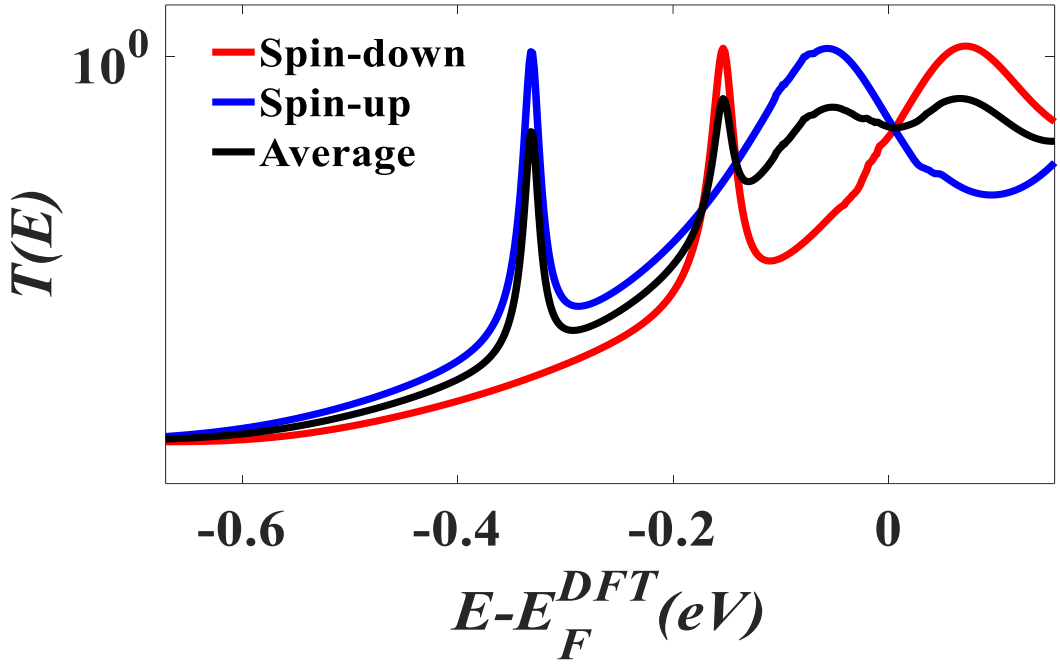

Figure 5.4. Spin-polarised transmission coefficients $T_{up}(E)$, $T_{down}(E)$ and $T(E) = \frac{T_{up}(E)+T_{down}(E)}{2}$, for the binding configuration of 60° orientation θ of $Sc_3C_2@C_{80}$ and z = 2.5 Å. The three curves represent the spin-up, spin-down and the average of them: blue, red and black curves, respectively.

Since, the extra resonance due to the metallic moiety is closer to the LUMO resonance (see Figure 5.4), and for clarity, only the effective area (the extra resonance and LUMO resonance, black-dashed box) is going to be shown in the coming Figures.

Figure 5.5 shows the average transmission coefficients for different orientations of $Sc_3C_2@C_{80}$ (see Figure 5.3). Similarly, Figure 5.6 shows the average transmission coefficients for 60 different orientations of $Sc_3N@C_{80}$. By comparing Figures 5.5 and 5.6, one can notice the fluctuations in the $Sc_3C_2@C_{80}$ transmission curves are larger than those of the $Sc_3N@C_{80}$ curves. I attribute the difference in the fluctuations of $Sc_3C_2@C_{80}$ and $Sc_3N@C_{80}$ to the shape of the metallic moieties. In other words, the shap of Sc_3N moiety is more symmetric/uniform (see Figure 4.16), than Sc_3C_2 and this is why the fluctuation is smaller in case $Sc_3N@C_{80}$ on this rotation axis (θ).

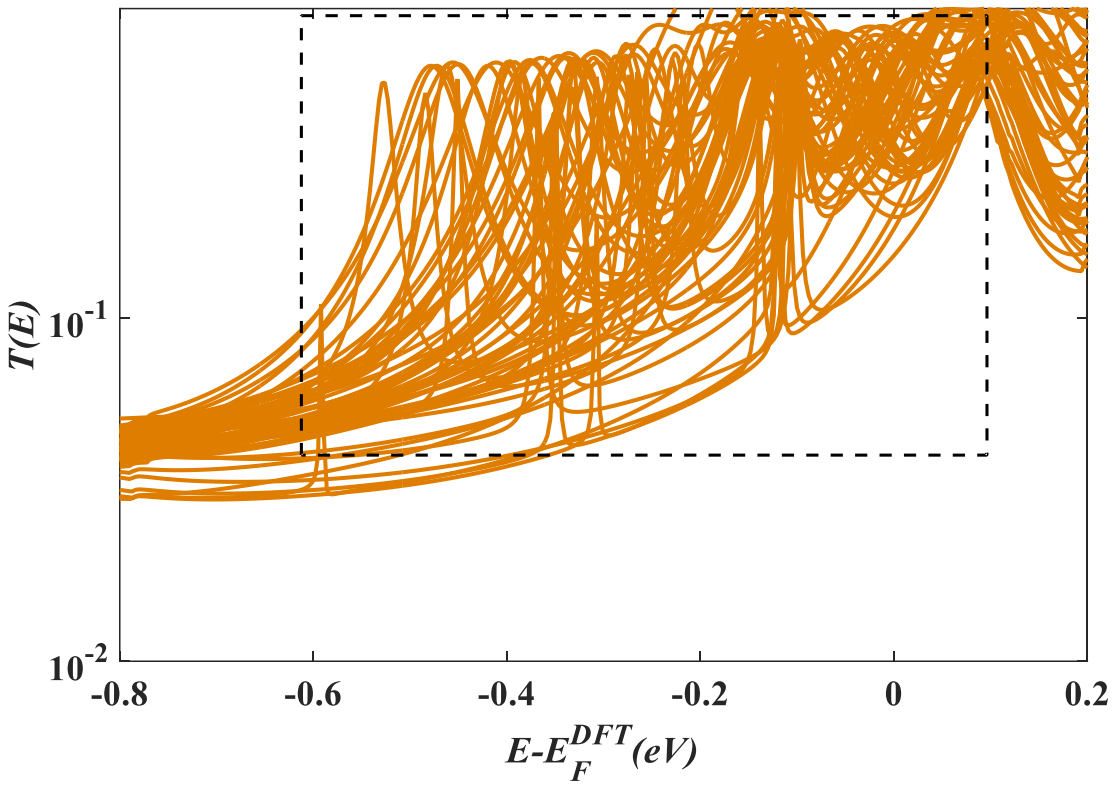

Figure 5.5. Spin-polarised transmission coefficients, $T(E) = \frac{T_{up}(E)+T_{down}(E)}{2}$, for the 60 binding configurations of different orientations θ for $Sc_3C_2@C_{80}$, and z = 2.5 Å.

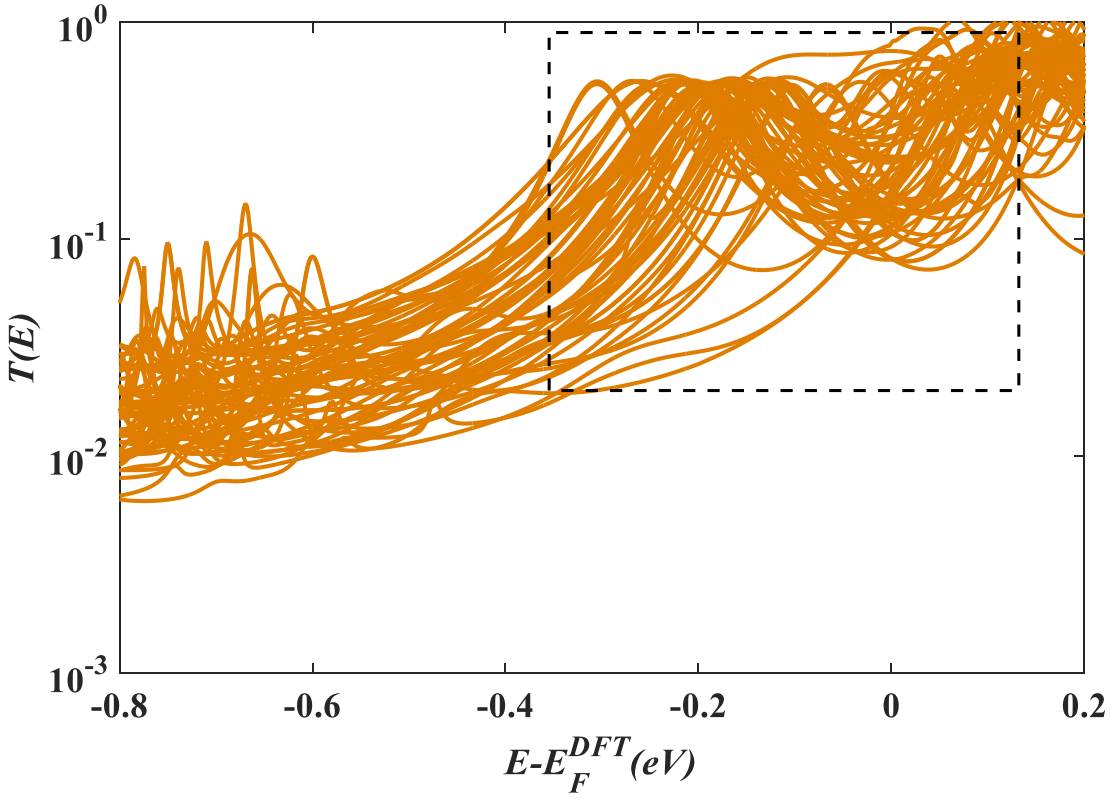

Figure 5.6. Spin-polarised transmission coefficients, $T(E) = \frac{T_{up}(E)+T_{down}(E)}{2}$, for the 60 binding configurations of different orientations θ for $Sc_3N@C_{80}$, and z = 2.5 Å.

5.4.2 Spin-dependent transport calculations for different orientations (Φ) about a horizontal rotation axis

In this section, I repeat the calculations described in section 5.3.1, but using the horizontal rotation axis (Φ), as shown in Figure 5.7. As expected the fluctuations in the transmission coefficients are smaller when the EMF rotates about the Φ axis, because the variation in the distance (see Table 4.4), between the metallic part Sc_3C_2/ Sc_3N and the cage C_{80} is smaller compared to rotation in θ axis as shown in Figures 5.8, 5.9.

The variation in the distance has been discussed thoroughly in chapter (see section 4.6, Figures 4.8, 4.9, 4.10 and Table 4.4). Here, one can easily notice the effect of this parameter on the transmission coefficient.

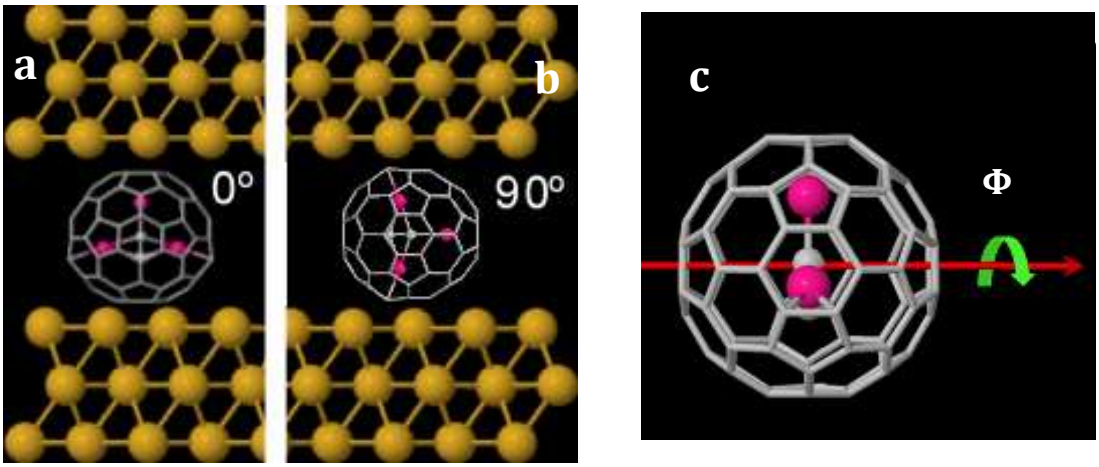

Figure 5.7. $Sc_3C_2@C_{80}$ EMF between gold surfaces. The orientation of the $Sc_3C_2@C_{80}$ molecule with respect to the gold leads corresponds to the defined angle (**a**) θ = 0°, (**b**) θ = 90°. (**a** and **b**): a view in which the rotation axis is perpendicular to the plane of the paper, **(c):** The horizontal rotation axis Φ.

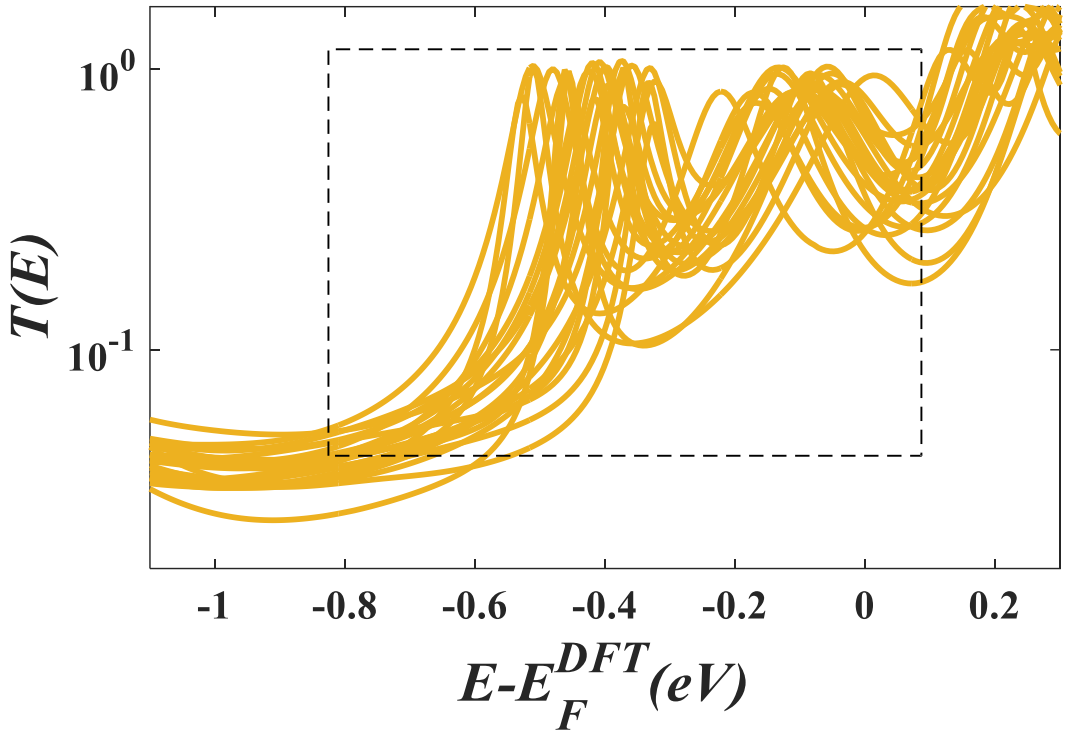

Figure 5.8. Spin-polarised transmission coefficients, $T(E) = \frac{T_{up}(E)+T_{down}(E)}{2}$, for the 60 binding configurations of different orientations Φ of $Sc_3C_2@C_{80}$, and z = 2.5 Å.

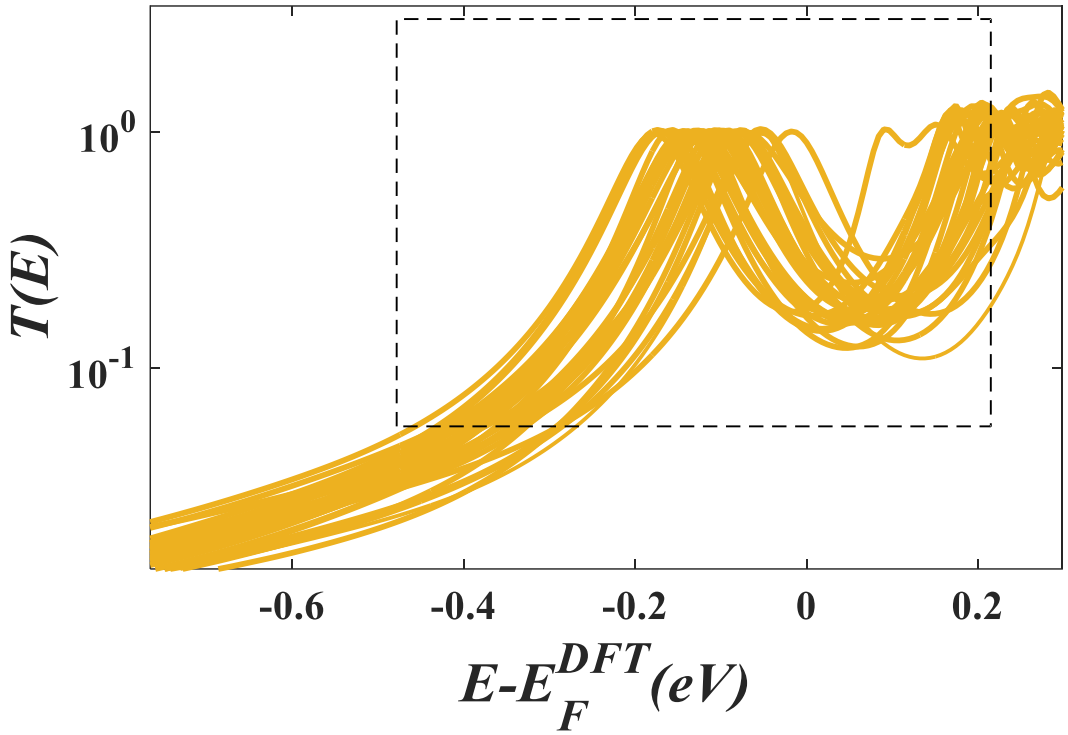

Figure 5.9. Spin-polarised transmission coefficients, $T(E) = \frac{T_{up}(E)+T_{down}(E)}{2}$, for the 60 binding configurations of different orientations Φ of $Sc_3N@C_{80}$, and z = 2.5 Å.

5.4.3. Spin-dependent transport calculations in the vertical rotation axis (α)

In this section, I repeat the calculations described in section 5.3.1, using rotation angles about the vertical rotation axis (α), as shown in Figure 5.10. As expected, compared to the rotations about the θ axis, Figures 5.11 and 5.12 show that the fluctuations in the transmission coefficients are smaller when the EMF rotates about this vertical axis, because the rotation causes a smaller variation in the distance (see Table 4.4, chapter 4), between the metallic part Sc_3C_2/Sc_3N and the cage C_{80}. Since the rotation in this axis (α), has small effect on the transmission coefficient curves, Figures 5.22 and 5.23 show that the Seebeck coefficient *S* does not show strong fluctuations (see section 5.5.3).

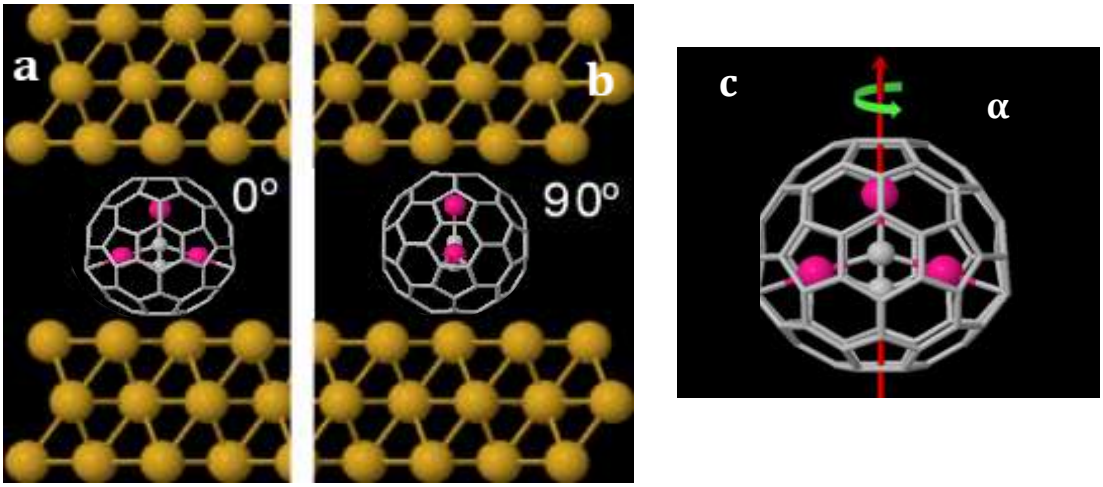

Figure 5.10. $Sc_3C_2@C_{80}$ between gold surfaces. **a-b**: The orientation of the $Sc_3C_2@C_{80}$ molecule with respect to the gold leads. **c**: The vertical rotation axis α.

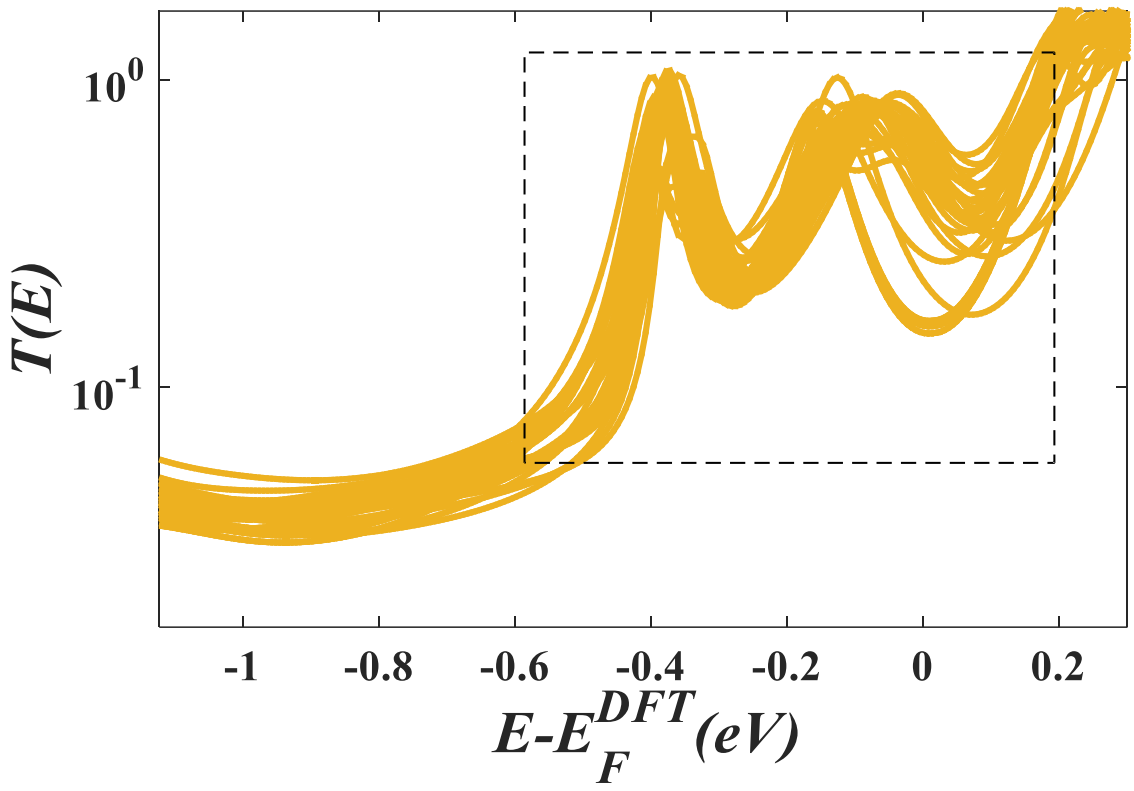

Figure 5.11. Spin-polarised transmission coefficients, $T(E) = \frac{T_{up}(E)+T_{down}(E)}{2}$, for the 60 binding configurations of different orientations α of $Sc_3C_2@C_{80}$, and z = 2.5 Å.

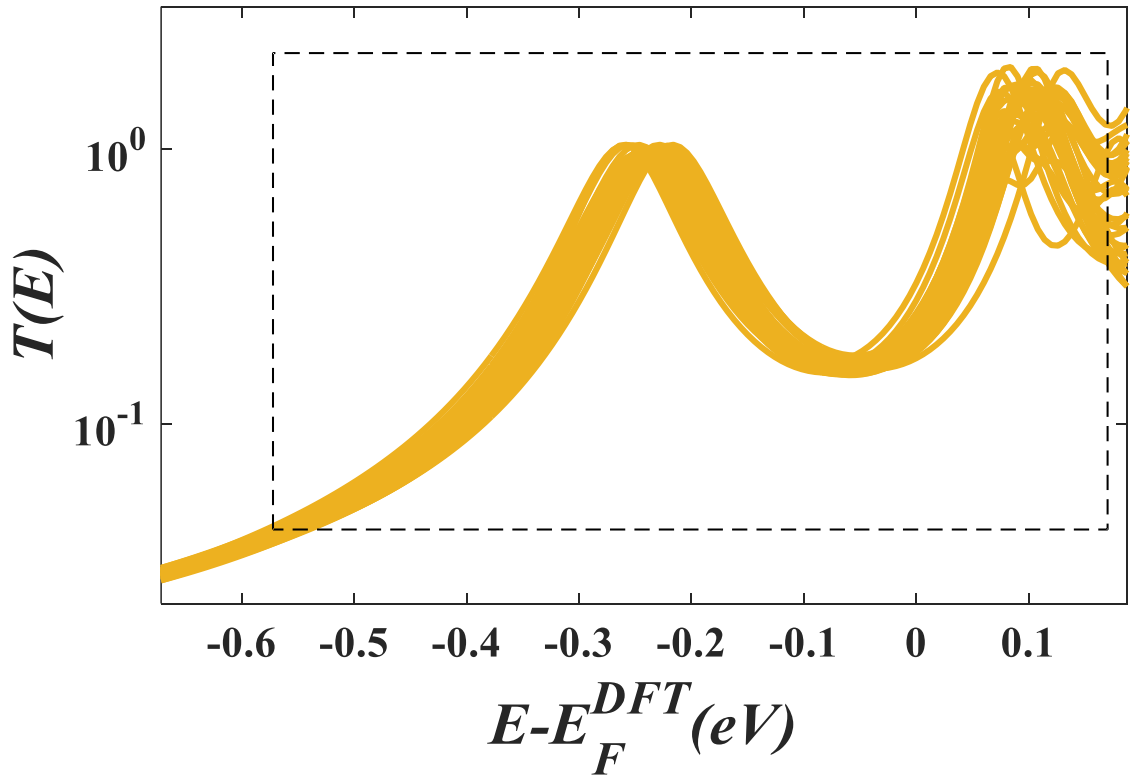

Figure 5.12. Spin-polarised transmission coefficients, $T(E) = \frac{T_{up}(E)+T_{down}(E)}{2}$, for the 60 binding configurations of different orientations α of $Sc_3N@C_{80}$, and z = 2.5 Å.

5.4.4 Spin-dependent transport calculations in the vertical rotation axis (β)

In this section, the same calculations described in section 5.3.1 have been repeated, using the vertical rotation axis (β), as shown in Figure 5.13. As expected, the difference in the transmission coefficients is the smallest when the EMF rotates in vertical axis, and this is due to the fact that the distance between the metallic part Sc_3C_2/Sc_3N and the cage C_{80} is kept the same. Figures 5.14 and 5.15 show small effect in the transmission curves while rotating in vertical axis (β), unlike in the horizontal axes θ and Φ. Since the rotation in this axis (β) has the smallest effect on the transmission coefficient curves one would expect the Seebeck coefficient S to be approximately similar for all rotation angles. I will discuss the effect of rotation axes on S in more detail in section 5.5

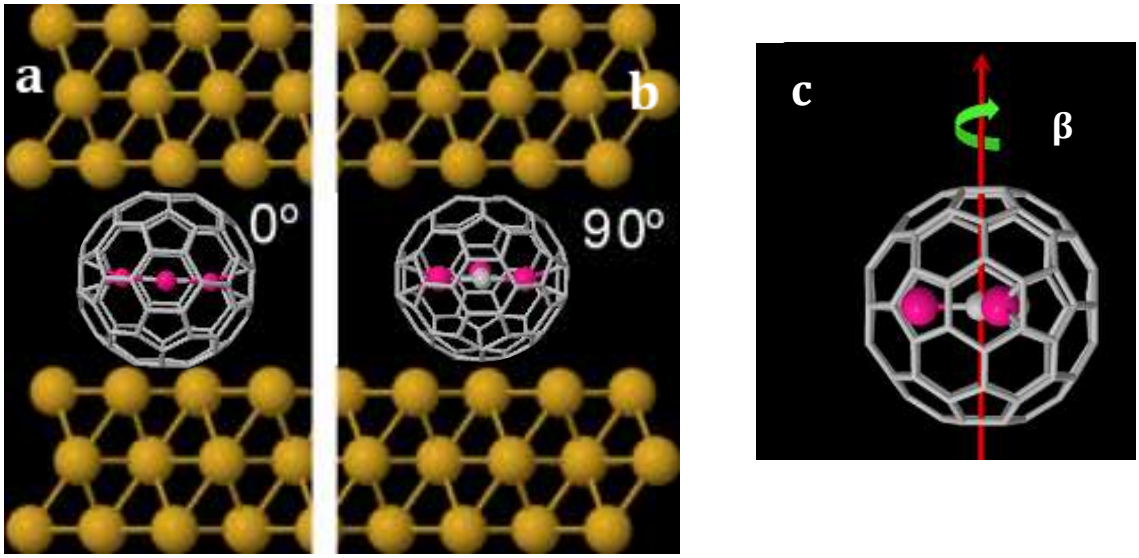

Figure 5.13. $Sc_3C_2@C_{80}$ EMF between gold surfaces. (**a-b**): The orientation of the $Sc_3C_2@C_{80}$ molecule with respect to the gold leads. (**c**): The vertical rotation axis β.

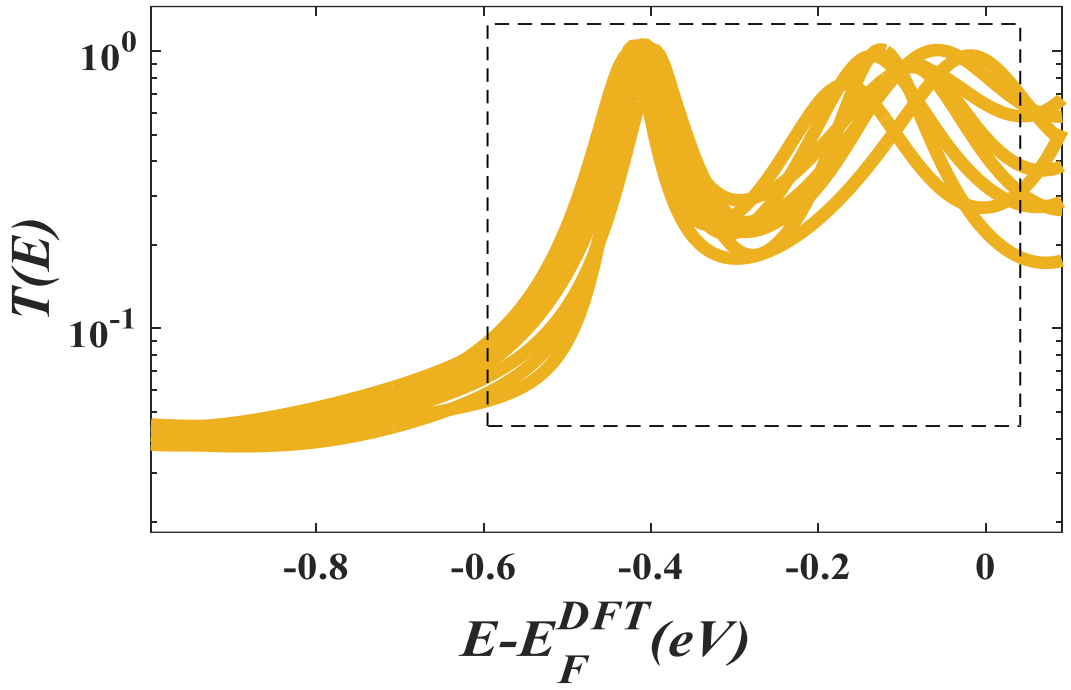

Figure 5.14. Spin-polarised transmission coefficients, $T(E) = \frac{T_{up}(E)+T_{down}(E)}{2}$, for the binding configurations of differnt orientations β of $Sc_3C_2@C_{80}$, and z = 2.5 Å.

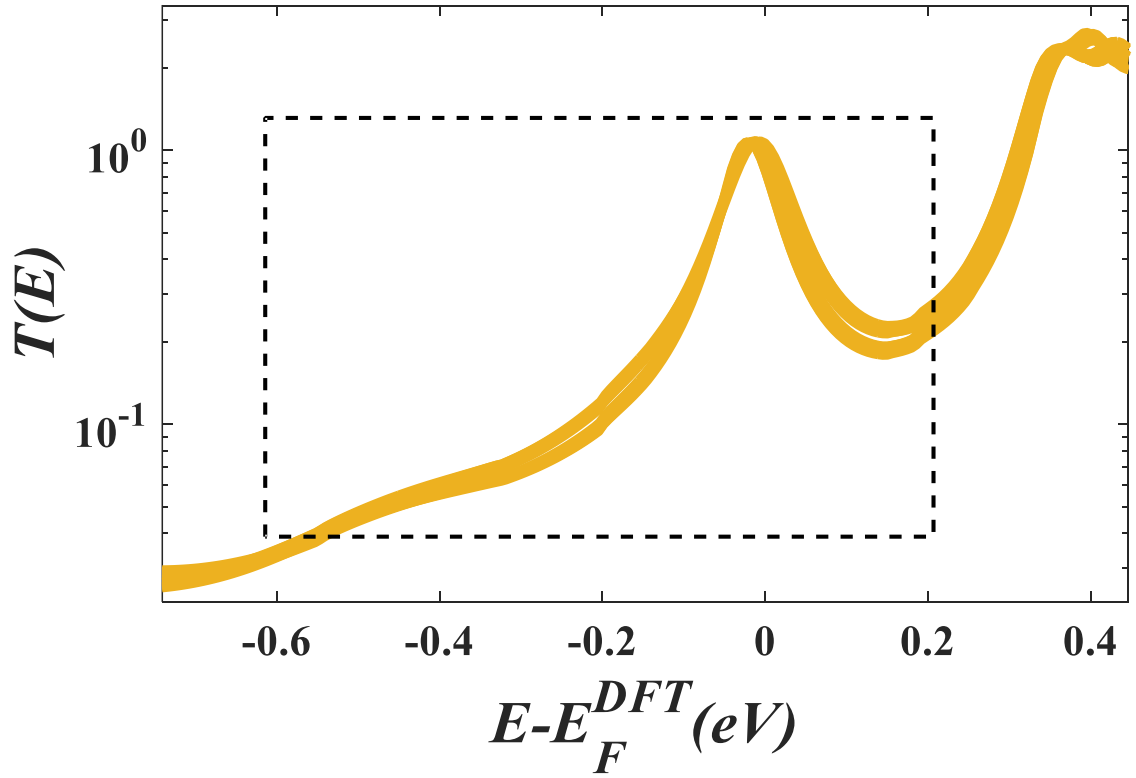

Figure 5.15. Spin-polarised transmission coefficients, $T(E) = \frac{T_{up}(E)+T_{down}(E)}{2}$, for the binding configurations of differnt orientations β of $Sc_3N@C_{80}$, and z = 2.5 Å.

5.4.5. Spin-independent transport calculations of C_{60}

In this section, I repeat the same calculations described in section 5.3.1, however, for an empty cage C_{60}. Since C_{60} has no metallic atoms there is no need for spin-dependent calculations. As expected, the transmission coefficients are almost independent of the rotation angle about a vertical or horizontal axis, because the distance between the carbon atoms of the cage and Au-electrodes are almost unchanged by such rotations. Figure 5.16 shows no significant effect in the transmission curves while rotating about vertical or horizontal axis. Since the rotation has a negligible effect on the transmission coefficient curves one would expect the Seebeck coefficient S to be approximately similar for all rotation angles I will discuss later.

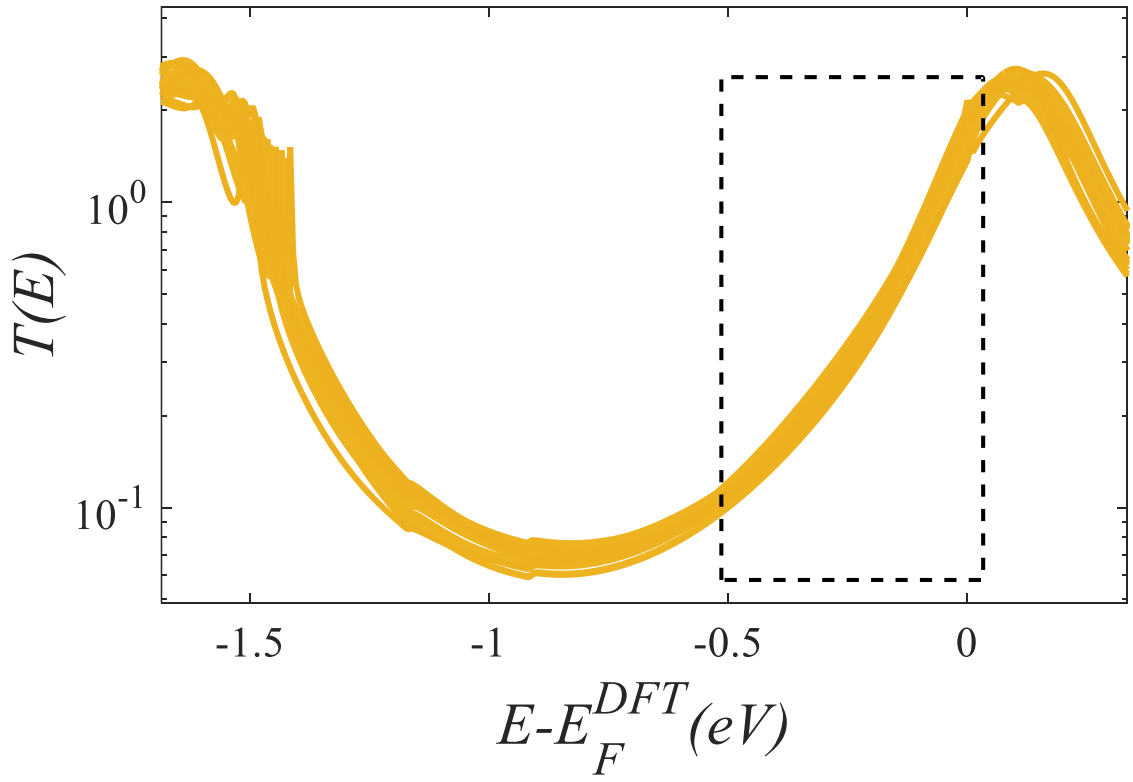

Figure 5.16. Spin-nonepolarised transmission coefficients, $T(E)$, for 60 binding configurations and, in different orientations around θ, Φ, β axes of C_{60}, and z = 2.5 Å. This results agrees with refrence[69].

5.5 Seebeck coefficient *S*

In the above simulations, I have discussed the effect of the rotation in four axes including θ, Φ (horizontal axes), α and β (vertical axes), on the transmission coefficient. I have also discussed the effect of varying the distance between the metallic moiety and the gold substrate on the transmission coefficient for $Sc_3C_2@C_{80}$, $Sc_3N@C_{80}$ EMFs and C_{60}.

In this section, the thermoelectric properties of the EMFs and C_{60} molecules are determined after calculating their electronic transmission coefficients T(E).

To calculate the thermopower of these molecular junctions, it is useful to introduce the non-normalised probability distribution $P(E)$ defined by

$$P(E) = -T(E)\frac{df(E)}{dE} \tag{5.2}$$

where $f(E)$ is the Fermi-Dirac function and $T(E)$ is the transmission coefficients and whose moments L_i are denoted as follows

$$L_i = \int dEP(E)(E - E_F)^i \tag{5.3}$$

where E_F is the Fermi energy. The Seebeck coefficient, S, is then given by

$$S(T) = -\frac{1}{eT}\frac{L_1}{L_0} \tag{5.4}$$

where e is the electronic charge.

and we can rewrite equation 5.3 as follows

$$\mathrm{S^e(T)} = \frac{-1}{\mathrm{eT}}\frac{1}{\mathrm{L^0_{12,\uparrow} + L^0_{12,\downarrow}}}\sum\nolimits_{\sigma}\mathrm{L^1_{12,\sigma}} \tag{5.5}$$

Equation 5.5 describes the linear response regime and is consistent with the Onsager reciprocal relations. This equation is equivalent to the analysis that has been utilised the spin-averaged

transmission coefficient $T(E) = \frac{T_{up}(E)+T_{down}(E)}{2}$. Figure 5.17 illustrates an example of a Seebeck coefficient S versus electron energy of $Sc_3C_2@C_{80}$. I will apply this method to evaluate the Seebeck coefficient S for different rotation axes θ, Φ, α and β of $Sc_3C_2@C_{80}$, $Sc_3N@C_{80}$ and C_{60}, respectively.

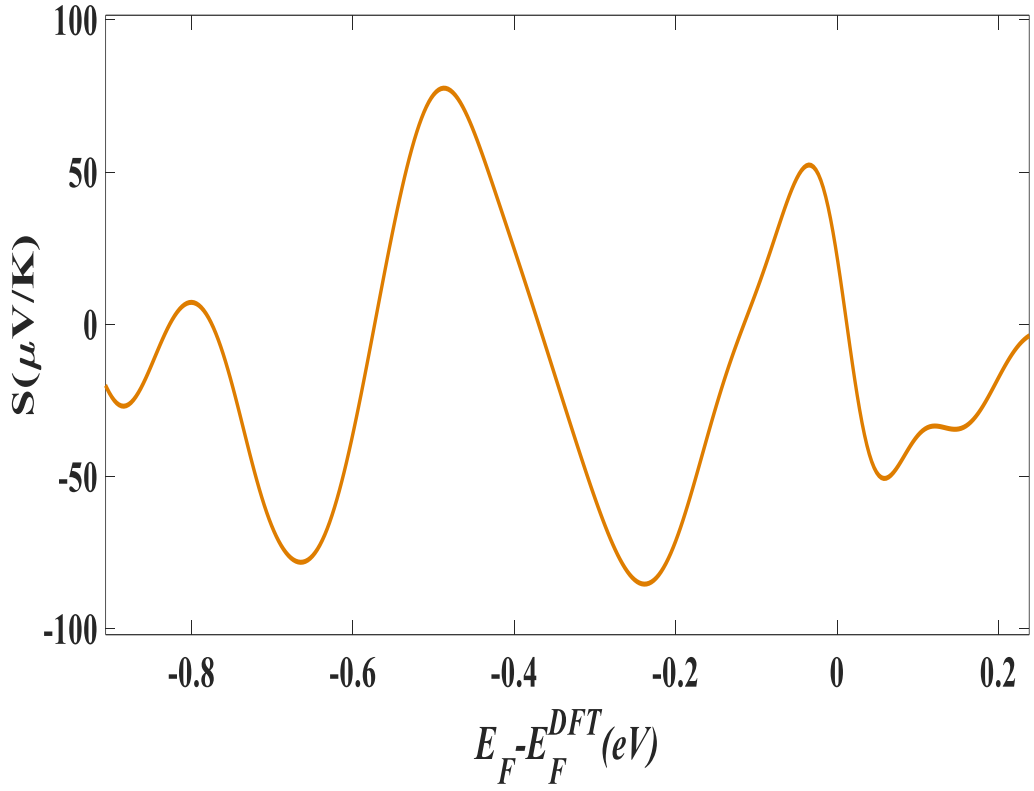

Figure 5.17. An example of Seebeck coefficient S versus electron energy of $Sc_3C_2@C_{80}$ EMF.

5.5.1 Calculated thermopower as a function of orientation in the horizontal rotation axis (θ)

Figures 5.18 and 5.19 show the average Seebeck coefficient S evaluated at room temperature for different orientation angles of θ for $Sc_3C_2@C_{80}$ and $Sc_3N@C_{80}$.

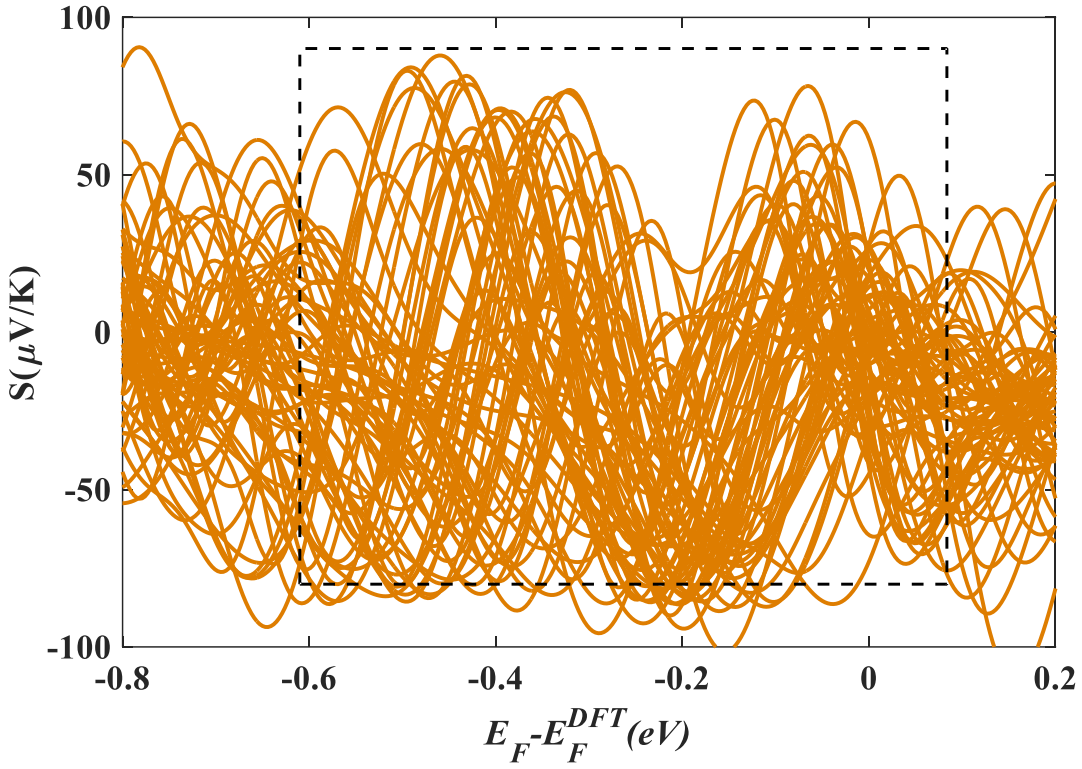

Figure 5.18. Seebeck coefficient *S* as a function of Fermi energy at 60 different orientations angles θ of $Sc_3C_2@C_{80}$, for a tip-substrate distance of 2.5 Å.

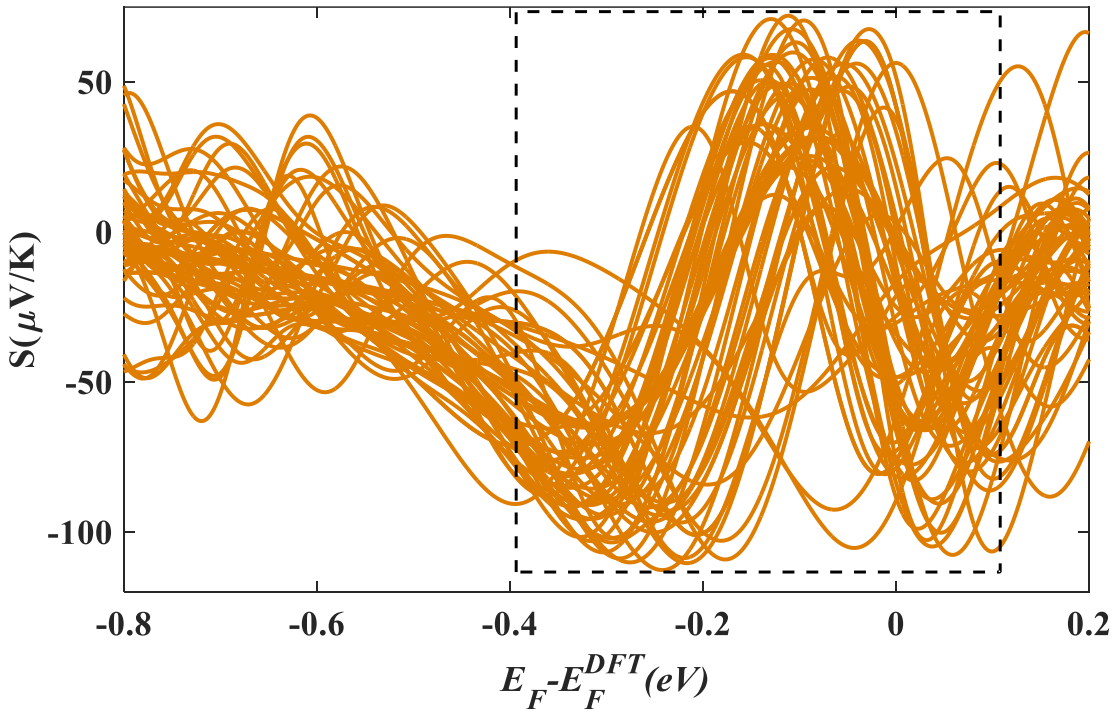

Figure 5.19. Seebeck coefficient *S* as a function of Fermi energy at 60 different orientations angles θ of $Sc_3N@C_{80}$. *S* versus Fermi energy at different orientation angles θ for a tip-substrate distance of 2.5 Å.

5.5.2 Calculated thermopower as a function of orientation in the horizontal rotation axis (Φ)

Figures 5.20 and 5.21 show the average Seebeck coefficient *S* evaluated at room temperature for different orientation angles of Φ for $Sc_3C_2@C_{80}$ and $Sc_3N@C_{80}$.

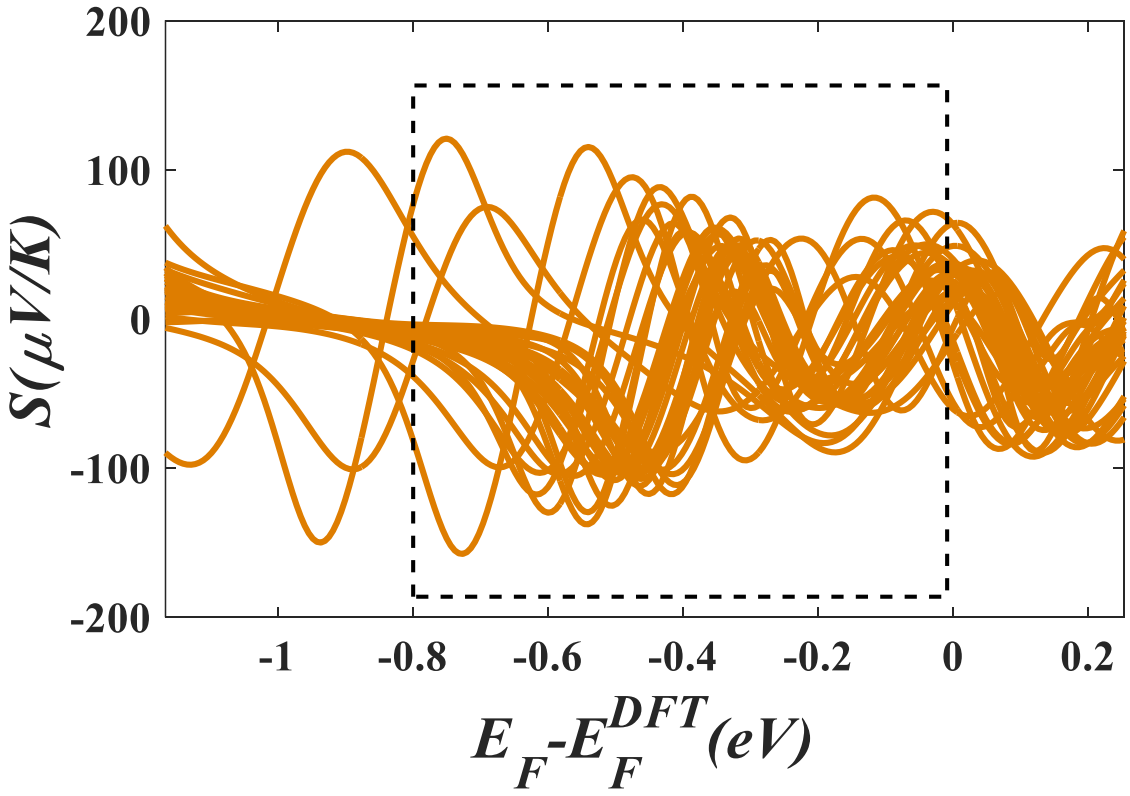

Figure 5.20. Seebeck coefficients *S* as a function of Fermi energy at 60 different orientation angles Φ of $Sc_3C_2@C_{80}$, for a tip-substrate distance of 2.5 Å.

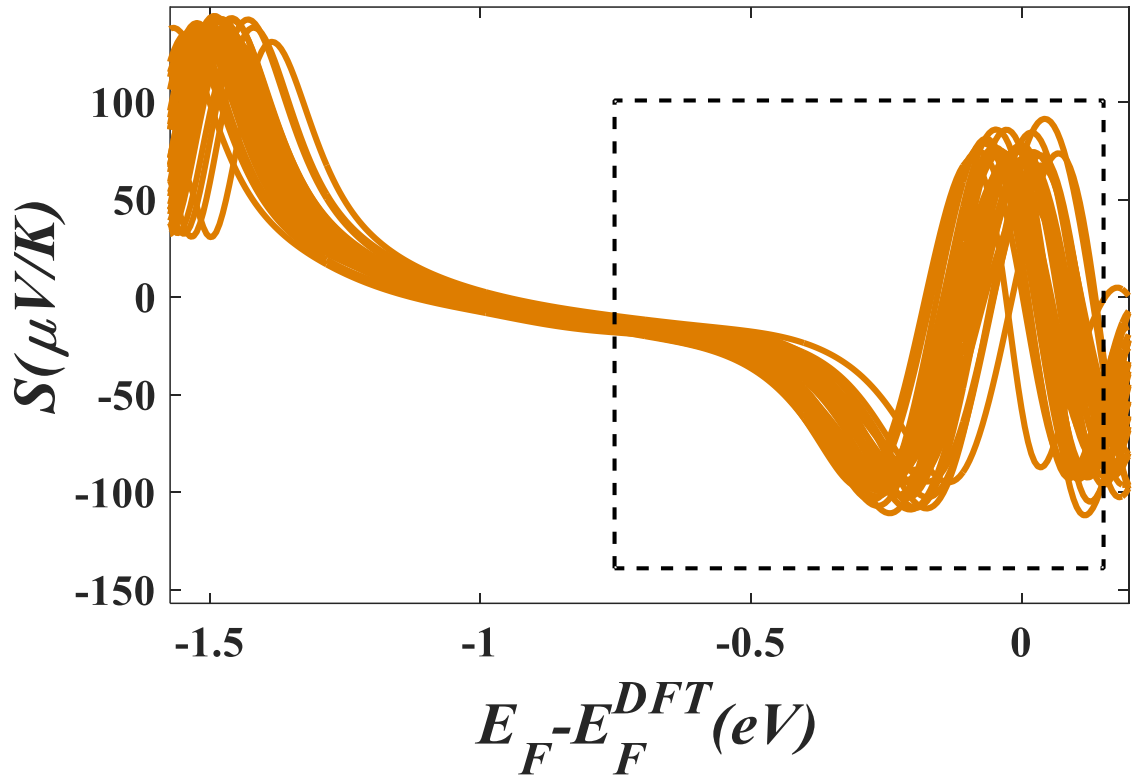

Figure 5.21. Seebeck coefficients *S* as a function of Fermi energy at 60 different orientation angles Φ of $Sc_3N@C_{80}$ for a tip-substrate distance of 2.5 Å.

5.5.3 Calculated thermopower as a function of orientation in the vertical rotation axis (α)

Figures 5.22 and 5.23 show the average Seebeck coefficient *S* evaluated at room temperature for different orientation angles of α for $Sc_3C_2@C_{80}$ and $Sc_3N@C_{80}$.

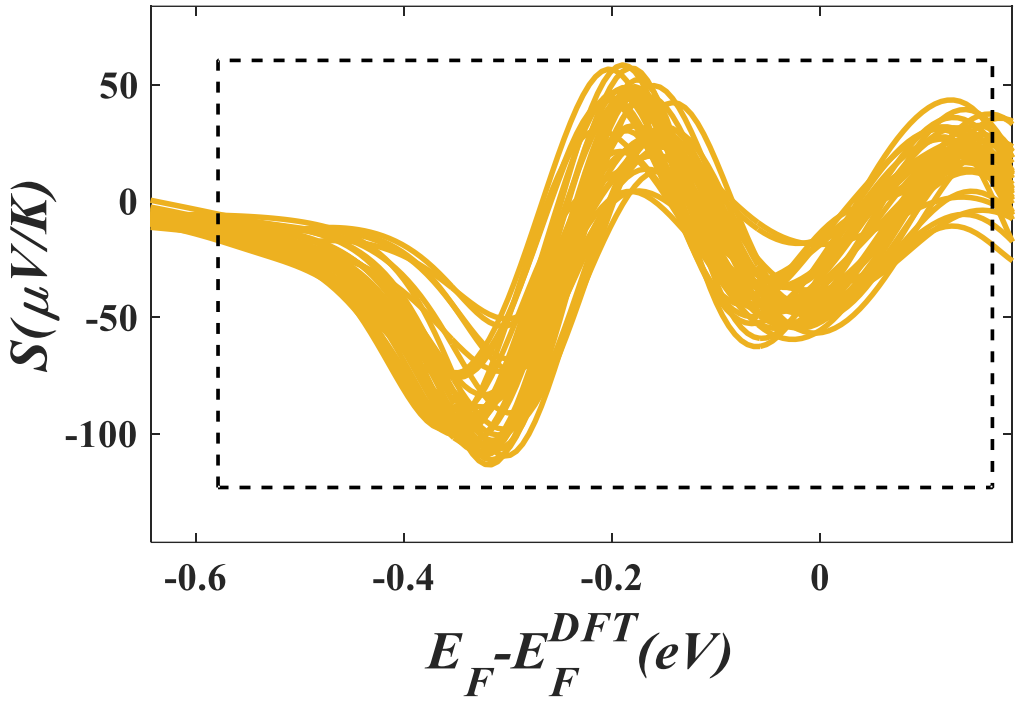

Figure 5.22. Seebeck coefficient *S* as a function of Fermi energy at 60 different orientation angles α of $Sc_3C_2@C_{80}$, for a tip-substrate distance of 2.5 Å.

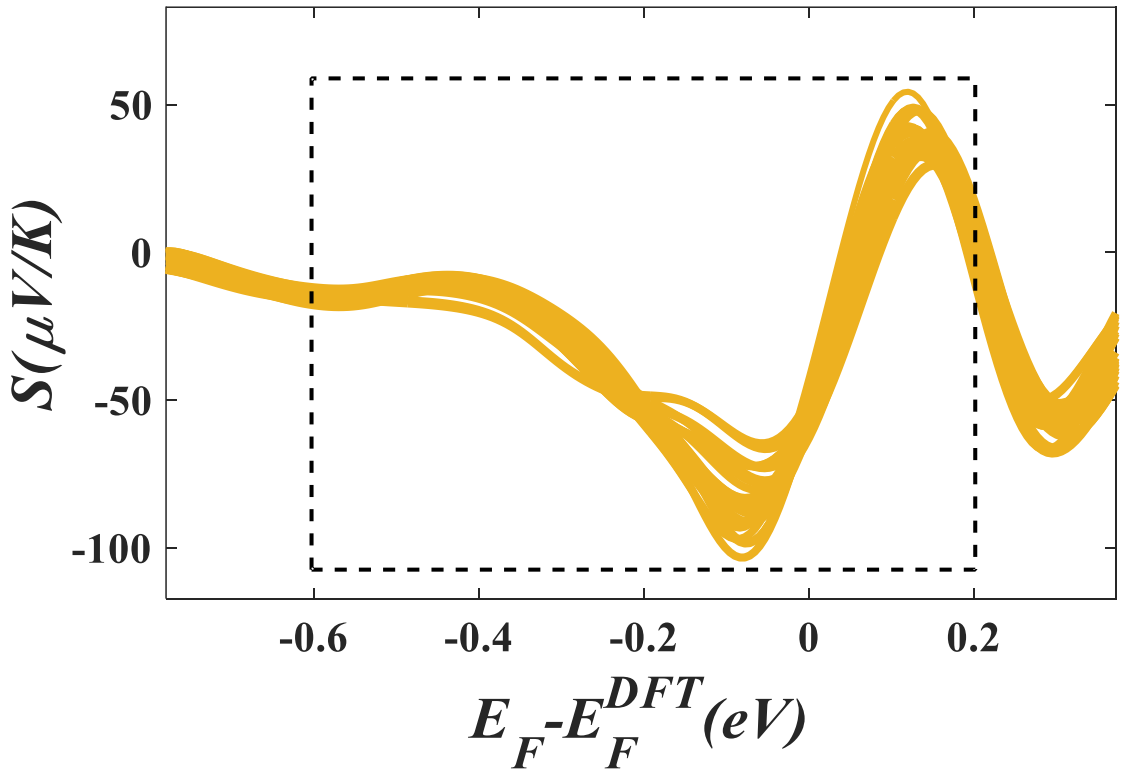

Figure 5.23. Seebeck coefficient S as a function of Fermi energy at 60 different orientation angles α of $Sc_3N@C_{80}$, for a tip-substrate distance of 2.5 Å.

5.5.4 Calculated Seebeck coefficient as a function of orientation in the vertical rotation axis (β)

Figures 5.24 and 5.25 show the average Seebeck coefficient *S* evaluated at room temperature for different orientation angles of β for $Sc_3C_2@C_{80}$ and $Sc_3N@C_{80}$.

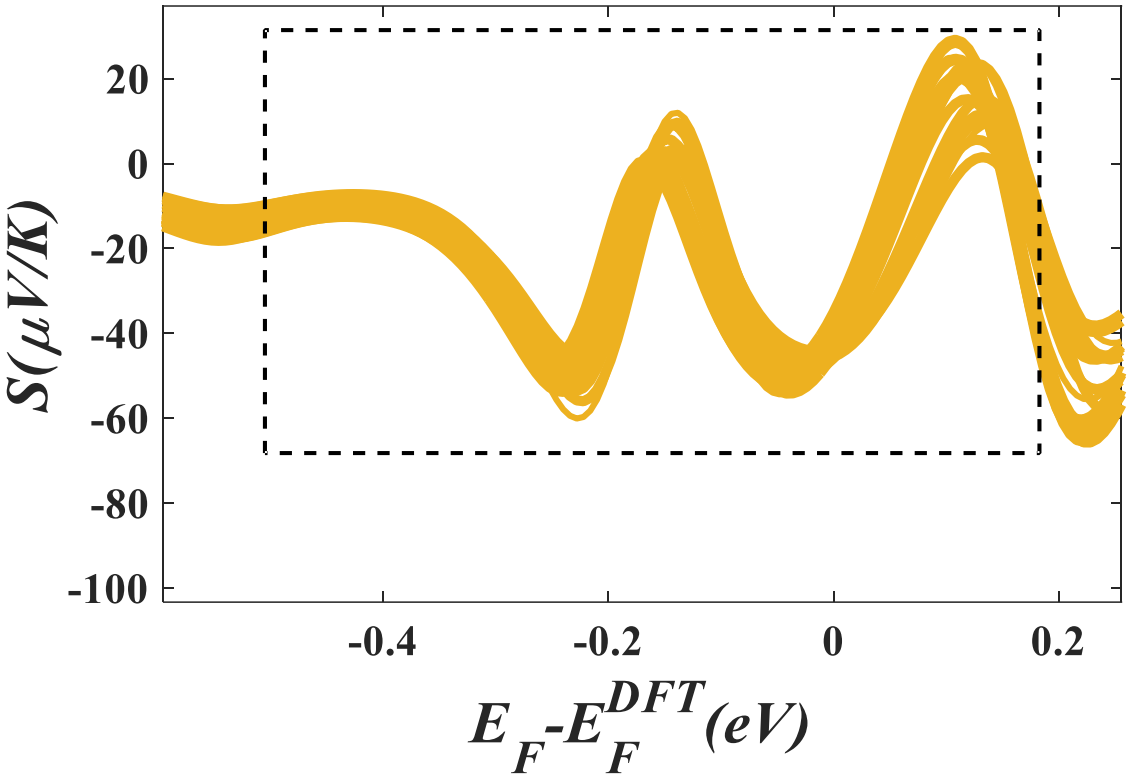

Figure 5.24. Seebeck coefficient *S* as a function of Fermi energy at 60 different orientation angles β of $Sc_3C_2@C_{80}$ for a tip-substrate distance of 2.5 Å.

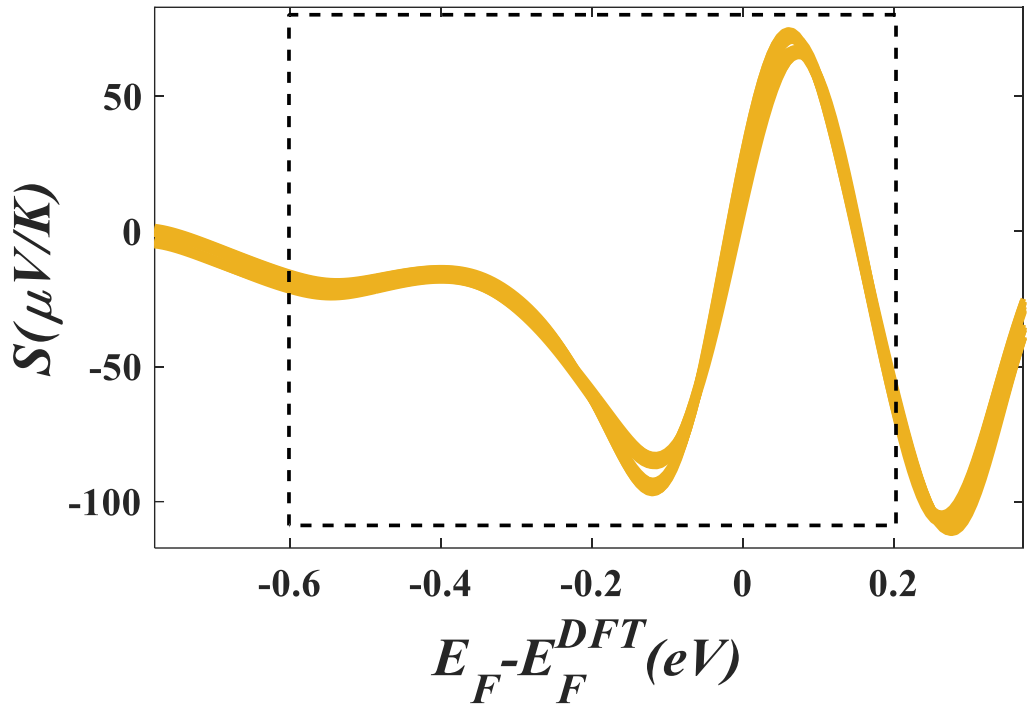

Figure 5.25. Seebeck coefficient *S* as a function of Fermi energy at 60 different orientation angles β of $Sc_3N@C_{80}$ for a tip-substrate distance of 2.5 Å.

From the Seebeck coefficient Figures 5.18-5.25 above, one could conclude that the thermopower fluctuation follows the order of $S_\theta > S_\Phi > S_\alpha > S_\beta$. The thermopower fluctuation agrees well with the conductance fluctuation order, $G_\theta > G_\Phi > G_\alpha > G_\beta$.

5.5.5. Calculated Seebeck coefficient of C_{60}

In this section, since the rotation has a negligible effect on the transmission coefficient, one would expect the Seebeck coefficient *S* to be approximately similar for all rotation angles (see Figure 5.26). It is worth mentioning, due to the absence of the extra resonance caused by the metallic moiety (C_{60} is an empty cage), that the Seebeck coefficient S does not switch sign under rotation and is negative as shown in dashed-black square of Figure 5.26.

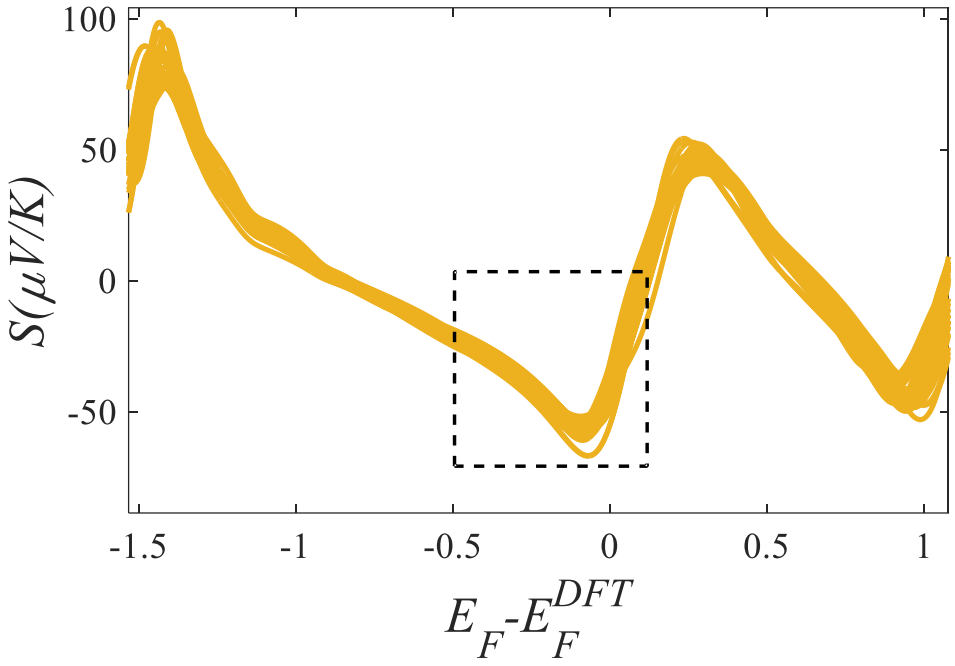

Figure 5.26. Seebeck coefficient S as a function of Fermi energy at 60 different orientations around θ, Φ, β axes of C_{60}. S versus Fermi energy at different orientation angles for a tip-substrate distance of 2.5 Å.

5.6. Standard deviation σ of $T(E)$ of EMFs and C_{60} in four different rotation axes

To calculate the standard deviations σ. I use equation 5.6 below for four different rotation axes θ, Φ, α and β, for two EMFs $Sc_3N@C_{80}$ and, $Sc_3C_2@C_{80}$ and the C_{60} fullerene. The standard deviation σ of the four axes follows $\sigma_\theta > \sigma_\Phi > \sigma_\alpha > \sigma_\beta$ for $Sc_3N@C_{80}$ and $Sc_3C_2@C_{80}$. This order is clearly shown in the transmission coefficient Figures 5.4-5.26, whereas σ of the vertical and horizontal rotation axes are approximately equal ($\sigma_\theta \approx \sigma_\alpha$) for C_{60}.

$$\sigma = \sqrt{\frac{1}{n-1}\sum_{i=1}^{n}(x_i - \bar{x})^2} \qquad (5.6)$$

where $\bar{x}$ is the mean

$$\bar{x} = \frac{1}{n}\sum_{i=1}^{n} x_i$$

Similarly, Table 5.2, contains the standard deviations σ of the Seebeck coefficient S for four different rotation axes θ, Φ, α and β, for two EMFs $Sc_3N@C_{80}$, $Sc_3C_2@C_{80}$ and C_{60} fullerene. The standard deviation σ of the four axes follows $\sigma_\theta > \sigma_\Phi > \sigma_\alpha > \sigma_\beta$ for $Sc_3N@C_{80}$ and $Sc_3C_2@C_{80}$. This order is clearly shown in the Seebeck coefficient plots (Figures 5.3-5.24), whereas for C_{60}, σ of the vertical and horizontal rotation axes are approximately equal ($\sigma_\theta \approx \sigma_\alpha$).

Table 5.1: Standard deviations σ of G/G_o in four different rotation axes θ, Φ, α and β, for two EMFs $Sc_3N@C_{80}$, $Sc_3C_2@C_{80}$ and C_{60} fullerene. Energy ranges (0.18 to -0.6), (0.18 to -0.38) and (0.0 to -0.5) eV of $Sc_3N@C_{80}$, $Sc_3C_2@C_{80}$ and C_{60}.

	G/G_o				
Molecule	σ_θ	σ_Φ	σ_α	σ_β	**Order**
$Sc_3N@C_{80}$	1.374e-01	1.086e-01	1.045e-01	2.411e-02	$\sigma_\theta > \sigma_\Phi > \sigma_\alpha > \sigma_\beta$
$Sc_3C_2@C_{80}$	2.028e-01	1.887e-01	1.406e-01	3.158e-02	$\sigma_\theta > \sigma_\Phi > \sigma_\alpha > \sigma_\beta$
C_{60}	7.256e-02	==	4.873e-02	==	$\sigma_\theta \approx \sigma_\alpha$

Table 5.2: Standard deviations σ of S in four different rotation axes θ, Φ, α and β, for two EMFs $Sc_3N@C_{80}$, $Sc_3C_2@C_{80}$ and C_{60} fullerene.

	S (μV/K)				
Molecule	σ_θ	σ_Φ	σ_α	σ_β	**Order**
$Sc_3N@C_{80}$	4.48e+01	1.83e+01	2.19e+01	4.55	$\sigma_\theta > \sigma_\Phi > \sigma_\alpha > \sigma_\beta$
$Sc_3C_2@C_{80}$	3.99e+01	2.83e+01	1.89e+01	1.23e+01	$\sigma_\theta > \sigma_\Phi > \sigma_\alpha > \sigma_\beta$
C_{60}	2.77	==	2.77	==	$\sigma_\theta \approx \sigma_\alpha$

5.7. Conductance G and thermopower S histograms of $Sc_3N@C_{80}$, $Sc_3C_2@C_{80}$ EMFs and C_{60}

In this section, I construct theoretical histograms of conductance *G* and Seebeck coefficient *S* by sampling the above results for $S(E_F)$ over Fermi energies within a range of 0.18 to -0.6 eV, centred on the metallic resonanc (next to the LUMO resonance) DFT-predicted (see the black-dashed rectangle in Figure 5.5) for $Sc_3C_2@C_{80}$. Similarly for $Sc_3N@C_{80}$ the Fermi energies within a range of 0.18 to -0.38 eV, centred on the matallic resonance DFT-predicted (see the black-dashed rectangle in Figure 5.6). For C_{60} there is no metallic resonance, however, the Fermi energies within a range of 0.0 to -0.5 eV have been considered (the black-dashed rectangle in Figure 5.16).In Figure 5.27 the theoretical histograms of conductance *G* against Seebeck coefficient *S* are shown. These calculations were taken in a range of Fermi energies of 0.18 to -0.6, 0.18 to -0.38 and 0.0 to -0.5 eV for $Sc_3C_2@C_{80}$, $Sc_3N@C_{80}$ and C_{60}, respectively. Figure 5.27 clearly shows that the Seebeck coefficient of $Sc_3C_2@C_{80}$ is larger than that of $Sc_3N@C_{80}$.

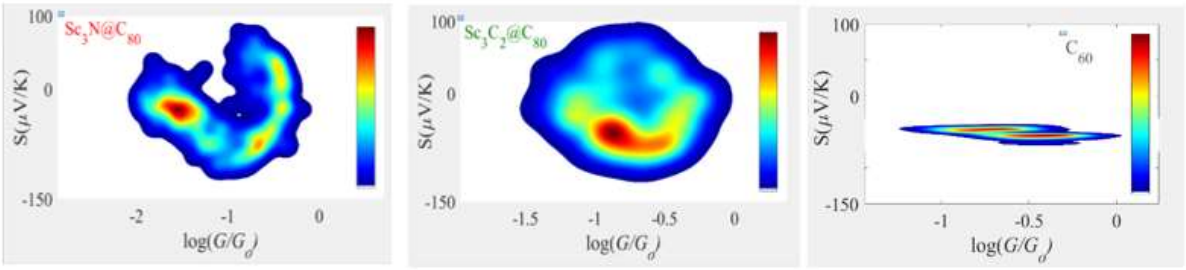

Figure 5.27. Theoretical histograms of conductance *G* against Seebeck coefficient *S*. Three ranges of Fermi energies (0.18 to -0.6), (0.18 to -0.38) and (0.0 to -0.5) eV considered for $Sc_3C_2@C_{80}$, $Sc_3N@C_{80}$ and C_{60}, respectively.

5.8. Power Factor

In this section, the power factor is calculated for $Sc_3C_2@C_{80}$, $Sc_3N@C_{80}$ and C_{60} within the same Fermi energy ranges for the four rotation axes and histograms generated. Since the conductance and Seebeck coefficient are calculated for a range of rotation angles for both $Sc_3C_2@C_{80}$ and $Sc_3N@C_{80}$, the power factor is calculated for the same angles. The black-curves in Figure 5.28 shows distributions obtained from a fit uing the Kernel Density Estimation (KDE) in MATLAB.

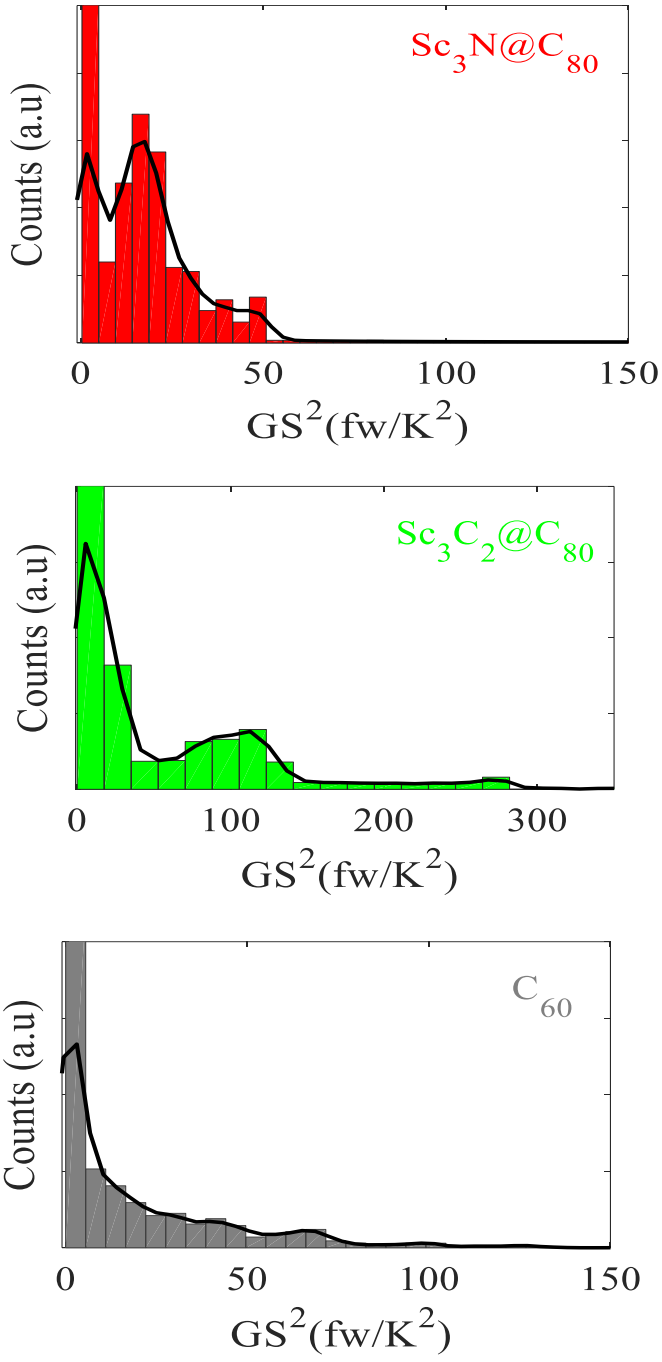

Figure 5.28. Theoretical power factor histograms for $Sc_3N@C_{80}$ (red histogram), $Sc_3C_2@C_{80}$ (green histogram), and C_{60} (grey histogram). The black lines show distributions obtained from a Kernel Density Estimation (KDE) in MATLAB.

5.9. Charge inhomogeneity

To characterize the charge inhomogeneity of each fullerene cage, I now compute the standard deviations of their charge distributions. If the charge on atom i is $|e|n_i$, then the standard deviation σ_q in the charge is defined by

$$\sigma_q^2 = < (n_i - < n_i >)^2 > \qquad (5.7)$$

where angular brackets denote an average over all atoms on the cage.

Using the DFT SIESTA code, I calculate the number of electrons n_i on each cage atom i in the gas phase for $Sc_3C_2@C_{80}$, $Sc_3N@C_{80}$, $Er_3N@C_{80}$ and C_{60} by three methods: Mülliken, Voronoi and Hirshfeld. It worth pointing out that Voronoi and Hirshfeld charges are more reliable than Mülliken charges, especially for large basis sets.

Table 5.3 shows the number of electrons on the fullerene cage for $Sc_3C_2@C_{80}$, $Sc_3N@C_{80}$, $Er_3N@C_{80}$ and C_{60} in gas phase (as isolated molecule). The number of electrons on the cage atoms vary from one molecule to another, depending on the number of atoms in the metallic moiety and the nature of these atoms.

Table 5.3: Standard deviations of charge of $Sc_3C_2@C_{80}$, $Sc_3N@C_{80}$, $Er_3N@C_{80}$ and C_{60}. Charges are calculated using Mülliken, Hirshfeld and Voronoi methods.

Molecule	Charge inhomogeneity (no. of electrons)		
	σ_{Mulliken}	$\sigma_{\text{Hirshfeld}}$	σ_{Voronoi}
$Sc_3C_2@C_{80}$	0.0154	0.0113	0.0133
$Sc_3N@C_{80}$	0.0163	0.0109	0.0119
$Er_3N@C_{80}$	0.00378	0.00259	0.00268
C_{60}	1.3e-04	5.7e-04	8.5e-04

5.10. Theory versus experiment

In this section, I shall compare discuss the theoretical simulations and STM measurements from Madrid in more depth. Note, most of the theoretical simulations were investigated in the previous chapter.

To understand the origin of the differences in Seebeck fluctuations (see Figures 5.18- 5.26), I examined the binding energies of these junctions under various rotations. The basic theoretical principles of the method can be found in the textbook [75] and basic concepts [76]. There are an infinite number of inequivalent orientations of the metallic moieties relative to their fullerene cage. Here, I consider a selection of rotations about high-symmetry axes as illustrated by Figures 4.6 and 4.7 in chapter 4.

In the gas phase, I consider rotation of the metallic moiety relative to a fixed fullerene cage. For this rotational mode, rotations about the β and Φ axes are equivalent, so in the gas phase, rotations about 3 distinct axes are investigated. In the presence of the gold substrate, I consider three modes of rotation about each of the four axes: rotation of the bare metallic moiety (in the absence of the cage), rotation of the metallic moiety in the presence of a fixed cage, and rotation of both the metallic moiety and cage, such that their relative orientation is fixed. This means that in total, on a substrate, 12 distinct cases are considered (4 axes x 3 modes of rotation). For simplicity of notation, in what follows, the same symbol (e.g. θ) is used to label both the rotation axis and the angle of rotation about the axis.

To quantify geometrical variations under rotation, it is convenient to define the distance d to be the smallest vertical distance between the top-most plane of the Au-substrate and the closest metal atom of the encapsulated moiety. Figure 4.11 shows the variation of d with rotations about the above axes, while Table 5.4 (colums 2 and 3) shows the standard deviations $\sigma_\theta, \sigma_\Phi$ in d under rotations about the axes θ, Φ. By symmetry $\sigma_\alpha = \sigma_\beta = 0$ and therefore these follow the order $\sigma_\theta > \sigma_\Phi > \sigma_\alpha, \sigma_\beta$. Furthermore,

the values of both σ_θ and σ_Φ associated with $Sc_3C_2@C_{80}$ are higher than those associated with $Sc_3N@C_{80}$ and $Er_3N@C_{80}$ (for more detail see Table 4.4 in chapter 4).

To quantify the charge inhomogeneities associated with these molecules, I also computed the standard deviations σ_q of the charge distributions on their cages, using two different definitions of charge (Hirshfeld and Voronoi) [77, 78]. These are presented in Table 5.4 (columns 4 and 5) and reveal that $Sc_3C_2@C_{80}$ and $Sc_3N@C_{80}$ possess relatively high values of σ_q, followed by $Er_3N@C_{80}$. In contrast the charge distribution of C_{60} is relatively uniform. Comparison between the experimental values for σ_S in the sixth column and the theoretical values for σ_S in the right-most column (obtained as described below), shows that standard deviations in the Seebeck coefficients are strongly correlated with the structural and charge standard deviations $\sigma_\theta, \sigma_\Phi$ and σ_q.

Table 5.4 is a key result of my study and reveals the origin of the differences in Seebeck fluctuations between the four studied molecules. Interestingly, the experimental and theoretical values of σ_s for C_{60} shown in Table 5.4 are comparable with those found for thiol-terminated oligophenylenes reported in ref [79], which varied from 2.1 to 3.2 as the number of phenyl rings was increased from 1 to 3. They are higher than those found for thiol-terminated alkyl chains, which were found to be 0.3 ± 1 and almost independent of length[80]. Studies[81-84]have also shown that increasing the applied temperature difference can lead to additional fluctuations in the thermovoltage.

Table 5.4: Standard deviations of charge, conductance and Seebeck coefficient of $Sc_3C_2@C_{80}$, $Sc_3N@C_{80}$, $Er_3N@C_{80}$ and C_{60}. Charges are calculated using Mulliken, Hirshfeld and Voronoi methods. The values shown for the conductance are geometric standard deviations. Computation of a theoretical value for σ_S of $Er_3N@C_{80}$ was not possible, due to the presence of *f*-electrons.

	Charge inhomogeneity (no. of electrons)				Conductance (G/G_o)		Seebeck (μV/K)	
Molecule	σ_{Mulliken}	$\sigma_{\text{Hirshfeld}}$	σ_{Voronoi}		σ_G **Exp.**	σ_G **Theo**	σ_S **Exp.**	σ_S **Theo.**
$Sc_3C_2@C_{80}$	0.0154	0.0113	0.0133		2.00	4.56	19.2	36.0
$Sc_3N@C_{80}$	0.0163	0.0109	0.0119		2.34	5.58	17.6	29.4
$Er_3N@C_{80}$	0.00378	0.00259	0.00268		2.00	===	7.7	==
C_{60}	1.3e-04	5.7e-04	8.5e-04		1.86	2.23	6.8	2.44

As a first step in the calculations leading to Table 5.4, energy barriers to rotation about the above axes were computed, to obtain the preferred angles of rotation, which minimise the total energy. σ_S was then obtained by computing Seebeck coefficients using an ensemble of angles and a distribution of Fermi energies E_F, as described in sections 5.4.1 to 5.5.5.

Table 4.5, shows the computed gas-phase energy barriers $\Delta E(\theta), \Delta E(\Phi), \Delta E(\alpha)$ associated with rotations about θ, Φ, α of Sc_3C_2, Sc_3N and Sc_3N within the fixed I_h-C_{80} cage, along with the preferred orientation angles for the three rotation axes (see section 4.7 of chapter 4). This reveals that for all three axes, $Sc_3C_2@C_{80}$ possesses the highest energy barriers to rotation, followed by $Sc_3N@C_{80}$, with $Er_3N@C_{80}$ possessing the lowest barriers. These correlate closely with their values of σ_q^2 and furthermore, the highest energy barrier associated with $Sc_3C_2@C_{80}$ correlates with the high value of the standard deviation in d.

Table 4.5, also shows that for all EMFs, in the gas phase, the energy barriers to rotation follow the order $\Delta E(\theta) > \Delta E(\Phi) > \Delta E(\alpha)$. Figure (4.22) shows that on a gold surface, the binding energies are also higher for the θ and Φ axes and follow the order $\Delta E(\theta) > \Delta E(\Phi) > \Delta E(\alpha) > \Delta E(\beta)$. Furthermore the barriers are higher for $Sc_3C_2@C_{80}$ and lower for $Er_3N@C_{80}$. On a gold substrate, the energy barriers significantly increase to approximately 0.6 eV for $Sc_3C_2@C_{80}$, which means that the configurational degrees of freedom of the endofullerene relative to the electrode exhibit a small number of preferred orientations corresponding to minima in the total energy of the endofullerene/electrode complex as shown in Figure (4.22) (for more detail see section 4.10 of chapter 4). The energy barrier for $Sc_3N@C_{80}$ is 0.3 eV and the lowest barrier of 0.1 eV is obtained for $Er_3N@C_{80}$ (see Figure 4.21).

To obtain the theoretical values of σ_S in Table 5.4 from the above distribution of orientations, I used a combination of the quantum transport code GOLLUM [85] and the density functional theory (DFT) code SIESTA [86] to calculate the transmission coefficient $T(E)$ for electrons of energy E passing through the EMFs, when contacted to gold electrodes (a detailed description can be found in section 4.10). The energy dependence of transmissions curves for $Sc_3C_2@C_{80}$, $Sc_3N@C_{80}$ and C_{60}, and their Seebeck coefficients for all minimum-energy orientations, are shown in Figures 5.4 to 5.26. Since the curves are rather smooth on the scale of k_BT at room temperature, their electrical conductance G is approximated by $G \approx T(E_F)G_0$, where G_0 is the quantum of conductance, and $S(E_F) \approx -S_0\left(\frac{dlnT(E)}{dE}\right)_{E=E_F}$ [75] In the latter equation, if E is measured in units of electron volts, then $S_0 = \alpha T$, which at $T = 300$ K, takes the value $S_0 = 7.3\ \mu V/K$. Figures 5.4 to 5.26 clearly show that rotations about the θ axis cause much more severe fluctuations in the transmission functions than rotations about the other axes. By sampling the transmission curves over a range of Fermi energies and preferred orientations (as described in section 4.10), I obtain the theoretical 2D histograms shown in Figure 5.27, from which the theoretical values of σ_S in Table 5.4 were obtained. In general, depending on the value of E_F, the Seebeck coefficient can achieve high values when the distance d between the metallic moiety and the Au substrate is large (e.g., for $\theta = 90°$, in Figure 5.3), whereas S tends to be lower when d is small (e.g., for $\theta = 0°$, in Figure 5.3).

The high values of σ_S and the bi-thermoelectric response of these EMF junctions confirm our initial intuition that charge inhomogeneity leads to larger variability in the transport properties, compared with pristine C_{60}. This interesting behaviour is also observed in Ref. [87], where $Gd@C_{82}$ and $Ce@C_{82}$ and the empty C_{82} were reported to present mainly negative Seebeck coefficients, with occasional positive values that were attributed possibly to meta-stable configurations of the junctions. The values reported for the Seebeck coefficient show an enhancement in the endohedral fullerenes with respect to the C_{82}. Compared to our investigated EMFs, the main difference with the systems studied in Ref. [87]is the total number of metal atoms inside the fullerene cage, which in the case of Ref [87] is just one atom placed out of centre. Of particular interest for quantifying the thermoelectric performance of molecular junctions is the power factor GS^2. Figure 6 shows a comparison between the experimental and

theoretical power factor distributions. These possess comparable shapes and, in both cases, reveal that rare values corresponding to particular configurations of the junctions can lead to very high-power factors.

Figure 5.29 also shows that the high conductance and Seebeck coefficient values measured for the carbide EMF translate into quite high values of power factor GS^2, with the highest power factor values of $Sc_3C_2@C_{80}$ significantly exceeding those of C_{60}, both in value and probability.

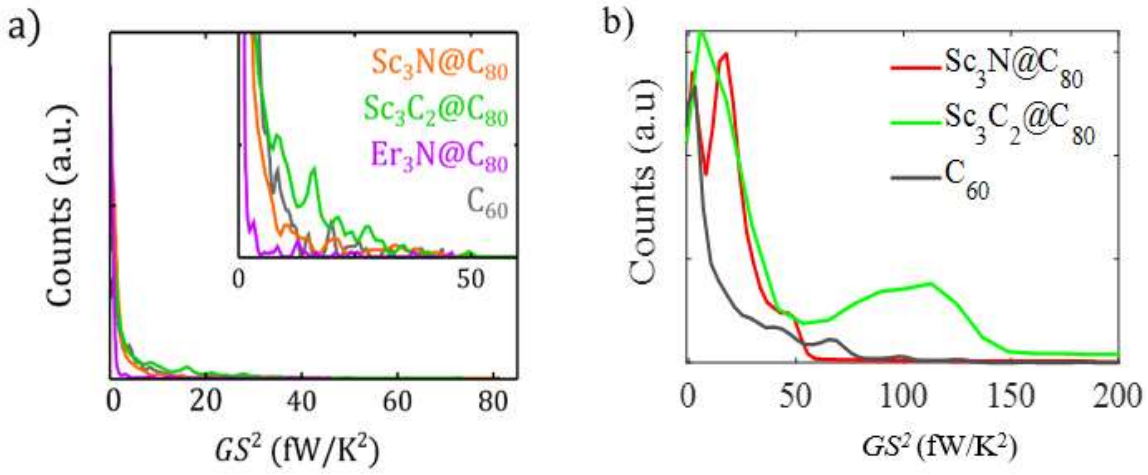

Figure 5.29. Power factor GS^2 analysis. a) Experimental 1D histograms of power factor at first contact, built with the data in Figure 1 Appendix A. The inset zooms into the details of the main panel. b). Theoretical 1D histograms of power factor obtained from Figure 5.28 in section 5.5.

Lee *et al* [87] noted that their EMF-based junctions possessed a high single molecule power factor of 16.2 fW K^{-2} for $Gd@C_{82}$, which corresponds to around 4 × 10 μW K^{-2} m^{-1} for a thin-film device consisting of a monolayer of $Gd@C_{82}$, which at the time of publication was the largest power factor obtained for a single molecule device. From the first-contact data in Figure 3(e,d) Appendix C, we find even higher values up to 50 fW K^{-2} for $Sc_3N@C_{80}$ and $Sc_3C_2@C_{80}$ junctions, and even two examples of values up to 70-80 fW K^{-2} (for these two EMFs). Statistically, we find larger values for the carbide compound ($Sc_3C_2@C_{80}$ junctions). Furthermore, considering all the measured conductance and Seebeck coefficient values (see Figure 3 Appendix C), the power factor can be statistically increased when the

junction becomes slightly compressed, because under compression, G increases and S becomes more negative.

5.10. Conclusion

In this chapter, through a combination of DFT-based transport calculations and experimental STM-based transport measurements carried out in Madrid, I studied the electrical conductance and Seebeck coefficient of three endohedral metallofullerenes (EMFs) $Sc_3N@C_{80}$, $Sc_3C_2@C_{80}$, and $Er_3N@C_{80}$, and found that their standard deviations are correlated with the degree of structural variations and the degree of charge inhomogeneity on the fullerene cages. All EMFs studied are bi-thermoelectric systems, exhibiting both positive and negative Seebeck coefficients, in contrast to the empty C_{60}.

When placed on a flat gold surface, the distance d between the top-most plane of the Au substrate and the closest metallic atom fluctuates due to rotations on the surface and the degree of variation is characterised by the associated standard deviation σ, which is a purely geometric quantity. Similarly, the degree of charge inhomogeneity on the fullerene cage can be characterised by a standard deviation σ_q. I found that standard deviations in the Seebeck coefficients σ_S of EMF-based junctions are correlated with the geometric quantity σ and the charge inhomogeneity σ_q. I benchmarked these molecules against C_{60} and found that all of σ_q, σ_S are the largest for $Sc_3C_2@C_{80}$, all are the smallest for C_{60} and for the other EMFs, they follow the order $Sc_3C_2@C_{80}$ >$Sc_3N@C_{80}$ > $Er_3N@C_{80}$ > C_{60}. This means that external measurements of fluctuations in the Seebeck coefficient provide insight into the internal structure and charge distribution of endohedral metallofullerenes.

This points the way to designs of molecular switches and bi-thermoelectric materials, because molecules with large values of σ_q possess large values of σ_S; the former is a sign that a molecule can switch between orientation-dependent electrical conductances, whereas the latter indicates that a molecule can exhibit a wide range of Seebeck coefficients with both positive and negative signs. If the orientation and Fermi energy of such molecules can be controlled, then high thermoelectric performance is possible. On the other hand, if the aim is to minimise fluctuations, then our study suggests that molecules with low values of σ and σ_q should be selected

Bibliography

1. Noori, M., Sadeghi, H., and Lambert, C. J. (2017). High-performance thermoelectricity in edge-over-edge zinc-porphyrin molecular wires. *Nanoscale*, *9*(16), 5299-5304.
2. Yzambart, G., Rincón-García, L., Al-Jobory, A. A., Ismael, A. K., Rubio-Bollinger, G., Lambert, C. J., Agraït, N., and Bryce, M. R. (2018). Thermoelectric properties of 2, 7-dipyridylfluorene derivatives in single-molecule junctions. *The Journal of Physical Chemistry C*, *122*(48), 27198-27204.
3. Ismael, A. (2017). *Towards molecular-scale sensing and thermoelectric energy harvesting* (Doctoral dissertation, Lancaster University).
4. Wu, Q., Sadeghi, H., García-Suárez, V. M., Ferrer, J., and Lambert, C. J. (2017). Thermoelectricity in vertical graphene-C 60-graphene architectures. *Scientific reports*, *7*(1), 1-8.
5. Sadeghi, H., Sangtarash, S., and Lambert, C. J. (2015). Electron and heat transport in porphyrin-based single-molecule transistors with electro-burnt graphene electrodes. *Beilstein journal of nanotechnology*, *6*(1), 1413-1420.
6. Massonnet, N., Carella, A., Jaudouin, O., Rannou, P., Laval, G., Celle, C., and Simonato, J. P. (2014). Improvement of the Seebeck coefficient of PEDOT: PSS by chemical reduction combined with a novel method for its transfer using free-standing thin films. *Journal of Materials Chemistry C*, *2*(7), 1278-1283.
7. Davidson, R. J., Milan, D. C., Al-Owaedi, O. A., Ismael, A. K., Nichols, R. J., Higgins, S. J., and Beeby, A. (2018). Conductance of 'bare-bones' tripodal molecular wires. *RSC advances*, *8*(42), 23585-23590.
8. Sangtarash, S., Sadeghi, H., and Lambert, C. J. (2018). Connectivity-driven bi-thermoelectricity in heteroatom-substituted molecular junctions. *Physical Chemistry Chemical Physics*, *20*(14), 9630-9637.

9. Algharagholy, L. A. A., Pope, T., and Lambert, C. J. (2018). Strain-induced bi-thermoelectricity in tapered carbon nanotubes. *Journal of Physics: Condensed Matter*, *30*(10), 105304.
10. La Rosa, A., Gillemot, K., Leary, E., Evangeli, C., González, M. T., Filippone, S., Rubio-Bollinger, G., Agrait, N., Lambert, C. J., and Martin, N. (2014). Does a Cyclopropane Ring Enhance the Electronic Communication in Dumbbell-Type C60 Dimers. *The Journal of organic chemistry*, *79*(11), 4871-4877.
11. Pauly, F., Viljas, J. K., and Cuevas, J. C. (2008). Length-dependent conductance and thermopower in single-molecule junctions of dithiolated oligophenylene derivatives: A density functional study. *Physical Review B*, *78*(3), 035315.
12. Nozaki, D., Sevinçli, H., Li, W., Gutiérrez, R., and Cuniberti, G. (2010). Engineering the figure of merit and thermopower in single-molecule devices connected to semiconducting electrodes. *Physical Review B*, *81*(23), 235406.
13. Bürkle, M., Zotti, L. A., Viljas, J. K., Vonlanthen, D., Mishchenko, A., Wandlowski, T., Mayor, M., Schön, G., and Pauly, F. (2012). Ab initio study of the thermopower of biphenyl-based single-molecule junctions. *Physical review b*, *86*(11), 115304.
14. Evangeli, C., Gillemot, K., Leary, E., Gonzalez, M. T., Rubio-Bollinger, G., Lambert, C. J., and Agrait, N. (2013). Engineering the thermopower of C60 molecular junctions. *Nano letters*, *13*(5), 2141-2145.
15. Karlström, O., Strange, M., and Solomon, G. C. (2014). Understanding the length dependence of molecular junction thermopower. *The Journal of chemical physics*, *140*(4), 044315.
16. Péterfalvi, C. G., Grace, I., Manrique, D. Z., and Lambert, C. J. (2014). Thermoelectric performance of various benzo-difuran wires. *The Journal of chemical physics*, *140*(17), 174711.

17. García-Suárez, V. M., Lambert, C. J., Manrique, D. Z., and Wandlowski, T. (2014). Redox control of thermopower and figure of merit in phase-coherent molecular wires. *Nanotechnology*, *25*(20), 205402.
18. Ismael, A. K., Grace, I., and Lambert, C. J. (2015). Increasing the thermopower of crown-ether-bridged anthraquinones. *Nanoscale*, *7*(41), 17338-17342.
19. Sadeghi, H., Sangtarash, S., and Lambert, C. J. (2015). Oligoyne molecular junctions for efficient room temperature thermoelectric power generation. *Nano letters*, *15*(11), 7467-7472.
20. Bürkle, M., Hellmuth, T. J., Pauly, F., and Asai, Y. (2015). First-principles calculation of the thermoelectric figure of merit for [2, 2] paracyclophane-based single-molecule junctions. *Physical Review B*, *91*(16), 165419.
21. Rincón-García, L., Ismael, A. K., Evangeli, C., Grace, I., Rubio-Bollinger, G., Porfyrakis, K., Agraït, N., and Lambert, C. J. (2016). Molecular design and control of fullerene-based bi-thermoelectric materials. *Nature materials*, *15*(3), 289-293.
22. Perroni, C. A., Ninno, D., and Cataudella, V. (2016). Thermoelectric efficiency of molecular junctions. *Journal of Physics: Condensed Matter*, *28*(37), 373001.
23. Manrique, D. Z., Al-Galiby, Q., Hong, W., and Lambert, C. J. (2016). A new approach to materials discovery for electronic and thermoelectric properties of single-molecule junctions. *Nano letters*, *16*(2), 1308-1316.
24. Rincón-García, L., Evangeli, C., Rubio-Bollinger, G., and Agraït, N. (2016). Thermopower measurements in molecular junctions. *Chemical Society Reviews*, *45*(15), 4285-4306.
25. Lambert, C. J., Sadeghi, H., and Al-Galiby, Q. H. (2016). Quantum-interference-enhanced thermoelectricity in single molecules and molecular films. *Comptes Rendus Physique*, *17*(10), 1084-1095.

26. Li, Y., Xiang, L., Palma, J. L., Asai, Y., and Tao, N. (2016). Thermoelectric effect and its dependence on molecular length and sequence in single DNA molecules. *Nature communications*, *7*(1), 1-8.

27. Cui, L., Miao, R., Jiang, C., Meyhofer, E., and Reddy, P. (2017). Perspective: Thermal and thermoelectric transport in molecular junctions. *The Journal of Chemical Physics*, *146*(9), 092201.

28. Gehring, P., Harzheim, A., Spiece, J., Sheng, Y., Rogers, G., Evangeli, C., ... and Mol, J. A. (2017). Field-effect control of graphene–fullerene thermoelectric nanodevices. *Nano letters*, *17*(11), 7055-7061.

29. Klöckner, J. C., Siebler, R., Cuevas, J. C., and Pauly, F. (2017). Thermal conductance and thermoelectric figure of merit of C 60-based single-molecule junctions: electrons, phonons, and photons. *Physical Review B*, *95*(24), 245404.

30. Al-Galiby, Q. H., Sadeghi, H., Manrique, D. Z., and Lambert, C. J. (2017). Tuning the Seebeck coefficient of naphthalenediimide by electrochemical gating and doping. *Nanoscale*, *9*(14), 4819-4825.

31. Wang, X., Bennett, T. L., Ismael, A., Wilkinson, L. A., Hamill, J., White, A. J., Grace, I. M., Kolosov, O. V., Albrecht, T., Robinson, B. J., Long, N. J., and Lambert, C. J. (2020). Scale-up of room-temperature constructive quantum interference from single molecules to self-assembled molecular-electronic films. *Journal of the American Chemical Society*, *142*(19), 8555-8560.

32. Ismael, A., Al-Jobory, A., Wang, X., Alshehab, A., Almutlg, A., Alshammari, M., Grace, I., Benett, T. L., Wilkinson, L. A, Robinson, B. J., Long, N. J., and Lambert, C. (2020). Molecular-scale thermoelectricity: as simple as 'ABC'. *Nanoscale Advances*, *2*(11), 5329-5334.

33. Ismael, A., Wang, X., Bennett, T. L., Wilkinson, L. A., Robinson, B. J., Long, N. J., Cohen, L. F., and Lambert, C. J. (2020). Tuning the thermoelectrical properties of anthracene-based self-assembled monolayers. *Chemical science*, *11*(26), 6836-6841.
34. Wang, X., Ismael, A., Almutlg, A., Alshammari, M., Al-Jobory, A., Alshehab, A., Bennett, T. L., Wilkinson, L. A., Cohen, L. F., Long, N. J., Robinson, B. J., and Lambert, C. (2021). Optimised power harvesting by controlling the pressure applied to molecular junctions. *Chemical Science*, *12*(14), 5230-5235.
35. Harzheim, A. (2018). Thermoelectricity in single-molecule devices. *Materials Science and Technology*, *34*(11), 1275-1286.
36. Algharagholy, L. A. A., Pope, T., and Lambert, C. J. (2018). Strain-induced bi-thermoelectricity in tapered carbon nanotubes. *Journal of Physics: Condensed Matter*, *30*(10), 105304.
37. Bennett, T. L., Alshammari, M., Au-Yong, S., Almutlg, A., Wang, X., Wilkinson, L. A., Albrecht, T., Jarvis, S., Cohen, L., Ismael, Ali., Lambert, C. J., Robinson, B., and Long, N. J. (2022). Multi-component self-assembled molecular-electronic films: towards new high-performance thermoelectric systems. *Chemical Science*, *13*(18), 5176-5185.
38. Miao, R., Xu, H., Skripnik, M., Cui, L., Wang, K., Pedersen, K. G., Leijnse, M., Pauly, F., Warnmark, K., Meyhofer, E., Reddy, P., and Linke, H. (2018). Influence of quantum interference on the thermoelectric properties of molecular junctions. *Nano letters*, *18*(9), 5666-5672.
39. Al-Khaykanee, M. K., Ismael, A. K., Grace, I., and Lambert, C. J. (2018). Oscillating Seebeck coefficients in π-stacked molecular junctions. *RSC advances*, *8*(44), 24711-24715.

40. Cui, L., Miao, R., Wang, K., Thompson, D., Zotti, L. A., Cuevas, J. C., Meyhofer, E., and Reddy, P. (2018). Peltier cooling in molecular junctions. *Nature nanotechnology*, *13*(2), 122-127.

41. Famili, M., Grace, I. M., Al-Galiby, Q., Sadeghi, H., and Lambert, C. J. (2018). Toward high thermoelectric performance of thiophene and ethylenedioxythiophene (EDOT) molecular wires. *Advanced Functional Materials*, *28*(15), 1703135.

42. Khalatbari, H., Vishkayi, S. I., and Soleimani, H. R. (2019). Effect of dopant nitrogen on the thermoelectric properties of C20 and C60 fullerene in graphene nanoribbon junction. *Physica E: Low-dimensional Systems and Nanostructures*, *108*, 372-381.

43. Chen, H., Sangtarash, S., Li, G., Gantenbein, M., Cao, W., Alqorashi, A., Liu, J., Zhang, C., Zhang, Y., Chen, L., Chen, Y., and Hong, W. (2020). Exploring the thermoelectric properties of oligo (phenylene-ethynylene) derivatives. *Nanoscale*, *12*(28), 15150-15156.

44. Ismael, A. K., and Lambert, C. J. (2020). Molecular-scale thermoelectricity: a worst-case scenario. *Nanoscale Horizons*, *5*(7), 1073-1080.

45. Noori, M., Sadeghi, H., Al-Galiby, Q., Bailey, S. W., and Lambert, C. J. (2017). High cross-plane thermoelectric performance of metallo-porphyrin molecular junctions. *Physical Chemistry Chemical Physics*, *19*(26), 17356-17359.

46. Sangtarash, S., Sadeghi, H., and Lambert, C. J. (2018). Connectivity-driven bi-thermoelectricity in heteroatom-substituted molecular junctions. *Physical Chemistry Chemical Physics*, *20*(14), 9630-9637.

47. Noori, M., Sadeghi, H., and Lambert, C. J. (2018). Stable-radicals increase the conductance and Seebeck coefficient of graphene nanoconstrictions. *Nanoscale*, *10*(40), 19220-19223.

48. Dekkiche, H., Gemma, A., Tabatabaei, F., Batsanov, A. S., Niehaus, T., Gotsmann, B., and Bryce, M. R. (2020). Electronic conductance and thermopower of single-molecule junctions of oligo (phenyleneethynylene) derivatives. *Nanoscale*, *12*(36), 18908-18917.

49. Akkermans, E., and Montambaux, G. (2007). *Mesoscopic physics of electrons and photons*. Cambridge university press.

50. Datta, S. (1997). *Electronic transport in mesoscopic systems*. Cambridge university press.

51. Hong, W., Valkenier, H., Mészáros, G., Manrique, D. Z., Mishchenko, A., Putz, A., García, P. M., Lambert, C. J., Hummelen, J. C., and Wandlowski, T. (2011). An MCBJ case study: The influence of π-conjugation on the single-molecule conductance at a solid/liquid interface. *Beilstein journal of nanotechnology*, *2*(1), 699-713.

52. Sedghi, G., García-Suárez, V. M., Esdaile, L. J., Anderson, H. L., Lambert, C. J., Martín, S., and Nichols, R. J. (2011). Long-range electron tunnelling in oligo-porphyrin molecular wires. *Nature nanotechnology*, *6*(8), 517-523.

53. Ballmann, S., Härtle, R., Coto, P. B., Elbing, M., Mayor, M., Bryce, M. R., Thoss, M., and Weber, H. B. (2012). Experimental evidence for quantum interference and vibrationally induced decoherence in single-molecule junctions. *Physical review letters*, *109*(5), 056801.

54. Kaliginedi, V., Moreno-García, P., Valkenier, H., Hong, W., García-Suárez, V. M., Buiter, P., Otten, J.L.H., Hummelen, J.C., Lambert C.J. and and Wandlowski, T. (2012). Correlations between molecular structure and single-junction conductance: a case study with oligo (phenylene-ethynylene)-type wires. *Journal of the American Chemical Society*, *134*(11), 5262-5275.

55. Chaste, J., and Eichler, A., E Moser, J.; Ceballos, G.; Rurali, R.; Bachtold. *A. A* (2012). *nanomechanical mass sensor with yoctogram resolution. Nat. Nanotechnol*, *7*, 301-304.

56. Vazquez, H., Skouta, R., Schneebeli, S., Kamenetska, M., Breslow, R., Venkataraman, L., and Hybertsen, M. S. (2012). Probing the conductance superposition law in single-molecule circuits with parallel paths. *Nature Nanotechnology*, *7*(10), 663-667.

57. Hong, W., Manrique, D. Z., Moreno-García, P., Gulcur, M., Mishchenko, A., Lambert, C. J., Bryce M.R. and Wandlowski, T. (2012). Single molecular conductance of tolanes: experimental and theoretical study on the junction evolution dependent on the anchoring group. *Journal of the American Chemical Society*, *134*(4), 2292-2304.

58. Arroyo, C. R., Tarkuc, S., Frisenda, R., Seldenthuis, J. S., Woerde, C. H., Eelkema, R., and Van Der Zant, H. S. (2013). Signatures of quantum interference effects on charge transport through a single benzene ring. *Angewandte Chemie International Edition*, *52*(11), 3152-3155.

59. Geng, Y., Sangtarash, S., Huang, C., Sadeghi, H., Fu, Y., Hong, W., Wandlowski, T., Decurtins, S., Lambert, C. J., and Liu, S. X. (2015). Magic ratios for connectivity-driven electrical conductance of graphene-like molecules. *Journal of the American Chemical Society*, *137*(13), 4469-4476.

60. Garner, M. H., Li, H., Chen, Y., Su, T. A., Shangguan, Z., Paley, D. W., Liu, T., Ng, F., Li, H., Xiao, S., Nuckolls, C., and Solomon, G. C. (2018). Comprehensive suppression of single-molecule conductance using destructive σ-interference. *Nature*, *558*(7710), 415-419.

61. Ito, Y., Okazaki, T., Okubo, S., Akachi, M., Ohno, Y., Mizutani, T., Nakamura, T., Kitaura, R., Sugai, T., and Shinohara, H. (2007). Enhanced 1520 nm

photoluminescence from Er3+ ions in di-erbium-carbide metallofullerenes (Er2C2) @ C82 (isomers I, II, and III). *ACS nano*, *1*(5), 456-462.

62. Dunsch, L., and Yang, S. (2007). Metal nitride cluster fullerenes: their current state and future prospects. *Small*, *3*(8), 1298-1320.

63. Chen, C. H. (2017). Krylov DS Avdoshenko SM Liu F. *Spree L. Yadav R. Alvertis A. Hozoi L. Nenkov K. Kostanyan A. Greber T. Wolter AUB Popov AA Chem. Sci*, *8*, 6451-6465.

64. Tran, C. D., and Gao, G. H. (1996). Characterization of an erbium-doped fiber amplifier as a light source and development of a near-infrared spectrophotometer based on the EDFA and an acoustooptic tunable filter. *Analytical chemistry*, *68*(13), 2264-2269.

65. Krause, M., Hulman, M., Kuzmany, H., Dubay, O., Kresse, G., Vietze, K., Seifert, G., Wang, C., and Shinohara, H. (2004). Fullerene quantum gyroscope. *Physical review letters*, *93*(13), 137403.

66. Rodríguez-Fortea, A., Balch, A. L., and Poblet, J. M. (2011). Endohedral metallofullerenes: a unique host–guest association. *Chemical Society Reviews*, *40*(7), 3551-3563.

67. Rodríguez-Fortea, A., Irle, S., and Poblet, J. M. (2011). Fullerenes: formation, stability, and reactivity. *Wiley Interdisciplinary Reviews: Computational Molecular Science*, *1*(3), 350-367.

68. Aparicio-Angles, X., Alegret, N., Clotet, A., Rodríguez-Fortea, A., and Poblet, J. M. (2013). Endohedral metallofullerenes containing lanthanides: a robust yet simple computational approach. *The Journal of Physical Chemistry C*, *117*(24), 12916-12921.

69. Gillemot, K. (2013). Quantum control of electrical and thermoelectrical transport in molecular-scale structures. Lancaster University (United Kingdom).

70. Li, Y. S., and Wang, X. F. (2018). Manipulation of the magnetoresistance effect in a double-helix DNA. *Journal of Physics: Condensed Matter*, *30*(45), 455102.

71. Xiong, Z. H., Wu, D., Vardeny, Z. V., and Shi, J. (2004). Giant magnetoresistance in organic spin-valves. *Nature*, *427*(6977), 821-824.

72. Göhler, B., Hamelbeck, V., Markus, T. Z., Kettner, M., Hanne, G. F., Vager, Z., Naaman, R., and Zacharias, H. (2011). Spin selectivity in electron transmission through self-assembled monolayers of double-stranded DNA. *Science*, *331*(6019), 894-897.

73. Göhler, B., Hamelbeck, V., Markus, T. Z., Kettner, M., Hanne, G. F., Vager, Z., Naaman, R., and Zacharias, H. (2011). Spin selectivity in electron transmission through self-assembled monolayers of double-stranded DNA. *Science*, *331*(6019), 894-897.

74. Xie, Z., Markus, T. Z., Cohen, S. R., Vager, Z., Gutierrez, R., and Naaman, R. (2011). Spin specific electron conduction through DNA oligomers. *Nano letters*, *11*(11), 4652-4655.

75. Lambert, C. J. (2021). *Quantum Transport in Nanostructures and Molecules*. IOP Publishing.

76. Lambert, C. J. (2015). Basic concepts of quantum interference and electron transport in single-molecule electronics. *Chemical Society Reviews*, *44*(4), 875-888.

77. Fonseca Guerra, C., Handgraaf, J. W., Baerends, E. J., and Bickelhaupt, F. M. (2004). Voronoi deformation density (VDD) charges: Assessment of the Mulliken, Bader, Hirshfeld, Weinhold, and VDD methods for charge analysis. *Journal of computational chemistry*, *25*(2), 189-210.

78. Hirshfeld, F. L. (1977). Bonded-atom fragments for describing molecular charge densities. *Theoretica chimica acta*, *44*(2), 129-138.

79. Reddy, P., Jang, S. Y., Segalman, R. A., and Majumdar, A. (2007). Thermoelectricity in molecular junctions. *Science*, *315*(5818), 1568-1571.

80. Malen, J. A., Doak, P., Baheti, K., Tilley, T. D., Segalman, R. A., and Majumdar, A. (2009). Identifying the length dependence of orbital alignment and contact coupling in molecular heterojunctions. *Nano letters*, *9*(3), 1164-1169.

81. Park, S., Cho, N., and Yoon, H. J. (2019). Two Different Length-Dependent Regimes in Thermoelectric Large-Area Junctions of n-Alkanethiolates. *Chemistry of Materials*, *31*(15), 5973-5980.

82. Park, S., Jang, J., and Yoon, H. J. (2021). Validating the Mott Formula with Self-Assembled Monolayer (SAM)-Based Large-Area Junctions: Effect of Length, Backbone, Spacer, Substituent, and Electrode on the Thermopower of SAMs. *The Journal of Physical Chemistry C*, *125*(36), 20035-20047.

83. Park, S., Kang, S., and Yoon, H. J. (2019). Power factor of one molecule thick films and length dependence. *ACS central science*, *5*(12), 1975-1982.

84. Park, S., and Yoon, H. J. (2018). New Approach for large-area thermoelectric junctions with a liquid eutectic gallium–indium electrode. *Nano letters*, *18*(12), 7715-7718.

85. Ferrer, J., Lambert, C. J., García-Suárez, V. M., Manrique, D. Z., Visontai, D., Oroszlany, L., Rodríguez-Ferradás, R., Grace, I., Bailey S. W., Gillemot, K., Sadeghi H., and Algharagholy, L. A. (2014). GOLLUM: a next-generation simulation tool for electron, thermal and spin transport. *New Journal of Physics*, *16*(9), 093029.

86. Soler, J. M., Artacho, E., Gale, J. D., García, A., Junquera, J., Ordejón, P., and Sánchez-Portal, D. (2002). The SIESTA method for ab initio order-N materials simulation. *Journal of Physics: Condensed Matter*, *14*(11), 2745.

87. Lee, S. K., Buerkle, M., Yamada, R., Asai, Y., and Tada, H. (2015). Thermoelectricity at the molecular scale: a large Seebeck effect in endohedral metallofullerenes. *Nanoscale*, *7*(48), 20497-20502.

Chapter 6

Conclusion and Future Work

6.1 Conclusion

In conclusion, I have discussed the essential equations and tools that underpin my work, including the Schrödinger equation, density functional theory (DFT), and the SIESTA programme, which implements DFT and solves these equations. I have also discussed single particle transport theory, which is based on the Hamiltonian and Green's functions, and provided some examples of how it might be used. These ideas are discussed in chapters 2 and 3, respectively.

In chapter 4, my aim was to study the three endohedral metallofullerenes (EMFs) $Sc_3N@C_{80}$, $Sc_3C_2@C_{80}$ and $Er_3N@C_{80}$ and compare them with C_{60}. I began my explorations by presenting the wave function plots of the studied molecules. I chose three different methods including Mulliken population, Hirshfeld and Voronoi, then I investigated the charge transfer immigration between metallic moieties and the cage. The charge transfer analyses were applied in the gas phase and on a gold substrate. I used the counterpoise method to evaluate the most energy favourable orientation of metallic moieties such as Sc_3N, Er_3N and Sc_3C_2 to settle inside the I_h-cage.

I have demonstrated how θ, Φ, α and β axes play an important role in the conductance and Seebeck coefficient fluctuations. I also investigated how the total energy varies with the angle of rotation, both in presence and absence of the gold substrate. There are an infinite number of inequivalent orientations of the metallic moieties comparative to their fullerene cage. Moreover, for each of the four axes, I considerd one mode of rotation in the gas phase and three modes of rotation on a substrate. I used DFT to determine the optimum distances between EMFs and the metallic electrodes.

In Chapter 5, I employed the parameters that I explored in chapter 4, and exploited them to support my simulations. Then I demonstrated, that standard deviations in the Seebeck coefficient σ_S of EMF-based junctions are related to the geometric quantity σ and charge inhomogeneity σ_q, which is an interesting

structure-function relationship. I examined EMF molecules to C_{60} and demonstrate that both σ_q, σ_S are the largest for $Sc_3C_2@C_{80,}$ and both are the smallest for C_{60} while, the other EMFs, they follow the order $Sc_3C_2@C_{80}$ >$Sc_3N@C_{80}$ > $Er_3N@C_{80}$ > C_{60}.

A high value of σ_S is a sign that a molecule can exhibit a wide range of Seebeck coefficients and if orientations corresponding to large range can be handpicked and controlled, then the molecule has the potential to exhibit high-performance thermoelectricity. Large values of σ_S are related to distributions of Seebeck coefficients with both positive and negative signs for the EMFs investigated here, indicating that all of these EMFs are bi-thermoelectric materials. Further to that, molecules with high charge inhomogeneity exhibit rare examples of high thermopower, which means that if these rare junction configurations could be isolated and controlled, then such molecules have the potential to deliver high-performance thermoelectricity.

6.2 Future work

In this thesis, I have focused on investigating the electrical conductance G and the Seebeck coefficient S of three EMFs and $C_{60.}$ My goal is to support the aim of producing single-molecule junctions that can convert a temperature differential ΔT into a voltage ΔV through the Seebeck effect, It is significant to examine molecules for their producing high values of the Seebeck coefficient $S = -\frac{\Delta V}{\Delta T}$. When single molecules are sandwiched between two electrodes to build single-molecule junctions, it is standard practice to make thousands of measurements of their Seebeck coefficients, because their values fluctuate due to random binding configurations of the molecule within the junction and variations in the electrode Fermi energy E_F relative to energies of frontier orbitals.

For the future work, it would be interesting to include a single atom inside a cage and explore where it settles inside the cavity (rattling) and what effect that has on G and S. It would also be of interest to use established methods of computing phonon transport [1,2] to predict the effect of encapsulated atoms on thermal conductance. For a single atom, a small cage such as C_{60} might fit better than large cage C_{80}

and therefore all these parameters need to be investigated. Another avenue for future exploration is to use different electrodes, for instance graphene [3,4], platinum or palladium [5] and examine their effect on fluctuation in G and S Recently, quantum interfernce effects in superconducting nano-junctions [6,7] have been shown to combine with intra-molecular quantum interference effect to yield unique interference phenomena [8] and it would be of interest to examine how these are modified in junctions formed from endohedral fullerenes.

Bibliography

1. Kambili, A., Fagas, G., Fal'ko, V. I., and Lambert, C. J. (1999). Phonon-mediated thermal conductance of mesoscopic wires with rough edges. *Physical review b*, *60*(23), 15593.
2. N. Mosso, H. Sadeghi, A. Gemma, S. Sangtarash, C. Lambert, and B. Gotsmann, (2019) Thermal transport through single molecule junctions. *Nanoletters* 19 (11) 7614-7622.
3. Limburg, B., Thomas, J. O., Holloway, G., Sadeghi, H., Sangtarash, S., Hou, I. C. Y., Cremers, J., Narita, A., Müllen, K., Lambert, C. J., Briggs, G. A., Anderson, H. L. (2018). Anchor Groups for Graphene-Porphyrin Single-Molecule Transistors. *Advanced Functional Materials*, *28*(45), 1803629.
4. Zheng, X. H., Zhang, G. R., Zeng, Z., García-Suárez, V. M., and Lambert, C. J. (2009). Effects of antidots on the transport properties of graphene nanoribbons. *Physical Review b*, *80*(7), 075413 (2009)
5. García-Suárez, V.M., Rocha, A. R., Bailey, S.W., Lambert, C. J., Sanvito, S. and Ferrer, J. (2005) Single-channel conductance of H 2 molecules attached to platinum or palladium electrodes. *Physical Review B* 72 (4), 045437
6. Lambert, C.J., Raimondi, R., Sweeney, V. and Volkov V.F. (1997) Boundary conditions for quasiclassical equations in the theory of superconductivity. Physical Review B 55 (9), 6015
7. Hui, V. C., and Lambert C.J. (1993) *Europhysics Letters* 23 (3), 203.
8. Plaszkó, N. L., Rakyta, P., Cserti, J., Kormányos, A. and Lambert, C.J. (2020) Quantum interference and non-equilibrium Josephson current in molecular Andreev interferometers. *Nanomaterials* 10,1033.

Appendices

Appendix A: Spectroscopic characterization and band gap calculation.

In Figure 1 we present the UV-Visible spectra (Figure 1a) for the two TNTs that were recorded in Madrid in o-dichlorobenzene solutions. The direct optical band gaps of the two trimetallic nitride endohedral metallofullerenes were calculated from the Tauc plots that can be seen in Figure 1b. The energy of the transition, in eV, is plotted against $(\alpha h\nu)^{1/r}$. For a direct allowed transition, we consider a value of r=1/2. Consequently, the band gaps are calculated to be 2.466 eV for $Sc_3N@C_{80}$ and 2.54 eV for $Er_3N@C_{80}$ from the fitting of the Tauc plot.

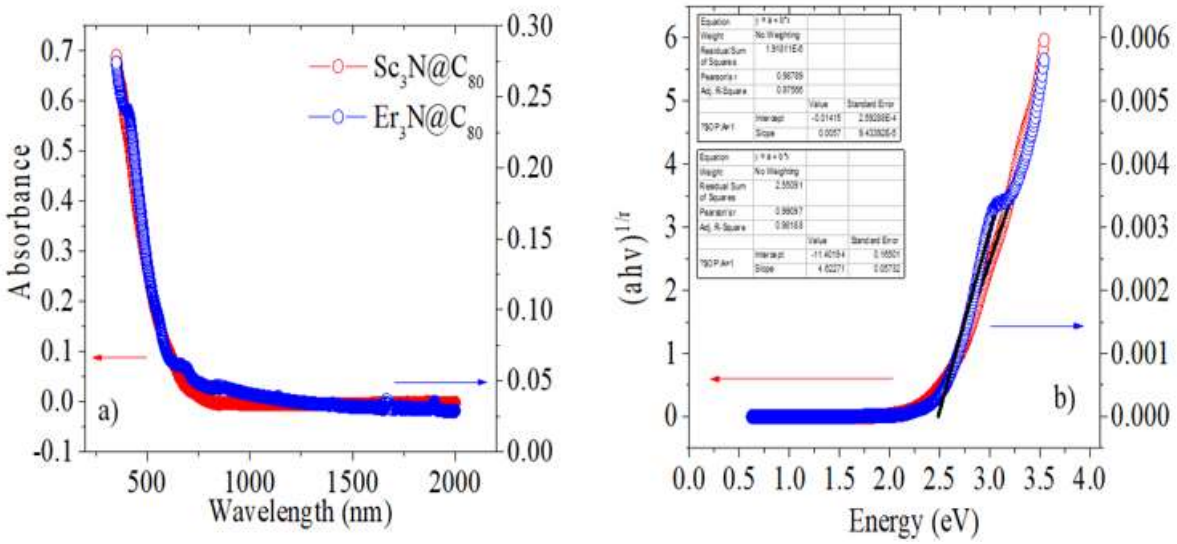

Figure 1. UV-Visible absorbance spectra (a) and Tauc plots (b) recorded in o-dichlorobenzene solutions for $Er_3N@C_{80}$ (blue) and $Sc_3N@C_{80}$ (red). The direct, optical band gaps, taking into consideration a value for r=1/2 are: 2.54 eV for $Er_3N@C_{80}$ and 2.46 eV for $Sc_3N@C_{80}$. The values are calculated from a fitting on the linear regime of the Tauc plot.

Appendix B: EPR spectra:

MALDI-TOF data are providing invaluable information for the formation of endohedral metallofullerenes species, however, they do not provide with a definite proof on the structure of the buckyball and the species incarcerated within. To that end, we recorded the EPR spectra and they demonstrated the unique diamond shape with 22 lines that arises from three equivalent scandium nuclei. The spectra for the temperature range 170—290 K can be seen in Figure 2.

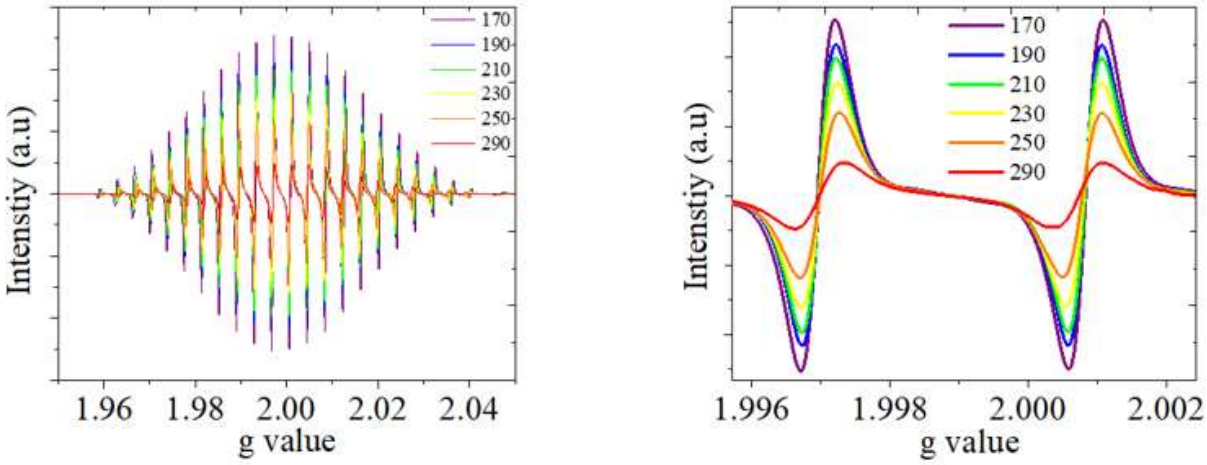

Figure 2. EPR spectra of the paramagnetic $Sc_3C_2@C_{80}$ recorded at various temperatures (170-290 K). The 22 lines stemming from three equivalent scandium (I=7/2) nuclei demonstrate the unambiguous synthesis of the trimetallic carbide.

Appendix C: G, S, and GS^2 1D histograms for single-molecule junctions:

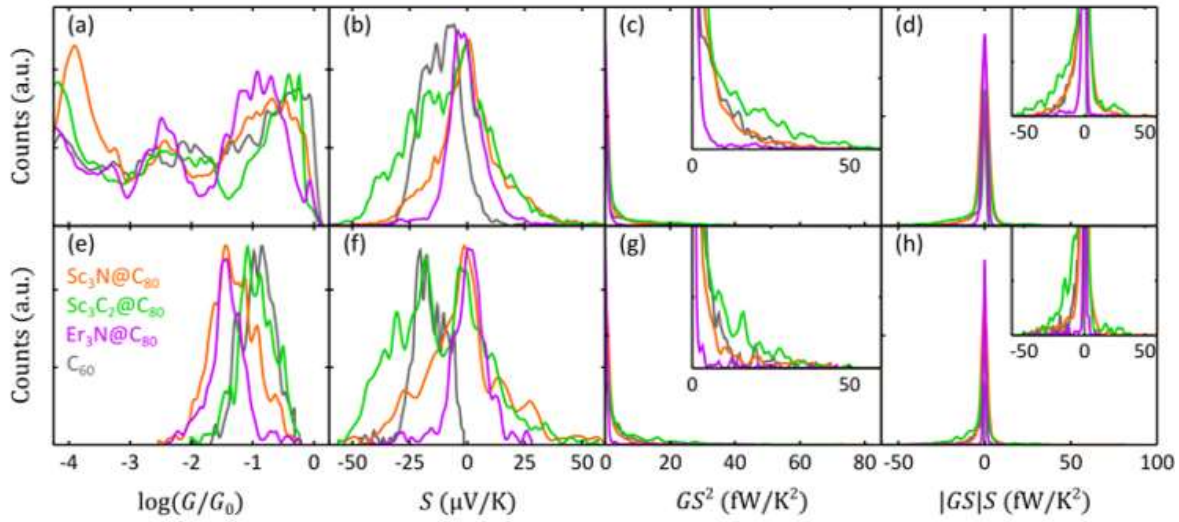

Figure 3. Conductance G, thermopower S and power factor GS^2 and $|GS|S$ 1D histograms of the monomers of EMFs and C_{60}. (a-d) Histograms built with all the data from the I-V curves measured during the complete approach of the tip, from the noise level until close to the metallic contact. (e-h) Histograms built only with first-contact values, i.e., within 0.1 nm after junction formation. Insets in c-d and g-h zoom into the details of the power factor data presented in the main panel. $|GS|S$ 1D histograms (d and h) are shown to highlight the asymmetry due to positive and negative thermopower values.